Automated Analysis and Visualization of Preclinical Whole-body MicroCT Data

Martin Baiker

Colophon

This thesis was typeset by the author using LaTeX 2_ε.

Cover design:
Martin Baiker and Marieke Thurlings

About the front cover:
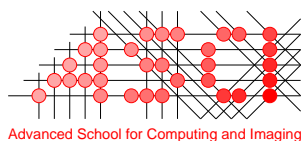Shown is a 'segmented' X-ray picture of a Microsoft mouse (original image by courtesy of www.petergof.com).

About the verso:
Shown are a laughing and a weeping face, the symbols of the ancient Greek muses Thalia (comedy) and Melpomene (tragedy). Image by courtesy of www.theaterverein-thalia.de.

Automated Analysis and Visualization of Preclinical Whole-body MicroCT Data

Geautomatiseerde Analyse en Visualisatie van Preklinische MicroCT Datasets van Hele Lichamen

(met een samenvatting in het Nederlands)

Proefschrift

ter verkrijging van
de graad van Doctor aan de Universiteit Leiden,
op gezag van Rector Magnificus prof. mr. P.F. van der Heijden,
volgens besluit van het College voor Promoties
te verdedigen op donderdag 17 november 2011
klokke 13:45 uur

door

Martin Baiker

geboren te Stuttgart (Duitsland)
in 1978

Promotiecommissie

Promotores:	Prof. dr. ir. B.P.F. Lelieveldt Leiden University Medical Center & Delft University of Technology
	Prof. dr. C.W.G.M. Löwik
Overige leden:	Dr. ir. J. Dijkstra
	Prof. dr. W. Niessen Erasmus Medical Center, Rotterdam
	Prof. dr. ir. M.J.T. Reinders Delft University of Technology

Contents

1

General Introduction

1.1 Molecular imaging for preclinical research

MOLECULAR IMAGING (MI) comprises a new set of technologies for "non-invasive, quantitative and repetitive imaging of targeted macromolecules and biological processes in living organisms [1]." The basis of MI consists of two elements: "(i) molecular probes whose concentration and/or spectral properties are altered by the specific biological process under investigation and (ii) a means by which to monitor these probes [1]." Therefore, imaging modalities for MI can be used for characterization, quantification and visualization of biological processes at the cellular and molecular level in living organisms [2]. In contrast to imaging modalities such as anatomical Magnetic Resonance Imaging (MRI), which rely on non-specific physical or metabolic changes to distinguish pathological from physiological tissue, molecular imaging enables the identification of events like the expression of a particular gene [3]. MI therefore offers great new opportunities because molecular events, that are related to a certain disease, can be detected long before the disease manifests itself by macroscopic anatomical modifications. Because of its non-invasive nature, it also allows to monitor disease progression over time, in a physiologically realistic environment and within the same subject. Compared to classical follow-up studies, in which a part of the cohort had to be sacrificed at each time point, using the same subject over time removes intersubject variation and the studies require significantly less animals [2]. Further applications for MI range from studying gene expression and intracellular events to detection of cell trafficking patterns related to inflammatory diseases and metastases and monitoring therapeutic effects of new drugs by assessing drug distribution and effectiveness [4–6].

For MI, almost all imaging modalities commonly utilized in clinical practice are used ranging from molecular Magnetic Resonance Imaging (MRI), Computed Tomography (CT) and Ultrasound (US) to the nuclear modalities Positron Emission Tomography (PET) and Single Photon Emission Computed Tomography (SPECT) and the optical modality Fluorescence Imaging (FLI). The prerequisite for imaging is that there exists a suitable molecular probe for a particular modality. Since the dimensions of the subjects

in preclinical research are one order of magnitude smaller compared to patients in the clinic, scanning hardware was developed in recent years that is tailored for small animal imaging. The main advantages of preclinical scanners are their compact size, the high resolution, the possibility to scan entire subjects and that some additional modalities are available, for example Bioluminescence Imaging (BLI). Generally, preclinical scanners can be identified by the prefix 'Micro' (see Fig. 1.1).

MI modalities offer a very high sensitivity but generally their spatial resolution is low, which complicates localization of the signal within the animal [7]. Therefore, often datasets of multiple modalities containing complementary information are 'fused'. An example is given in [5], where BLI is used to monitor metastatic activity of breast cancer cells in the mouse skeleton over time. In addition to the BLI signal, a photograph of the animal is acquired that enables to coarsely estimate the location of the metastases. To visually assess the cancer-induced bone resorption, the data is combined with whole-body MicroCT (Fig. 1.2). Besides visual investigation, multimodality fusion may be required to enable quantification of a molecular probe. Examples are the optical modalities BLI and FLI, which require a realistic tissue model of the studied subject based on another modality, in order to accurately determine the location and the emission of a light source within a subject [8, 9]. Another type of application where multimodality imaging is required is computer-assisted scan planning. Approaches are typically based on matching a prior model of the anatomy of interest to a set of scout views. An example is given in [10], where an anatomical mouse atlas was registered to a sparse set of scout photographs, yielding scan Volume-Of-Interest (VOI) estimates for subsequent MicroSPECT data acquisition.

1.2   Image processing challenges

Because of the non-invasive nature of MI, often several data acquisition time points are planned to follow a certain disease or treatment effect over time, within the entire animal. To be able to compare the results, datasets of different time points have to be aligned (registered) to each other. However, this is particularly difficult for whole-body data because of non-standardized acquisition protocols and the fact that the body contains many different tissues with largely varying stiffness properties. This results in a potentially large postural variation between animals that are imaged at different time points (Fig. 1.3, left and middle) or if different animals have to be compared. This postural variation is caused by articulations of the skeletal system, deformations of soft tissues and anatomical difference between animals. While many strategies are discussed in the literature [12–15] for registration of individual objects like the brain or the heart, only few methods aim at registration of objects with greatly varying structural properties and articulations.

Another problem that arises when studying whole-body data is the fact that it may be difficult to image all anatomical structures of interest at the same time with only one modality, because each modality has a specific target. While MRI for example is suitable for imaging soft tissues, it yields no bone contrast whereas in vivo MicroCT data shows excellent bone contrast but only poor soft tissue contrast (Fig. 1.3, right). In exceptional
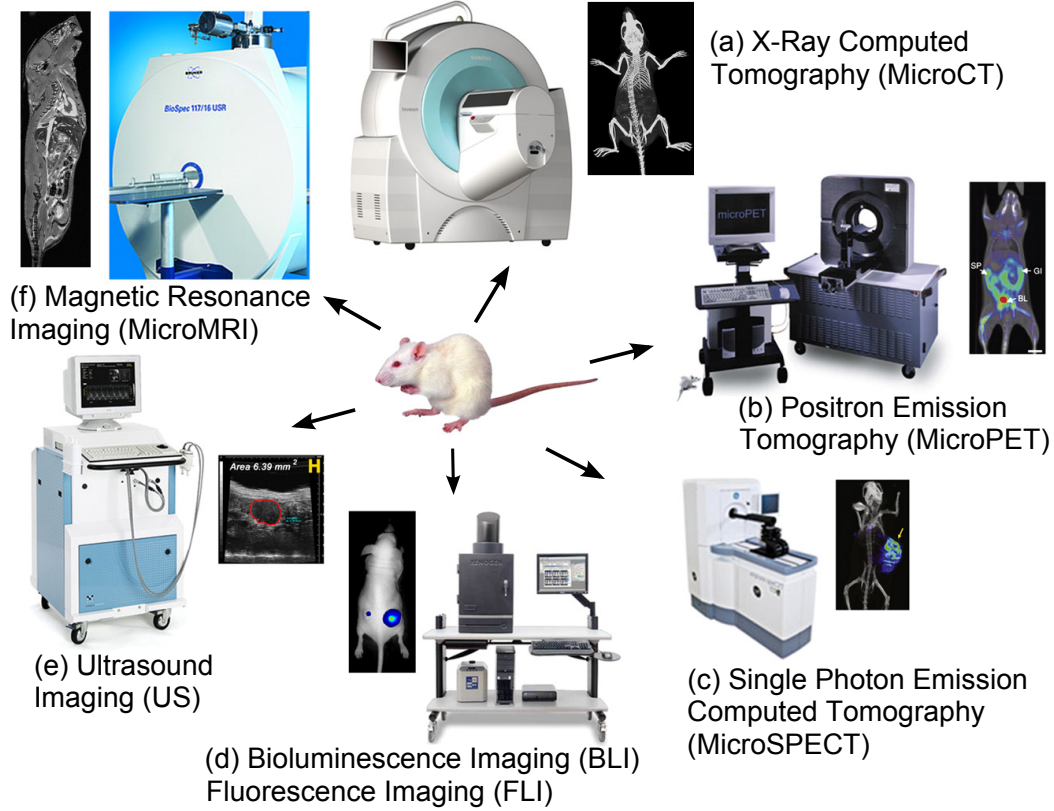
Figure 1.1: Modalities used for preclinical molecular imaging. Figure adapted from [11].

cases, contrast-enhanced MicroCT can be used to obtain soft tissue contrast. However, this solution is usually not preferred because contrast agents are difficult to administer and may influence the outcome of follow-up studies. Thus besides the combination of a functional and an anatomical modality, it sometimes may be necessary to add another anatomical modality.

The necessary combination of modalities for MI leads to another challenge for image processing because datasets from several modalities have to be brought into correspondence. Sometimes researchers can rely on hybrid acquisition hardware integrating several modalities in one setup and thus circumvent this problem. However, these solutions are often not available and not all modalities can be combined.

In conclusion, the challenges for image processing are:

- Potentially large postural variations that complicate comparing animals in follow-up (same animal, multiple timepoints) and cross-sectional (different animals, one timepoint) studies,

- Large tissue heterogeneity of whole-body data with greatly varying stiffness properties and

- Absence of geometrical calibration between scanners in multi modality imaging.
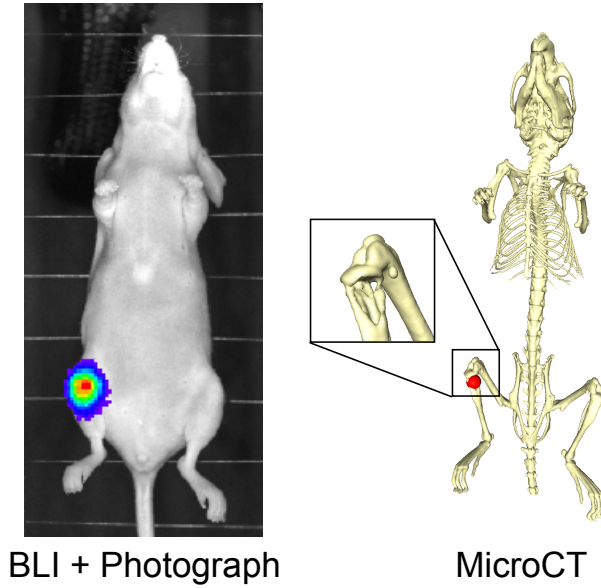
Figure 1.2: *Demonstration of multimodality imaging for BLI and MicroCT. For coarse light source localization, the BLI signal is overlaid on a light photograph (left). For accurate localization or quantification of e.g. osteolysis, a MicroCT dataset should be acquired as well (right). The red sphere represents an approximation of the light source.*

1.3 State of the Art

1.3.1 Registration of whole-body data

For some applications, especially designed holders can be used in order to scan animals in similar position at different time points and thus reduce postural variability [18]. However, such holders may influence the study e.g. by obstructing light in optical imaging based studies and therefore software based solutions for registration of datasets are required as well.

In the literature, several approaches are described to tackle the aforementioned difficulties of whole-body registration. This review mainly focuses on methods for small animal applications. Reported are:

1. *Methods that are based on global image data i.e without including prior knowledge about the internal structure.* Approaches are based on intensity in MicroCT [19] or on extracted features like the mouse skin [20, 21].

2. *Methods that distinguish between different tissue types, based on grayvalues.* One of these approaches is presented in Staring *et al.* [22], where the authors filter the deformation field after each iteration step of the registration, dependent on the tissue rigidity. In [23], the same authors include a rigidity term in the registration criterion. In order to do so, the rigidity has to be determined based on the image data. However, since the method is based on CT data, there is a correlation between tissue rigidity and radio density and rigidity is derived from the Hounsfield units.

Figure 1.3: Postural variation for prone (left) and supine (middle) data acquisition. Figure adapted from [16]. Demonstration of soft tissue contrast in non-contrast-enhanced in vivo MicroCT (right, top) and contrast-enhanced in vivo MicroCT (right, bottom). The labels indicate the heart (red), the lungs (yellow), the liver (grey) and the kidneys (blue). Figure adapted from [17].

3. *Methods that distinguish between different tissue types based on an initial global segmentation.* Xiao *et al.* [24] register two surface representations of a mouse skeleton. Other methods describe a two step approach. First, only the segmented regions are registered, followed by an intensity-based registration step. In Li *et al.* [25, 26] and Suh *et al.* [27], the authors first register the skeleton. In [27], the skin is registered as well, initialized by the result of the skeleton registration. In both approaches, the results of the first step are used to initialize a deformable registration of the entire body. In either case, the modality is MicroCT.

4. *Methods that are based on registration of local image data and subsequent derivation of a global transformation, so-called block-matching methods.* Although these methods in general do not include prior knowledge about the internal structure, the locality of the individual registrations can, to a certain extent, handle varying tissue properties and articulations, depending on the type of transformation. The reviewed methods are all based on intensity and methods differ in the transformation models of the individual blocks. Transformations include translation only [28], translation and rotation [29] and affine [30, 31] local transformations. In all of these approaches, the blocks are registered independently. There is one exception [31], where the blocks are registered simultaneously. A block-matching approach that does include a priori knowledge by means of a hierarchical animal model is presented in Kovacevic *et al.* [18]. In their work, the authors register whole-body MRI data by first registering the entire body, subdividing the result, register again, subdivide again and so on. They identify individual bones and organs in a reference dataset and use affine transformations for registration of individual elements.

5. *Methods that are based on registration of local image data and subsequent derivation of a global transformation, where the local transformations are constrained by including a priori knowledge of the anatomy of the subject.* This can be achieved by including a kinematic model of articulated structures. Martin-Fernandez *et al.* [32] use an articulated hand model and register it to 2D hand radiographs. The individual bones, represented as rods, are initialized by the result of the previous registrations and the transformation is constrained by anatomically realistic motion constraints of the hand joints. Du Bois d'Aische *et al.* [33] register a human head, based on a model of the cervical spine. Articulated vertebrae are registered to the target image and the deformation is propagated to the rest of the head using a linear elastic model. Bones are registered simultaneously, but motion between cervices is small. Van de Giessen *et al.* [34] register the bones of the wrist by imposing motion constraints to prevent unrealistic constellations. All bones are registered simultaneously, but they have to be identified in advance. Papademetris *et al.* [35] use a kinematic model to register the legs of a mouse by modeling the joints. Articulated parts have to be segmented manually.

The presented solutions in Items 1-4 vary greatly in their capability to properly treat tissue heterogeneity and to handle postural variations. The solutions in Item 1 may cause internal tissues to deform in non-realistic ways. However since in [20] and [21] only a representation of the skin is needed, an anatomical organ atlas can be registered to any modality yielding a segmentation of the data. The solutions in Item 2 and Item 3 ensure more realistic deformations for the skeleton [24], the skeleton and the skin [25–27] or various soft tissues [22, 23]. Due to the dependency on a segmentable skeleton and tissue density maps, these methods are mainly restricted to intramodality registration using CT. The methods in Item 4 are capable of handling multimodality data, because registration of the individual blocks is generally intensity-based.

Common to all methods discussed so far is that they may suffer from local minima during registration because of limited capability to handle large postural variations, or if bones lie in close proximity like e.g. around the ribcage. In these situations, obtaining the correct result cannot be guaranteed.

Most approaches in Item 5 are inherently more robust to deformations caused by articulations, because these articulations are explicitly modeled and taken into account during registration. To date, all these methods derive local transformations of target structures and if desired, determine a global transformation using a weighted combination of the local transformations [18, 32], a linear elastic model [33] or a solution to ensure global invertibility [35].

None of the approaches discussed so far did address the problem of dealing with structures that do not show sufficient contrast for registration, [20] and [21] being the only exceptions. In their work they demonstrate how registration using an anatomical animal atlas (the Digimouse [36]) can compensate for missing structural information.

1.3.2   Registration of datasets from different modalities

Molecular imaging applications typically rely on multimodality image acquisition to combine functional and structural data and thus to facilitate visual localization and quantification of molecular events (Sec. 1.1). Many solutions for multimodality image fusion are described in the clinically oriented literature. The most relevant application areas are oncology, cardiology, neurology as well as radiation therapy planning or assessment of therapy and typical modality combinations are MRI or CT and PET or SPECT [13,15,37].

With preclinical (animal) imaging, the variety of imaging procedures is even larger than in clinical imaging, since almost every research question to be answered requires a unique protocol. Consequently, many multimodality studies based on small animals require a specific solution to register two or more modalities. Currently, preclinical counterparts of clinical hybrid systems became available that allow to acquire PET and CT [38], SPECT and CT [39], PET and MRI [40] as well as SPECT and MRI [41] (refer to [42] and [43] for reviews). After data acquisition, the datasets can be 'fused' directly because all of the modalities yield 3D data, registered by hardware. The same is true for 2D hybrid systems like the combination of radiography and optical imaging in one device [44].

Other possible modalities that are used in combination differ in data dimensionality and are typically combinations of 3D data and 2D data. Douraghy *et al.* [45] present an integrated Optical-PET (OPET) scanner that is currently under development and FLI-PET [46] and CT-Optical [47] systems are also presented. A very interesting novel approach is presented in Hillman *et al.* [48] where the authors only rely on an all-optical system to derive the location and shape of all major organs. To this end they measure the biodistribution dynamics of a fluorescent dye and subsequently derive organ boundaries. At the same time, MI information is acquired.

Imaging experiments using several single modality acquisition hardware require software solutions to register the data after acquisition. Most methods are based on using the same animal holder in all modalities and animals are usually anaesthesized during scans to minimize body movement induced artifacts. Therefore most studies include a rigid transformation model. Again, handling datasets with equal dimensionality are most straightforward. Combinations of volumetric data are PET-CT [49], PET-MRI [50, 51], SPECT-CT [52] and CT-PET-SPECT [53]. Image similarity measures are generally based on intensity or intensity gradients but can also be feature-based. A projection of structured light can be used to reconstruct the skin surface of an animal in 3D and subsequently registered to CT [54] and MRI data [55].

It gets more complicated if data of different dimensionalities need to be fused, because derivation of a similarity measure is not straightforward any more and the transformation model usually has to incorporate scaling parameters as well. Although it is possible to circumvent these issues and make use of external [8,10] or implanted fiducial markers [56], these solutions require significant user effort to place the markers and generally have limited accuracy. Within the image processing literature regarding small animal data, very little work has been published on fully automated registration of data with different dimensionality. Exceptions are two methods for registration of 2D projections of a mouse skin, derived from 3D MicroCT data, and one [57] or three [58] 2D photographs of the same animal including an affine and rigid transformation model respectively.

1.4 Goals of the research

Based on the particular challenges that arise for imaging entire bodies (sec. 1.2), the overall goal of this thesis is to develop methods for the analysis and visualization of cross-sectional and longitudinal (follow-up) whole-body small animal imaging data.

In particular, we focus on developing methods that:

- Are highly robust to large postural variation

- Can deal with the large heterogeneity of animal bodies

- Can compensate for lacking tissue contrast and

- Can facilitate the combination of multiple modalities.

1.5 Outline of the thesis

This manuscript is organized as a collection of scientific papers: consequently, a certain degree of content overlap will be present in the most general parts of the following chapters. The context and novelty of each chapter are described here.

In Chapter 2, the process of developing an articulated animal atlas is described. Based on labeled 3D volume datasets of three publicly available whole-body animal atlases (MOBY mouse [59], Digimouse [36], SD Rat [60,61]), the skeletons are segmented manually into individual bones in a first step. Second, joint locations are defined and anatomically realistic motion constraints are added to each joint. Finally, surface representations of the individual bones and major organs (skin, brain, heart, lungs, liver, spleen, kidneys, stomach) are combined, yielding a representation of the atlas that forms the basis of the methods presented in the following chapters. In addition, some application examples for usage of such an atlas are given. The atlases are made publicly available (http://www.lkeb.nl).

In Chapter 3, a novel and highly robust method for segmentation of in vivo whole-body MicroCT data is presented. It is based on a combination of the articulated MOBY atlas developed in Chapter 2 and a hierarchical anatomical model of the mouse skeleton, and enables to achieve a fully automated registration of the atlas to a skeleton surface representation from the target data. First, the entire skeleton is coarsely aligned and subsequently, individual bones are registered one by one, starting with the most proximal bones and ending with the most distal bones. This renders the method highly robust to postural variations and greatly varying limb positions. Other high contrast organs, namely the lungs and the skin, are registered subsequently, initialized by the skeleton registration result. In a final step, low-contrast organs are mapped from the atlas to the target by means of Thin-Plate-Spline interpolation. The main novelty of the method is the high robustness with respect to postural variations and the usage of a whole-body atlas, to compensate for missing organ contrast. Another novelty is the robustness with respect to severe bone malformation because of e.g. metastatic activity. The Degrees of

General Introduction

Freedom of the individual bones are constrained such that even large holes in the skeleton do not cause the registration of the individual bones to fail.

Possible applications of the automated whole-body segmentation include anatomical referencing and it allows to provide a heterogeneous tissue model of the target that can be used to improve the light source reconstruction in optical tomography approaches. Another application example is the qualitative analysis of differences between individual bones or organs in intramodality follow-up or cross-sectional datasets. Chapter 4 describes, how the result of the atlas-based skeleton registration can be used for mapping multiple time points of a follow-up MicroCT datasets into a common reference frame (Articulated Planar Reformation, APR) and be visualized side-by-side. Above that, several change visualization strategies are discussed that can help researchers to easily follow e.g. a certain therapeutic effect over time without any user interaction. The novel aspects in this chapter are the framework for automated navigation through whole-body data and the side-by-side assessment of whole-body follow-up data.

In Chapter 5, the APR framework is extended by a concrete example, where accurate quantification is required to follow disease progression over time. More specifically, tibial tumors are induced by breast cancer cells and osteolysis is followed over time in whole-body MicroCT datasets. To this end, a structure of interest, in this case the tibia, is selected automatically in each time point and combined with a highly accurate segmentation strategy and subsequent measurement of bone volume changes over time. Besides that, a way to determine and visualize cortical bone thickness is demonstrated. Thorough statistical analysis reveals that the segmentation results of the automated method and two human observers do not differ significantly. The novelties presented in this chapter are the analysis of osteolysis in 3D data, the automated segmentation of a particular structure of interest in whole-body in vivo data and the automated derivation and visualization of cortical bone thickness maps.

The atlas-based skeleton registration presented in Chapter 3 proved to be highly robust to postural variation and pathological bone malformations. However, this is at the expense of bone registration accuracy. In Chapter 6, the robustness of the articulated registration is combined with the accuracy of an intensity-based registration algorithm. An intensity-based similarity criterion is regularized with the corresponding point information obtained from the articulated registration. Registration is formulated as an optimization problem and solved using a parameter-free and very fast optimization routine in a multiresolution fashion using Gaussian pyramids. It is shown that the combination of intensity and the corresponding point information outperforms methods based on either intensity or corresponding point information alone and that the method is highly time efficient, compared to other published work.

Another important aspect of preclinical MI applications is addressed in Chapter 7. The goal of the presented work is to automatically register multimodality, multidimensional data, namely 3D MicroCT of an animal and two or more 2D photographs of the same animal, taken at different viewing angles. 2D photographs are often taken together with Fluorescence and Bioluminescence data and with the automated registration, the FL and BL data can be related to 3D anatomical MicroCT data without the requirement of two calibrated systems or the knowledge of the between-system transformation matrix.

Chapter 1

The only requirement is that the animal is placed on a multimodality holder and does not move during the transport from one scanner to the other. The fact that the registration is performed in 3D, based on an approximate reconstruction of the skin surface from the 2D projections, renders the method fast and flexible; the more 2D projections are available, the better the 3D reconstruction and therefore the registration accuracy but without noticeable increase in time requirement for the 3D reconstruction. Chapter 8 summarizes the findings of this thesis and presents some areas of future work.

General Introduction

2

Articulated Whole-Body Atlases for Small Animal Image Analysis: Construction and Applications

Chapter 2

Abstract

Purpose: Using three publicly available small-animal atlases (SpragueDawley rat, MOBY, and Digimouse), we built three articulated atlases and present several applications in the scope of molecular imaging.

Procedures: Major bones/bone groups were manually segmented for each atlas skeleton. Then, a kinematic model for each atlas was built: each joint position was identified and the corresponding degrees of freedom were specified.

Results: The articulated atlases enable automated registration into a common coordinate frame of multimodal small-animal imaging data. This eliminates the postural variability (e.g. of the head or the limbs) that occurs in different time steps and due to modality differences and non-standardized acquisition protocols.

Conclusions: The articulated atlas proves to be a useful tool for multimodality image combination, follow-up studies, and image processing in the scope of molecular imaging. The proposed models were made publicly available.

2.1 Introduction

IN PRECLINICAL RESEARCH, different imaging modalities are used for the in vivo visualization of functional and anatomical information. Structural imaging modalities such as magnetic resonance imaging (MRI), computed tomography (CT), and ultrasound provide detailed depictions of anatomy. Positron emission tomography (PET), single photon emission computed tomography (SPECT) and specialized MRI protocols add functional information. In addition, optical imaging modalities, such as bioluminescence imaging (BLI) and near-infrared fluorescence imaging offer a high sensitivity in visualizing molecular processes in vivo. In combination, these modalities enable the visualization of the cellular function and the follow-up of molecular processes in living organisms without perturbing them.
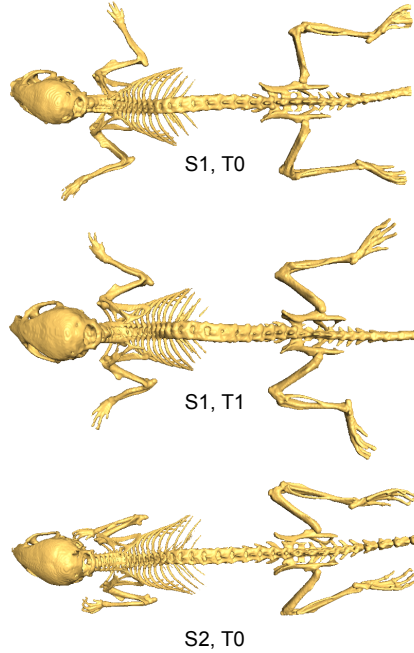
Figure 2.1: Illustration of the postural variability (limbs, head) that occurs in follow-up and cross-sectional molecular imaging studies. Shown are two mice (S1 and S2) at two different time points (T0 and T1).

Due to the high number of existing imaging modalities, a new, different challenge emerged: how to best combine and analyze all these data. The problem is shifting from data acquisition to data organization, processing and analysis, and the main difficulty of this task is the enormous data heterogeneity and volume/throughput. The above-mentioned imaging techniques provide 2D, 3D, or 4D images depending on modality and are used in follow-up and cross-sectional studies using different animals (according to strain, size, age, body fat percentage, population). One other very important factor is the postural variability: there is no standardized protocol for imaging. If a subject is imaged using different imaging modalities and protocols during follow-up studies or

if different animals are used, the subject is positioned in different ways and postural variations occur (e.g. of the head or the front limbs, refer to Fig. 2.1, Fig. 3.8 and Fig. 2.3). Although there are some multimodality animal holders, to date, they are not widely used, and even with the use of the holders, there are still significant differences in animal posture between different time points. All these factors contribute to the large data heterogeneity.

One way of handling this problem is to use atlases. In biomedical imaging research, anatomical atlases have proven to be useful for defining a standard geometric reference for further subject analysis and meaningful comparisons. Atlases may consist of a 3D, sometimes 4D, whole-body or organ-based geometric representations. This enables mapping functional activity and anatomical variability among individuals and populations. Considering the issues mentioned above, having such a model allows for a more effective way to combine, structure, and execute all sorts of comparisons and correlations within the data. For example, it is possible to make population brain studies in a specific time frame. For that, brain images from each individual, obtained through MRI, PET and other imaging techniques, are spatially warped to a brain template. After combining the data, inferences are made about tissue identity at a specific location by referring to the atlas or looking for variability of those locations within that population.

There is a large number of clinical atlases that are available and widely used in population imaging, image segmentation, image registration and in shape differences and follow-up studies. Three of the most well-known and used atlases within the clinical research scope are the Talairach brain atlas [62], the Visible Human Project whole-body atlas [63], and the 4D NCAT torso phantom [64]. The Talairach atlas consists of a standard 3D coordinate space with labeled regions and structural probability maps and is available for clinical use. This atlas is not only used for stereotactic and functional neurosurgery but also in human brain mapping, neuroradiology, medical image analysis, and neuroscience education. The Visible Human Project consists of manually annotated MRI, CT and cryosection images for both male and female human bodies. The available datasets were designed to serve as a reference for the study of human anatomy and have been applied to a wide range of educational, diagnostic, treatment planning, virtual reality and artistic, mathematical, and industrial uses [63]. The 4D NCAT phantom on the other hand provides a more realistic model of the human anatomy and motions because it does not sacrifice any flexibility to model the anatomical variations and patient motion and has been used in SPECT simulations [64]. For a more detailed survey on computational anatomical and physiological models, see [65].

Within the scope of preclinical molecular imaging research, there are various mouse and rat atlases with different characteristics and purposes, acquired using different techniques (CT, MRI, cryosectioning, etc.). Many of those are thoroughly described and published in literature and are publicly available: the LONI Rat atlas published by the UCLA Laboratory of Neuro Imaging [66] and other brain focused atlases [67–71], the Edinburgh Mouse Atlas Project [72] that describes and presents a 3D model of the mouse embryo, the MRI Atlas of Mouse Development from the California Institute of Technology [73], the Mouse Cochlea Database made by the University of Minnesota [74], and whole-body small animal atlases like the MOBY mouse [59], the Digimouse [36] and the

high resolution SpragueDawley (SD) rat [60, 61].

However, these mouse and rat atlases are either specific, organ-dedicated atlases (brain, hypothalamus, heart, etc.), low-resolution or cannot be deformed in a realistic manner to compensate for the large postural variations that may occur within the scans. Postural variability occurs when using different imaging modalities, during follow-up studies (different time steps) or if different animals are used, because mice are positioned in different ways when scanned. Above that, there is no standardized acquisition protocol.

The work described here addresses the abovementioned problems by introducing articulations in three existing whole-body atlases: The Digimouse [36], the MOBY mouse [59] and the SD rat [60, 61]. A kinematic model is built for each atlas, where bones in each skeleton are manually segmented and labeled. In addition, the corresponding degrees of freedom (DoFs) for each joint are defined.

Mapping to this articulated atlas has the advantage that all the different imaging modalities can be (semi) automatically registered to a common anatomical reference; postural variations can be corrected and the different animals (according to strain, size, age, body fat percentage) can be scaled properly.

The goals of this work are to:

1. Introduce the concept of the articulated whole-body small animal atlas,

2. Present and discuss several implemented application examples: atlas to MicroCT data registration, follow-up MicroCT studies, cross-sectional MicroCT studies, multimodality atlas to BLI and MicroCT image registration and analysis and atlas to MicroMRI data approximation and

3. Make these three articulated whole-body small animal atlases publicly available.

2.2 Methods

2.2.1 Atlas Descriptions

Presently, in the work described here, three small animal atlases are used. In this section, a brief description of each one is presented.

MOBY (Mouse Whole-Body) Atlas

Segars *et al.* generated a realistic 4D digital mouse phantom based on high-resolution 3D MRI data from Duke University. The organs of this atlas were built using non-uniform rational b-spline (NURBS) surfaces, which are widely used in 3D computer graphics. The final package includes a realistic 3D model of the mouse anatomy and accurate 4D models for the cardiac and respiratory motions. Both the cardiac and respiratory motion models were developed based on cardiac gated black-blood MRI and respiratory-gated MRI data from the University of Virginia. It has been used in simulation studies in SPECT and X-ray CT [59].

Chapter 2

Digimouse Atlas

Dogdas *et al.* constructed a 3D whole-body multimodal mouse atlas from coregistered X-ray MicroCT and color cryosection data (anatomical information) of a normal nude male mouse. It also includes PET data (functional information) representing the distribution of a mixture of the tracers [18^F] fluoride and 2-deoxy-2-[18^F]fluoro-D-glucose within the mouse. The image data were coregistered to a common coordinate system using fiducial markers and resampled to an isotropic 0.1mm voxel size. Using interactive editing tools, several organs were segmented and labeled. The final atlas consists of the 3D volume (in which the voxels are labeled to define the anatomical structures listed above) with coregistered PET, X-ray CT, and cryosection images and can be used in 3D BLI simulations and PET image reconstruction [36].

High-Resolution SD Rat Atlas

Xueling *et al.* built a high-resolution 3D anatomical atlas of a healthy adult SD rat from 9475 horizontal cryosection images (at $20\mu m$ thickness). Coronal and sagittal section images were digitized from the horizontal sections and anatomical structures under the guidance of an experienced anatomist. The 3D computerized model of the rat anatomy was generated using a parallel reconstruction algorithm and interactive atlas-viewing software was developed that offers orthoslice visualization, featuring zoom, anatomical labeling, and organ measurements. Also, an interactive 3D organ browser based on a virtual reality modeling language was made available on a website. The models of each organ and tissue constructed from the images were used for calculations of absorbed dose from external photon sources [60, 61].

Fig. 2.8 in the Appendix provides a visual comparison between the original atlases described above. While the MOBY and Digimouse atlases are quite similar in content, they differ in terms of the species of the mouse, the types of organs defined, resolution and in the modalities from which they were constructed. Also, the MOBY atlas includes a model of cardiac and respiratory motion. In Tab. 2.4 in the Appendix, an overview of the main differences between these three atlases is presented.

2.2.2   Articulated Atlas Construction
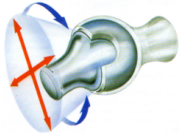
In all the abovementioned atlases, the included skeletons do not distinguish between single bones and joints. To render the registration performance independent of the data acquisition protocol and large postural variations due to postural heterogeneity between scans, we present a segmentation of the skeleton into individual bones and add anatomically realistic kinematic constraints to each joint.

Segmenting the Skeleton

The first step was to manually segment the following bones/bone groups in each atlas from the skeleton using the Amira V3.1 software [75], guided by anatomical text books [76, 77] and a high resolution CT scan of a real mouse: scapula, humerus (upper front limb),

Table 2.1: *Joint types of the animal skeleton and the DoFs for the registration of the distal articulated bone (Pictograms from [78]).*

Joint types	Modeled joint	DoFs of the distal bone
Ball joint	Shoulder Wrist Hip Ankle	0 Translations 3 Rotations 3 Scalings
Hinge joint	Elbow Knee	0 Translations 1 Rotation 3 Scalings

clavicula (collarbone, rat only), ulna-radius (lower front limb), manus (front paw), femur (upper hind limb), tibia-fibula (lower hind limb), pes (hind paw), caput (skull), columna vertebralis (spine), costae (ribs), sternum (chest bone) and pelvis. The resulting labeled skeletons for each atlas can be seen in Fig. 2.2.

Introducing Joint Kinematics

In the second step, a kinematic model for each atlas was built, i.e. each joint position was identified and the corresponding DoFs were specified. Two types of joints were distinguished: ball joints and hinge joints. In Tab. 2.1, the DoFs for the ball and hinge joints can be seen. These DoFs are anatomically correct and were defined according to expert specifications described in literature [76, 77].

2.2.3 Atlas-Based Whole-Body Registration/Segmentation of Small Animal Datasets

The skeleton is the rigid frame of the animal, in the sense of tissue stiffness. Besides the articulations of individual bones with respect to each other, little deformation takes places in the bones themselves within the same animal. This is in contrast to e.g. organs, which highly vary in shape, depending on the posture of the animal. Therefore, a robust registration strategy should be based on the skeleton. Although there are approaches in literature that perform small animal whole-body image registration based on the entire skeleton [19, 26], these methods may fail if large postural variations occur among different animals or among the same animal in a follow-up study.

Therefore, we propose an approach that employs the articulated skeleton model as

MOBY   Digimouse   SD Rat
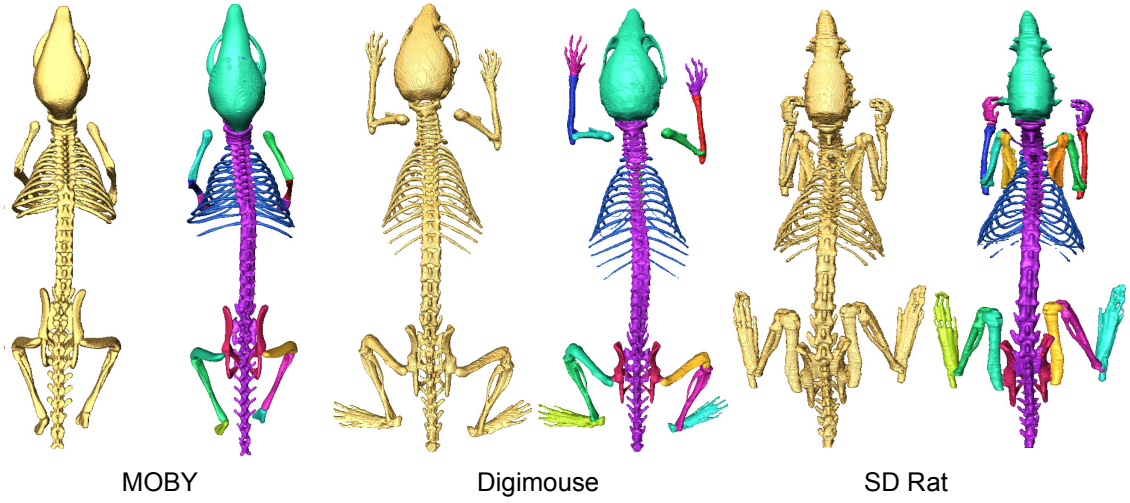
Figure 2.2: Illustration of the atlas skeletons before (left) and after (right) manual segmentation.

described above for registration of the skeleton in a first step. Organs are nonrigidly matched in a second step, initialized by the result of the skeleton matching.

Skeleton Registration

The more distal a given bone is in the skeleton, the more variable its position between acquisitions is. Therefore, if datasets of several mice are globally aligned to each other, the location of the skulls is more similar than for instance that of the paws. Given that the entire atlas skeleton is coarsely aligned to a target dataset in a first step, all bones can subsequently be matched individually by executing the registration from proximal to distal bone segments. The registration of a distal segment is thereby constrained by the joint type of the proximal bone it connects to. For example, for the tibia, the registration is constrained by the DoFs of the knee joint. The deformation model that is required for the individual bones depends on the type of study and may vary between rigid (intrasubject) and nonrigid (intersubject) deformation models. The selected registration criterion depends on the modality of interest. It can be a point-based (e.g. Euclidean distance), surface-based (e.g. Euclidean distance and surface curvature), or volume-based registration criterion (e.g. Normalized Mutual Information). In this paper, we limited ourselves to a surface-based registration measure, i.e. the Euclidean distance between two surfaces. Since the registration has to deal with large articulations, potentially pathological data (as a result of bone resorption) and intersubject data, a rigid transformation model including non-isotropic scaling was chosen. This renders the registration robust to pathological cases while still taking different bone sizes into account. The registration was embedded in the Iterative Closest Point [79] framework and optimized using an interior-reflective Newton method.

Organ Registration

The registered skeleton allows us to initialize the registration of several major organs, because their location is strongly related to the posture of the skeleton. To realize this, the transformation model should be chosen such that it can handle the large deformations that can occur for soft tissues. Many methods have been proposed for registration of individual organs (see e.g. [12,14] for reviews), which are not discussed further here. In the applications described next, we selected Thin-Plate-Spline (TPS) interpolation [80]. The required anatomical landmarks that define the TPS mapping are primarily derived from the registered skeleton. To this end, we compute a sparse set of initial correspondences on the animal skin by selecting the skin points, closest to a set of anatomical landmarks on the skeleton (e.g. the joints). From this sparse set of skin points, a denser set of point correspondences is calculated by means of an iterative matching of local distributions of geodesic distances [17]. This results in a set of correspondences on the skin and on the skeleton, which in combination define the TPS interpolants.

2.2.4 Evaluation Metrics for Registration Accuracy

To evaluate the accuracy of the registration algorithm for the skeleton, skin and organs, three different error metrics were defined [17]: Joint localization error is calculated as the Euclidean distance between corresponding anatomical landmarks (point-to-point distance). To this end, the locations of the upper lower limb and the lower limb-paw joints of all datasets were indicated manually using the extracted skeleton surfaces. For validation, the manually determined joint locations were compared to those automatically determined by registration of the skeleton. Euclidean point-to-surface distance was determined to quantify border positioning errors. It was used to evaluate the registration error over the surface of the entire skeleton and skin. Dice coefficients of volume overlap s [81] were computed to assess the organ interpolation performance. The Dice coefficient is widely used in literature to assess segmentation accuracy by evaluation of the spatial overlap of a manual and an automated segmentation. It is a voxel-based measure and therefore includes differences in object sizes as well as spatial misalignment [82]. Given the absolute volumes of a manual segmentation result V_m and an automated segmentation result V_a, the Dice coefficient is defined as the intersection of the volumes, divided by the average volume:

$$s = 2\frac{|V_m \cap V_a|}{|V_m| + |V_a|} \tag{2.1}$$

2.3 Applications

In this section, two application examples are presented that employ the articulated skeleton model for analysis of follow-up, cross-sectional and multimodality small animal imaging studies. Each application was quantitatively validated.

Table 2.2: Skeleton, lungs and skin registration results before the registration, i.e. after initialization (left), and after registration (right).

	Before registration	After registration
	Joint localization error [mm]	
Right knee	14.29 ± 5.51	0.75 ± 0.29
Right ankle	18.70 ± 5.87	1.82 ± 1.01
Left knee	16.61 ± 4.80	0.77 ± 0.26
Left ankle	19.93 ± 5.15	1.69 ± 1.14
Right elbow	5.66 ± 2.11	1.31 ± 0.44
Right wrist	15.56 ± 4.49	1.27 ± 0.53
Left elbow	5.23 ± 2.96	1.23 ± 0.39
Left wrist	18.04 ± 6.47	1.21 ± 0.56
	Euclidean point to surface distance [mm]	
Entire skeleton	3.68 ± 0.77	0.58 ± 0.03
Lungs	1.27 ± 0.26	0.47 ± 0.03
Skin	11.06 ± 8.49	0.75 ± 0.53

2.3.1 Atlas to MicroCT Registration for Follow-Up and Cross-Sectional MicroCT Studies

Whole-Body Segmentation Based on Articulated Skeleton Registration

Anatomical referencing of molecular events inside the animal using non-contrast-enhanced MicroCT is difficult, because although the skeleton can be extracted easily from the data as a whole it is often required to know exactly in which bone the molecular event takes places and because the poor soft-tissue contrast in the abdomen complicates organ localization and renders registration very difficult. Above that, MicroCT is often used in oncological studies to assess metastatic activity in bone and since the locations where possible metastases can develop greatly varies, a very flexible data acquisition protocol, with respect to animal positioning in the scanner, is required. For such applications, animal posture, shape, and limb position may vary substantially.

To deal with the challenges specific to MicroCT, we employ the fully automated articulated atlas-based skeleton and organ segmentation method for non-contrast-enhanced whole-body data of mice [17] described in the section above. The skeleton is represented with a surface, derived from the modified MOBY atlas.

To test the proposed method, data acquired during a study of the metastatic behavior of breast cancer cells were used. Breast cancer has a preference to metastasize to bone and at the location of a metastatic lesion, osteolysis occurs, causing structural damage in the skeleton (fractures or completely resorbed bones). The subject was injected with luciferase positive human MDA-MB-231 breast cancer cells into the cardiac left ventricle.
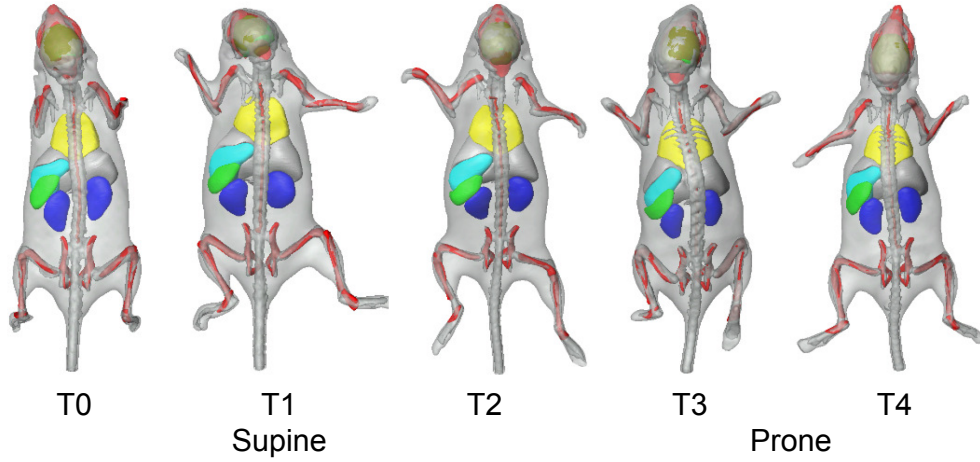
Figure 2.3: Skeleton registration and organ approximation using the same subject, at five differ-ent time points (T0-T4). The animal was put into the acquisition device arbitrarily, in supine (T0-T2) and prone (T3, T4) position, respectively. The resulting postural variations of the head, the spine and the front limbs are clearly visible.

The animal was scanned 40 days after cell injection to screen for possible small amounts of photo-emitting tumor cells in bone marrow/bone mimicking MicroCT-metastatic spread. Nine anesthetized mice (Balb/c, Charles River WIGA, Sulzfeld, Germany), 69 week old, eight female, one male, with a mean weight of 22.23 ± 2.18g, were acquired with a Skyscan (Kontich, Belgium) 1178 MicroCT scanner. Fourteen 3D data volumes of the nine mice were acquired with step size $1°$, 50 keV X-ray voltage, an anode current of 200 μA, an aluminum filter of 0.5 mm thickness, an exposure time of 640 ms and without using a contrast agent. The reconstructed datasets covered the range between -1000 (air) and +1000 (bone) Hounsfield units. Neither cardiac nor respiratory gating was used. The mice were scanned in arbitrary prone and supine postures and arbitrary limb positions.

Tab. 2.2 shows the joint localization and point to surface errors for before and after registering the articulated atlas skeleton, lungs and skin to the data. Subsequently, the brain, heart, liver, kidneys, spleen and stomach were mapped from the atlas to the subject using TPS interpolation [17]. The result is a segmentation of the animal body into individual bones and major organs. This can be used for qualitative assessment of morphology at a single point in time in one or more animals (cross-sectional study) (Fig. 3.8), or to follow morphological changes over time (follow-up study) (Fig. 2.3). To facilitate the comparison of cross-sectional and follow-up data, also visualization concepts were developed that are based on mapping the data to a common reference frame and present the results simultaneously (Fig. 2.4).

2.3.2 Multimodality Registration, Visualization and Analysis Combination of BLI and Segmented MicroCT Data

BLI is an imaging technique that has found widespread application in preclinical research over the past years. It is used to track cells and monitor the function of specific genes and
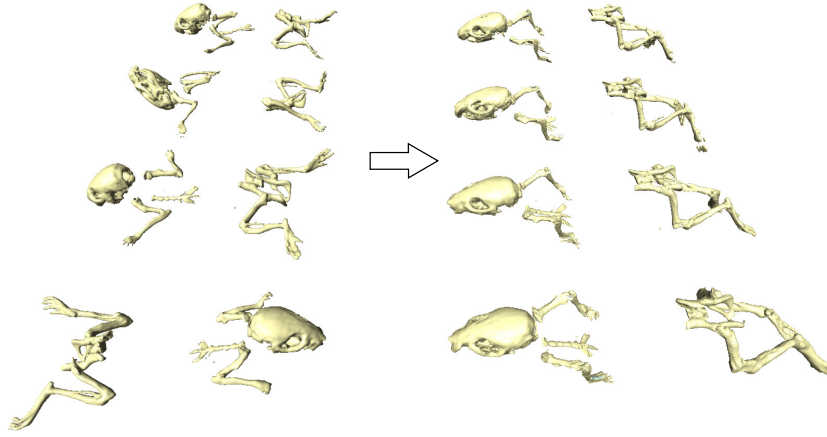
Figure 2.4: Demonstration of mapping the registered bones of four different animals from the corresponding target domain to a common reference domain (the MOBY atlas domain). The large postural differences of the animals (left) are not present any more (right), enabling a more intuitive comparison of different time points.

processes in the cellular biochemistry with a high sensitivity in living animals. A typical application domain is oncology, where researchers aim at monitoring the development of metastases using a highly sensitive optical modality (BLI) and relate it to morphological changes using an anatomical modality like MicroCT [5,6].

Since BLI does not show anatomical information, it is often overlaid on multiple 2D photographs from different angles around the animal. This however has the disadvantage that anatomical referencing is limited to the animal skin and therefore, allows only coarse source localization. Thus, a combination with a real 3D anatomical modality like MicroCT is preferable. This requires a BLI to CT registration approach. The BLI data in this work was acquired using the Xenogen IVIS Imaging System 3D series scanner by Caliper LifeSciences (Alameda, USA). The data was collected from a study with two experiments in mice on the metastatic behavior of breast cancer cells, to visually correlate the reconstructed BLI sources with MicroCT data. One hundred thousand RC21-luc cell, luciferase expressing human renal carcinoma cells, and 100 μl 100000 KS483-HisLuc cells, luciferase expressing murine mesenchymal stem cells, were injected under the renal capsule and into the left heart ventricle respectively, and scanned after 3 to 4 weeks (time for the carcinoma to develop).

Two alternative ways have been worked out to perform the BLI to CT registration. A semiautomated method, which requires manual selection of at least three anatomical landmarks both on the photographs and the CT data, was implemented. Subsequently, these corresponding landmarks are used to map one data domain to the other. As a second approach, a fully automated way to perform this registration was implemented. Based on the skin contours on the photographs, a 3D distance map is derived and used for registration of the animal skin, derived from CT [83]. In addition, the atlas to CT mapping as described above can be applied as well. The result is a fully segmented animal that serves for anatomical referencing, if combined with a qualitative BLI source localization algorithm (e.g. [7]) as shown in Fig. 2.5. The quantitative results for the
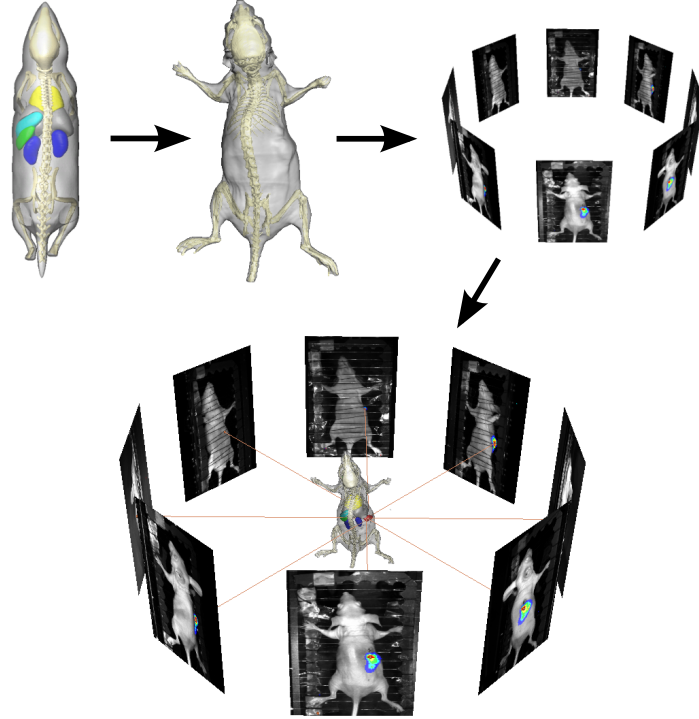
Figure 2.5: Overview of the steps towards a combined visualization of fully segmented whole-body MicroCT and BLI data. The MOBY atlas is registered to the MicroCT data and subsequently, the MicroCT data is registered to the BLI data using the photographs, either by using manually selected landmarks or fully automatically using a 3D distance map (see text). In the resulting visualization, the BLI source (red) is shown and can be related to the skeleton and organs.

articulated skeleton atlas to MicroCT registration are the following: entire skeleton before registration 4.25 ± 12.25mm, after registration 0.63 ± 1.04mm, lungs before registration 1.27 ± 2.44mm and after registration 0.50 ± 1.35mm.

2.3.3 Atlas to MicroMRI Approximation

Organ and Bone Approximation for Ex Vivo Mouse Data

Since MicroMRI data provide greater contrast between the different soft tissues of the body but poorer bone contrast than CT data, it can be used to closely follow the changes in phenotype in studies that require genetic modifications.

A novel semiautomated organ approximation method for MicroMRI mouse data that considerably reduces the required user effort compared to manual segmentation was implemented. It includes the limbs and provides a shape approximation of the bones in MR data. To derive the set of skin correspondences, the user interactively points out the joints/bone landmarks guided by anatomically realistic kinematic constraints, imposed by the articulated atlas. Given this set of dense skin correspondences, the organ approximation is performed using the TPS approximation as described in the Sec. 2.2. The bone approximation is performed by (1) automatically identifying all the joints out of the
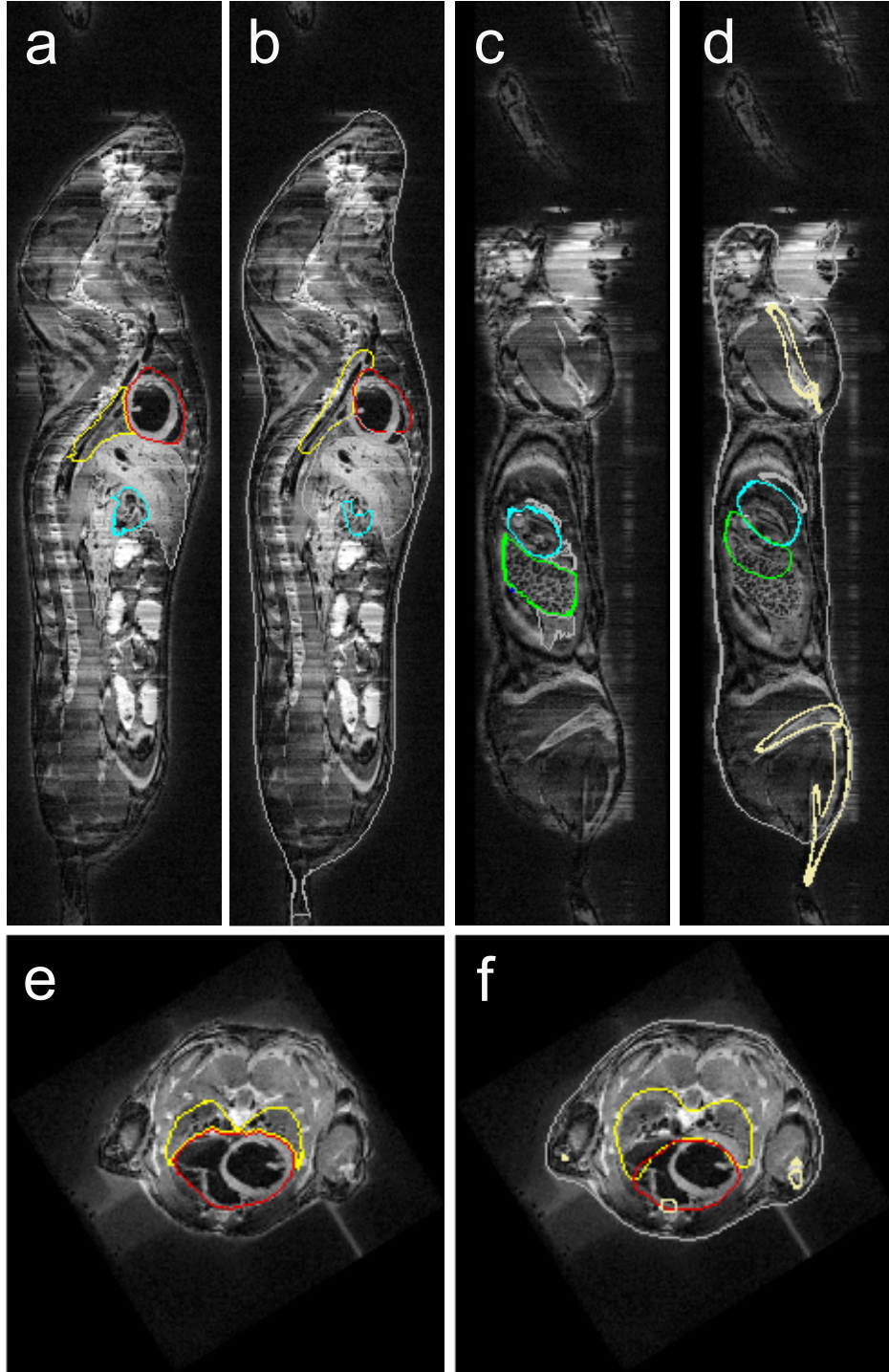
Figure 2.6: Organ and bone approximation results for MicroMRI mouse data. Manual organ segmentation (a, c, e) and bone and organ approximation (b, d, f) results for two sagittal (top) planes and one transverse (bottom) plane, respectively. Yellow: lungs, red: heart, green: spleen, cyan: stomach, cream: bone, gray: skin and liver. Reproduced from [84] with permission.
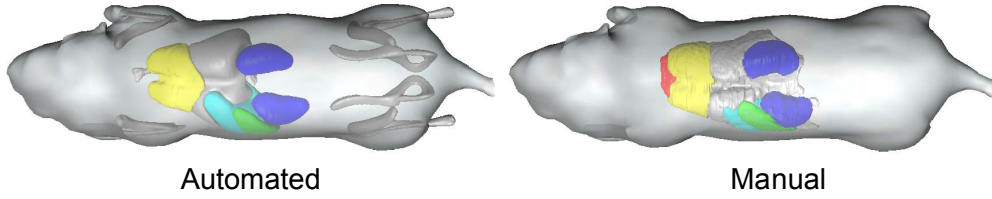
Figure 2.7: *Automated bone and organ approximation and manual organ segmentation.*

Table 2.3: *Organ approximation results for three MicroMRI datasets and four organs: heart, lungs, kidneys and liver. Presented are organ volumes derived manually (V_m) and automatically (V_a) as well as the Dice Coefficient. The last three columns show a comparison with results obtained by Chaudari et al. [20], Baiker et al. [86], and Joshi et al. [87].*

	Mouse 1			Mouse 2			Mouse 3			[20]	[86]	[87]
	$V_m[mm^3]$	$V_a[mm^3]$	Dice	V_m	V_a	Dice	V_m	V_a	Dice	Dice	Dice	Dice
Heart	292.62	227.16	0.65	282.36	241.83	0.80	292.56	202.19	0.74	0.47	0.81	0.82
Lungs	421.15	392.78	0.39	429.74	437.26	0.56	344.55	362.38	0.44	0.49	0.82	N/A
Kidneys	264.57	268.10	0.43	301.28	268.94	0.72	305.68	231.27	0.72	0.44	0.60	0.59
Liver	1131.77	1776.11	0.63	1087.54	1939.77	0.68	1484.82	1551.95	0.63	0.65	0.80	N/A

manually indicated landmarks and (2) applying a scaling and rotation to the atlas bone surfaces [84]. This MRI segmentation method was tested on female C3H mice, perfusion fixed with formalin and 10 mM Magnevist with ultrasound guidance [85]. Imaging was performed on a 7T magnet with a four-channel VarianINOVA console (Varian Inc., Palo Alto, CA) multiplexed to 16 coils for parallel imaging. A spin echo sequence was used: TR/TE=650/15 ms with isotropic voxels of $100\mu m$ and an imaging time of 13 h.

Application of the registration resulted in segmentations of the limbs and six major organs: heart, spleen, lungs, kidneys, liver and stomach. See Fig. 2.6 and Fig. 2.7, where the obtained results are presented in 2D and 3D visualizations respectively. Tab. 2.3 shows the Dice coefficients for the heart, the lungs, the kidneys and the liver.

In all the abovementioned application examples, experiments were executed using MATLAB R2008b (The Mathworks,Natick, USA) and took always ≤ 6 minutes of runtime on a 2.40 GHz Intel Quad Core Windows PC with 4 GB of RAM.

2.4   Discussion and Conclusions

This paper introduces three realistic, articulated skeleton phantoms derived from publicly available small animal atlases: Digimouse [36], MOBY mouse [59] SD rat atlas [60,61]. A number of application examples using the MOBY atlas for such articulated atlases were presented. Mainly, it was demonstrated that articulated atlases can be used in correcting the postural variation, in referencing optical to CT data and in organ approximation. By combining the atlas with a hierarchical anatomical model and articulated registration, whole-body skeleton registration could be performed robustly, even in the presence of large postural variations: all 14 MicroCT datasets could be registered successfully. For

the skeleton, a registration accuracy within two voxel dimensions was achieved. This performance is comparable to the results given in [26]. However, that method takes several hours while the method presented here takes less than 10 minutes. Regarding the joint localization error, suboptimal registration results can occur where two adjacent long bones are pointing in almost the same direction. In some of these cases, the resulting scaling factor along the longitudinal bone axis was the maximum value that was considered anatomically realistic (scaling by 15%). As a result, parts of the distal bones were erroneously assigned to target bone during registration. Due to animal placement during acquisition, this mainly is a problem for the ankle joint and is reflected in the somewhat higher error. Also, the results for the joint localization errors are comparable to those reported in literature [25].

The obtained results for the semi-automatic atlas to MRI data approximation were generally satisfactory and similar to the manual segmentations (heart, kidneys, liver), while for other organs the atlas approximations are more variable (organs with inherent shape variability such as the stomach and spleen) and errors were larger. The calculated Dice coefficients reveal "moderate" (0.41-0.6 [88]) performance for the lungs and mostly "substantial" (0.61-0.80) or "excellent" (>0.7 [89]) performance for heart, liver and kidneys. The comparison of the calculated Dice coefficients with previously published results shows that while performing better than [20] and at a similar level as [87], the proposed method does not obtain as good results for the lungs as the method proposed in [86] (see Tab. 2.3). However, the examples given in Fig. 2.3 and Fig. 2.7 reveal that the proposed TPS mapping of the major organs leads to a realistic approximation and can be used by biologists for qualitative anatomical referencing. Also, in the context of the intended application of combining segmented 3D data and BLI, the achieved accuracy should suffice to define a heterogeneous tissue model for Bioluminescence Tomography, since it has been shown, that integration of heterogeneous tissue properties yields a more accurate BLI source reconstruction than relying on a homogeneous tissue model [90].

At the moment, MicroCT data is required to perform the whole-body segmentation step. To be able to obtain whole-body segmentation also in the absence of MicroCT data, without putting restrictions on the positioning of the animals during data acquisition, a method is under development to register the modified Digimouse atlas to a 3D distance map, which is derived from multiple photographs. This is especially interesting for cases, where researchers are interested mainly in quantification of the light source. If morphological changes have to be studied in detail over time, a MicroCT scan would still be required. However, since these usually occur at a later point in time, CT data acquisition could be omitted at early time points and therefore reduce radiation burden of the animals.

The strategy applied here to make the atlases articulated was outlined to deal with major postural variations (involving long bones or large bone complexes). However, it can be extended to the whole skeleton to cope with any minor variation. One can define a kinematic model for each vertebra of the columna vertebralis (whereas here the columna vertebralis is defined as one big bone complex) and even to some nonrigid organs. Also, it is important to note that often, depending on the task at hand, the DoFs for each bone/bone complex can be defined or redefined accordingly. In [17] for example, some

additional DoFs were allowed, although they are anatomically unnecessary, to compensate for errors that have been made during the specific task of whole-body atlas to 3D mouse data registration.

The presented articulated models were made publicly available and can be downloaded from the "Articulated Atlas Downloads" section at http://www.lkeb.nl.

Acknowledgements

Appendix

Comparison of the Three Original Atlases
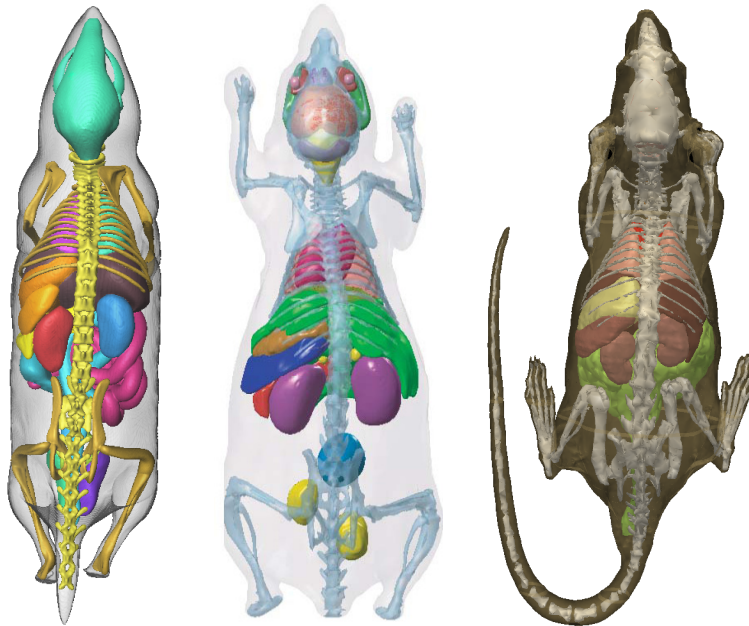
Figure 2.8: Illustration of the three original atlases (left to right): MOBY, Digimouse and SD Rat.

Chapter 2

Table 2.4: Comparison between the three atlases. The 'x' indicates available structures.

	Moby mouse	Digimouse	SD Rat
Origin	John Hopkins Univ.	Univ. of Southern California	Huazhong Univ. of Science and Technol.
Strain	C57BL/6	NA, nude	Sprague-Dawley (SD)
Gender	male	male	male
Age	15, 16 weeks	adult	$\approx$ 2 months
Number of Cryosections	NA	418	9475
Cryosection Image Size	NA	1740 x 2560	4600 x 2580 (24-bit)
Weight	$\approx$ 30g	28g	156g - 190g
Resolution	$110\mu m$ (isotropic)	$100\mu m$ (isotropic)	$20\mu m$ (isotropic)
Modalities	MRI	CT, PET, Cryosections	Cryosections
Data Processing	SURFdriver, Rhinoceros NURBS	ImageJ, RVIEW, LEREG, MATLAB, BrainSuite	Photoshop, VTK
Website	http://dmip1.rad.jhmi.edu/xcat/	http://neuroimage.usc.edu/Digimouse.html	http://vchibp.vicp.net/VCH/Mice/tech.html
Skeleton	x	x	x
Skeleton Labels	Ribs, Spine, Skull, Rest		
Skin Surface	x	x	x
Esophagus			x
Stomach	x	x	x
Stomach Labels	Wall, Contents		
Intestines	x		x
Intestine Labels	Large, Small, Air		
Liver	x	x	x
Lungs	x	x	x
Kidneys	x	x	x
Heart	x	x	x
Heart Labels	LV & RV & LA & RA myocardium, LV & RV & LA & RA blood pool		
Spleen	x	x	x
Brain	x	x	x
Brain Labels	Neocortical white & gray matter, Cerebellum white & gray matter & nuclei, Thalamus, Hippocampus	Cerebrum, Cerebellum, Olfactory Bulbs, Striatum, Medulla	
Masseter muscles		x	
Eyes		x	
Lachrymal glands		x	
Pancreas	x	x	
Adrenal glands		x	
Testes	x	x	
Bladder	x	x	
Vas deferens	x	x	
Thyroid	x		

Articulated Whole-Body Atlases for Small Animal Image Analysis

3

Atlas-Based Whole-Body Segmentation of Mice from Low-Contrast MicroCT Data

Chapter 3

Abstract

This paper presents a fully automated method for atlas-based whole-body segmentation in non-contrast-enhanced MicroCT data of mice. The position and posture of mice in such studies may vary to a large extent, complicating data comparison in cross-sectional and follow-up studies. Moreover, MicroCT typically yields only poor soft tissue contrast for abdominal organs. To overcome these challenges, we propose a method that divides the problem into an atlas constrained registration, based on high-contrast organs in MicroCT (skeleton, lungs and skin), and a soft tissue approximation step for low-contrast organs. We first present a modification of the MOBY mouse atlas (Segars *et al.* 2004) by partitioning the skeleton into individual bones, by adding anatomically realistic joint types and by defining a hierarchical atlas tree description. The individual bones as well as the lungs of this adapted MOBY atlas are then registered one by one by traversing the model tree hierarchy. To this end, we employ the Iterative Closest Point method and constrain the Degrees of Freedom of the local registration, dependent on the joint type and motion range. This atlas-based strategy renders the method highly robust to exceptionally large postural differences among scans and to moderate pathological bone deformations. The skin of the torso is registered by employing a novel method for matching distributions of geodesic distances locally, constrained by the registered skeleton. Because of the absence of image contrast between abdominal organs, they are interpolated from the atlas to the subject domain using Thin-Plate-Spline approximation, defined by correspondences on the already established registration of high-contrast structures (bones, lungs and skin).

We extensively evaluate the proposed registration method, using 26 *non-contrast-enhanced* MicroCT datasets of mice, and the skin registration and organ interpolation, using *contrast-enhanced* MicroCT datasets of 15 mice. The posture and shape varied significantly among the animals and the data was acquired *in vivo*. After registration, the mean Euclidean distance was less than two voxel dimensions for the skeleton and the lungs respectively and less than one voxel dimension for the skin. Dice coefficients of volume overlap between manually segmented and interpolated skeleton and organs vary between 0.47 ± 0.08 for the kidneys and 0.73 ± 0.04 for the brain. These experiments demonstrate the method's effectiveness for overcoming exceptionally large variations in posture, yielding acceptable approximation accuracy even in the absence of soft tissue contrast in *in vivo* MicroCT data, without requiring user initialization.

Atlas-Based Whole-Body Segmentation of Mice from MicroCT data

3.1   Introduction

3.1.1   Background

MOLECULAR IMAGING modalities are nowadays regarded as powerful tools for pre-clinical (small animal) research, especially for characterization and quantification of molecular processes *in vivo* [2]. In contrast to traditional structural imaging methods in diagnostic medicine, their aim is to determine disease-related abnormalities at a microscopic (cellular) scale at an early stage and to subsequently correlate these with macroscopic anatomical changes over time [3]. This adds a new dimension to animal experiments, since the traditional cross-sectional studies using different animals can be extended to follow-up studies, using the same animal.

While sometimes researchers are interested in imaging molecular events in a specific target organ, e.g. the brain or the heart, it is often necessary to acquire data from the entire animal. This is particularly important in oncology, where researchers aim at monitoring metastatic disease, to answer questions like where in the body particular tumor cells metastasize, and to follow tumor growth and interaction with its environment [5,6]. Bioluminescence Imaging (BLI) and Fluorescence Imaging (FLI) are useful modalities for this purpose because of their high sensitivity but in general do not provide anatomical reference information. Therefore, BLI or FLI datasets are often combined (fused) with high-resolution diffuse light photographs and coregistered MicroCT datasets. Although we earlier demonstrated that this improves visual data navigation [7], the localization of a particular structure of interest remains challenging if the structure of interest does not show sufficient contrast, for instance for abdominal organs in MicroCT. An automated whole-body segmentation of the entire animal, including the skeleton, would therefore greatly facilitate data interpretation. Moreover, a whole-body segmentation can be useful to localize and quantify bioluminescence sources, because accurate Bioluminescence Tomography (BLT) approaches require a heterogeneous tissue model [90,91].

Since light propagation in tissue is highly diffusive and light has a very limited penetration depth, the positioning of the animal in the BLI and FLI data acquisition device is strongly dependent on the type of study. If there are e.g. metastases in the spine, the animal should be positioned such, that the back of the animal is directed toward the CCD camera. Therefore, the data acquisition protocol cannot be standardized and the animal posture and shape may vary significantly among different animals in a cross-sectional study or the same animal in a follow-up study. The reason is that an animal body consists of many individual (rigid) bones next to multiple (nonrigid) organs and other soft tissues, which renders the animal interior largely heterogeneous. Besides the shape variability of these individual parts, there exists an additional variability in location relative to each other, which is especially the case for the distal parts of the skeletal system (limbs). Above that, being the modality of choice for bone imaging, non-contrast-enhanced MicroCT shows poor soft tissue contrast (Fig. 1.3, right). This complicates data comparison, especially in the abdominal cavity.

The goal of this work is to provide a fully automated, atlas driven method for whole-body segmentation of mice. To deal with follow-up as well as cross-sectional data, the
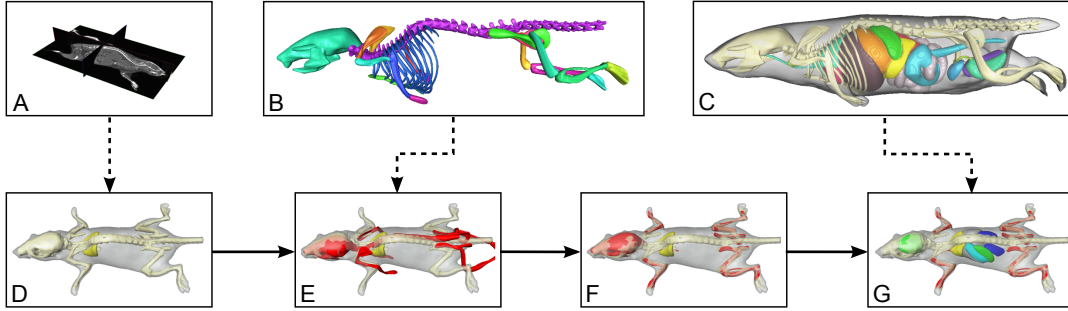
Figure 3.1: Overview of the registration and organ approximation process. First, high contrast structures (the skeleton, the skin and the lungs) are extracted from the CT data of a given subject (A). Subsequently the atlas skeleton (B) and lungs and the extracted skeleton and lungs (D) are registered (E and F) using an anatomically realistic kinematic model. Finally, major organs are mapped from the atlas (C) to the subject domain (G). (The dashed arrows indicate the data input i.e. the CT data and the atlas).

method should be able to handle anatomical intersubject data and exceptionally high variability in posture and shape between timepoints and individuals. Moreover, the method should be robust with respect to moderate bone malformations (e.g. as a result of metastatic activity) and with respect to low soft-tissue contrast. Primary application in this paper is non-contrast-enhanced MicroCT data, acquired *in vivo*.

3.1.2 Related work

The amount of Degrees of Freedom (DoF) that a registration method has to resolve is related to the shape variability of the registration object and can become very large for nonrigid structures. A generic whole-body registration approach not only has to deal with a large shape variability of individual parts of the body, but in addition with the large postural variability of the entire body. This requires a tradeoff between an enormous amount of DoFs and deformation constraints to ensure that the individual elements of the body are transformed in an anatomically realistic way, e.g. stiff structures like bones should not be deformed as much as soft tissue structures.

Methods that aim at registration of individual anatomical structures have been extensively surveyed in the literature [12–15]. Therefore in the following, only registration strategies that are suitable to handle objects with inherent structural diversity and methods, specifically tailored for small animal whole-body registration, are reviewed.

Several strategies have been reported to tackle the aforementioned difficulties of whole-body registration. There are basically two types of approaches:

1. Methods that solve for a global transformation function directly [20, 26] and

2. Methods that are based on a set of local transformations, derived using (hierarchical) block-matching [18] or using an underlying anatomical model [32, 33, 35]. The global transformation is subsequently determined by combining the local transformations.

Atlas-Based Whole-Body Segmentation of Mice from MicroCT data

Chaudhari *et al.* [20] determine a diffeomorphic transformation between the skin surface of the Digimouse 3D atlas [36] and a subject skin, derived from MicroCT data. They segment the animal interior by surface-constrained warping of the atlas volume to the subject using harmonic maps, based on the skin mapping result. The method to a certain extent handles variations in limb position by manually drawing curves on the limbs, but does not take internal structural differences into account. Bone structures therefore can easily deform in an anatomically non-realistic way. A method that takes special care of the skeleton is presented in Li *et al.* [26]. The authors present a whole-body intersubject, intramodality (CT) approach for *ex vivo* mouse studies. They nonrigidly register centerline representations of different animal skeletons and subsequently use the correspondences to define a Thin-Plate-Spline (TPS) mapping. As a final step, they apply an intensity-based nonrigid registration. Their work is based on the skeleton and therefore distinguishes between bone and soft tissue in general. However, there is no further identification of soft tissue parts. Above that, the point matching method cannot handle large limb articulations.

A way to take local differences in tissue properties into account during registration are block-matching methods. Depending on the target, the transformation model can be adjusted to fit the deformations locally. Approaches have been presented for various applications allowing translation only [28], translation and rotation [29] or affine [30, 31] local transformations. Kovacevic *et al.* [18] apply a hierarchical block-matching method for whole-body, intramodality registration of MRI data, using locally affine transformations. The approach is based on the "part-of" concept, i.e. they first separate the main organ compound and refine that division as the registration progresses, down to single bones and organs. A drawback of block-matching methods reported in the literature is that, although the individual transformations are initialized by the registration result on a higher hierarchical level, the individual blocks are determined anatomically independent of each other. Therefore larger postural differences will lead to suboptimal results.

To deal with larger postural differences, several authors perform local registrations by integrating anatomically realistic motion constraints. Martín-Fernández *et al.* [32, 92] for example make use of an anatomical hand model to register 2D radiographs. The bones are thereby represented by a wireframe where individual 'rods' are registered imposing kinematic constraints. Du Bois d'Aische *et al.* [33] register a human head, based on a model of the cervical spine. Articulated vertebrae are registered to the target image and the deformation is propagated to the rest of the head using a linear elastic model. Papademetris *et al.* [35] use a kinematic model to register the legs of a mouse by modeling the joints. Articulated parts thereby have to be segmented manually. After registration, they propagate the deformations to soft tissue parts by focusing on the folding problem at interfaces of articulated parts. Although they show the applicability of such an approach for small animal registration, they focus on a subpart of the body.

In summary, some available methods can be used either for whole-body applications, as long as differences in posture and shape are small. Some authors use animal holders or place the animals in a similar position for each scan. Other methods include *a priori* information, for instance about structural properties of single elements of the object, about kinematics of elements relative to each other or about position and spatial extent of

anatomical objects but again, allow small articulations only or were used for registration of subparts of a body. Often the method is only suitable for intramodality applications [18, 26] and registration is therefore restricted to image features that show sufficient contrast in the used modality. The required amount of user interaction e.g. to define joint locations or to generate labeled datasets [35] or computational demands [26] makes some methods laborious. Moreover, the aforementioned methods for small animal applications were evaluated either using synthetic data [18] or using only few subjects [20, 26, 35].

3.1.3 Contributions

In this work we present an automated method for whole-body segmentation of MicroCT datasets of mice using atlas-based registration. To accommodate for large postural variations between scans or animals, the DoFs in the registration are governed by realistic kinematic constraints on the animal skeleton in a coarse-to-fine manner: after global alignment, individual bones are registered locally, subject to a hierarchical model of the skeleton that includes anatomically realistic motion constraints in the joints. The registration is driven by high-contrast anatomical structures (bones, lungs and skin) included in the matching hierarchy. To compensate for missing registration features in MicroCT (most organs and soft tissue), we rely on a publicly available whole-body mouse atlas (the MOBY atlas [59]). Abdominal organs with low contrast are estimated using Thin-Plate-Splines (TPS) interpolation [80], after establishing a dense set of correspondences between the high-contrast structures in the data and the atlas.

The novel elements in this work are:

- We extend the MOBY atlas by partitioning the static skeleton into individual bones, and defining anatomically realistic kinematic constraints for each joint.

- We define a hierarchical anatomical model of the animal body for automated registration of the MOBY atlas.

- We describe a novel algorithm to determine dense correspondences on the animal skin based on an initial set of sparse correspondences, using matching of local distributions of geodesic distances.

- We validate our approach using 41 MicroCT datasets of mice scanned in arbitrary posture. To the best of our knowledge this represents the most extensive validation reported for whole-body small animal segmentation.

Pilot studies on the methods in this work were presented previously [86, 93].

3.2 Methodology

An overview of the presented approach is given in Fig. 3.1. First the anatomical atlas modifications (Fig. 3.1, B) as well as the hierarchical anatomical model are introduced
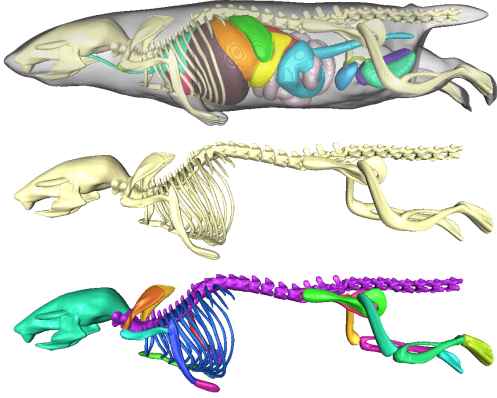
Figure 3.2: *The mouse atlas (top), the skeleton as originally included in the atlas (middle) and after segmentation of individual bones (bottom). The colors indicate different bones.*
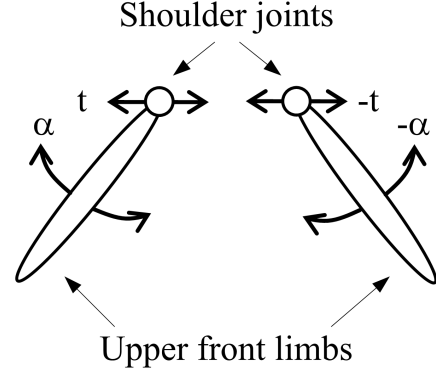
Figure 3.3: *Representation of the shoulder complex. Besides global DoFs, a symmetric translation t and rotation α with respect to the shoulder joints are allowed.*

(section 3.2.1). Details about the automated extraction of the high-contrast organs (skeleton, lungs and skin) are given in section 3.2.2 (Fig. 3.1, D). Next, the registration of the individual parts of the hierarchy, namely the global registration of the entire skeleton (Fig. 3.1, E) and the local registration of individual structures (Fig. 3.1, F) are given in section 3.2.3. The determination of skin correspondence is introduced in section 3.2.4 and section 3.2.5 describes how skeleton, lung and skin correspondence is used for low-contrast organ interpolation (Fig. 3.1, G).

3.2.1 Atlas adaptations and anatomical model definition

The atlas used in this work was originally developed by Segars *et al.* [59]. It is a 4D whole-body anatomical mouse model including bones and organs that allows to simulate breathing and heart motion. For this work, an instance of the model was generated at a fixed time point in the respiratory and cardiac cycle at end diastole and full exhale (Fig. 3.2, top). The skeleton is represented as a whole and does not distinguish between individual bones (Fig. 3.2, middle). To integrate rotational DoFs in the joints, we segmented the individual bones using Amira 3.1 (Mercury Computer Systems, Chelmsford, USA), guided by anatomical text books [76, 77], yielding a labeled volume dataset with voxel size 90 μm $\times$ 90 μm $\times$ 90 μm. Subsequently, triangulated surface representations of all bones, the organs and the skin were generated using the Marching Cubes Algorithm [94]. A surface representation of the segmented skeleton is given in Fig. 3.2 (bottom). Based on the segmented bones and lungs, a set of characteristic anatomical landmarks at distinctive locations like the joint pivot points, the caudal end of the skull etc. was defined manually on the surfaces and the skin surface was partitioned into torso and limbs. Second, local coordinate systems for each bone were defined such that the realistic bone articulation for each joint could be expressed more intuitively, e.g. the knee rotation axis and the longitudinal axis of the tibia were chosen to be coordinate axes of
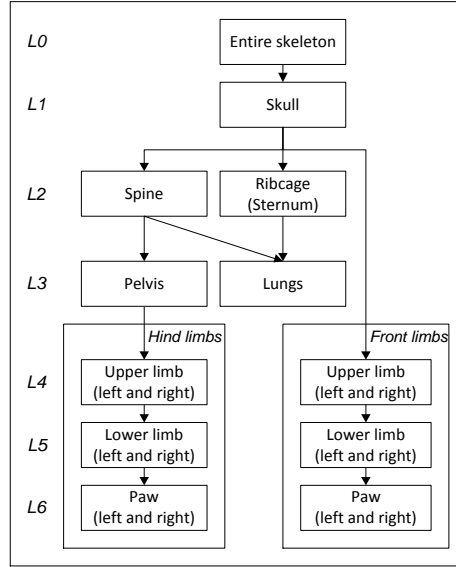
Figure 3.4: Hierarchical anatomical tree for the skeleton and the lungs. The connections depict relations between single bones or bone compounds such that a part on a lower level is initialized by the registration result on a high level.

the local coordinate system.

Three types of joints were distinguished: ball joints, hinge joints and the shoulder complex (both shoulders combined). Tab. 2.1 shows the DoFs for the ball and hinge joints. Due to the large number of DoFs in the shoulder, an additional motion constraint was introduced by allowing only a coupled, symmetric displacement of both front upper limbs, with a varying distance between the shoulders and a rotation toward and away from each other (Fig. 3.3). Subsequently, the left and the right front upper limbs are decoupled. The hierarchical anatomical tree of the animal skeleton and the lungs is shown in Fig. 3.4, containing the bones that determine the major posture variations. For capturing the animal posture, smaller skeletal elements such as the shoulder blades and individual paw bones were excluded. Assuming that the spine and the sternum sufficiently describe the global pose of the ribcage, individual ribs were removed from the data by applying appropriate preprocessing steps (see section 3.3.1), as indicated in Fig. 3.5. In principle, each of the 23 individual vertebrae in the mouse body could be separately modeled. However this would greatly increase the total amount of DoFs. To avoid this, we opted for modeling the spine as a 3D curve connecting the skull to the pelvis.

3.2.2 Robust extraction of registration features

The presented registration method relies on automatically extracting surface meshes of the high-contrast organs from MicroCT data (skeleton, skin, lungs), and several interchangeable processing pipelines can be envisioned that produce these meshes automatically. We opted for extracting these meshes by smoothing the CT data to remove noise and small skeletal elements, followed by isodata thresholding (Ridler *et al.* [95]). The
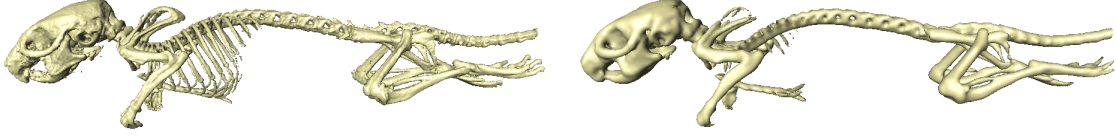
Figure 3.5: Isosurfaces of a mouse skeleton before (left) and after preprocessing (right).

resulting data volume was used for global skeleton alignment and spine determination, as described in section 3.2.3. The skin boundary of the animal was segmented from the smoothed data volume by isodata thresholding in one iteration (threshold t_1). For segmentation of the lungs, the triangle algorithm [96] was selected for its ability to classify lung tissue voxels in the absence of a clear lung peak in the MicroCT histogram . The required parameters were set to $b_{min} = t_1$ and b_{max} being the bin k of the 8-bit histogram h_{gray} where $h_{gray}(k > t_1)$ is maximal. Triangular surface meshes were extracted from the segmented volumes using the Marching Cubes Algorithm [94]. For the determination of the skin correspondences, the skin surfaces were simplified using the QSlim method by Garland *et al.* [97].

3.2.3 Registration of high-contrast organs

To initialize the hierarchical model registration, first a coarse alignment of the atlas and the target data on the highest hierarchical level ($L0$), i.e. the entire mouse skeleton, is performed. For this purpose, a similarity transformation model with seven DoFs is employed (translation, rotation, isotropic scaling), which suffices to accommodate for the animal pose in the CT scanner and for size differences between animals. The individual DoFs are resolved in several steps, which are based on a set of robust inherent features of the skeleton:

- Alignment of the anteroposterior axis of the animal, based on the Center of Gravity (CoG) and the first eigenvector of the skeleton, represented as a 3D point set, using Principal Component Analysis [98].

- Determination of the animal position (prone/supine) in the scanner, using a 3D curve representation of the skeleton. This is derived from the labeled skeleton volume by binning the data along the anteroposterior axis and calculating the CoG in each bin. Between the ribcage and the pelvis, the curve closely follows the spine. The course of the curve in this part allows deriving the animal position.

- Determination of the animal orientation, because the amount of bone is much larger in the cranial half.

- Determination of the neck location, based on the projection of the 3D curve to the coronal plane.

- Derivation of an initial scale factor from the total bone content of the skeletons.

An example of the result of the global alignment step is given in Fig. 3.8 (top row).

Following the coarse alignment of the entire skeleton, lower hierarchical tree levels are registered piece by piece. For the individual bones, transformation models according to Tab. 2.1 are used. We consider the amount of DoFs to be sufficient to model coarse anatomical bone differences among subjects. Adding more DoFs would lead to more accurate registration results but would compromise robustness with respect to large postural variations, especially if bones show pathological changes.

The transformation parameters for the individual bones are determined using the Iterative Closest Point (ICP) algorithm (Besl *et al.* [79]). It is a method that iteratively solves for transformation and correspondence, by minimizing the Euclidean distance between two point sets. Because of the restricted amount of DoFs of the individual transformations and the fact that a skeleton segmentation from CT data contains only few outliers, ICP offers the best tradeoff between robustness and computational burden for the problem at hand and therefore a more robust but more expensive method, e.g. the Robust Point Matching (RPM) framework [99], is not required. While ICP has originally been developed for incorporating rigid transformations only, non-isotropic scaling can be integrated as well. In this way, it is possible to account for anatomical intersubject variability in bone thickness and length.

The articulated registration of the skeleton is performed by traversing the hierarchical anatomical tree (Fig. 3.4) in a top-down manner i.e. starting at $L1$ and proceeding to the lowest level $L6$. At each step ICP is applied to the distal part of a joint, constrained by the respective joint type i.e. if e.g. the pelvis ($L3$) has been registered, the upper hind limb ($L4$) is registered subsequently, allowing the DoFs of a ball joint. The lungs ($L3$) are initialized based on the spine and the sternum. They are registered allowing 9 DoFs because during breathing, lungs expansion with respect to the longitudinal body axis differs significantly from the lateral expansion [100]. Elastic deformations are not modeled. After convergence of a structure, the final transformation function is used to initialize the registration of a bone at a lower hierarchical level. An example of the gradually improving overall registration error during stepwise registration of individual structures is given in Fig. 3.6.

Given the source point sets $X_k = \{x_{ki}, i = 1, 2, \ldots, M_k\}$ of the segmented atlas bones, the target point set $Y = \{y_j, j = 1, 2, \ldots, N\}$ of the skeleton segmented from CT, and the error measure E_k, the Euclidean distance between a source and the target surface, the registration is done as follows (note that X_k and Y are represented in homogeneous coordinates to enable matrix multiplications:

1: Determine the global transformation matrix T_0 that coarsely aligns the skeletons
2: **for** All k elements (bones and lungs) in the hierarchy **do**
3:     Obtain the local transformation matrices $T_1, \ldots, T_{k-1}$ of the elements on the higher levels in the hierarchy
4:     Define the parameter vector Θ_{init} for the current element
5:     Determine the transformation matrix $T_{local2global}$ that aligns the local to the global coordinate system
6:     Apply the ICP algorithm to the current element:
7:     **repeat**

00 Coarsely aligned skeleton
01 Skull
02 Right part of the pelvis
03 Right hind upper limb
04 Right hind lower limb
05 Right hind paw
06 Left part of the pelvis
07 Left hind upper limb
08 Left hind lower limb
09 Left hind paw
10 Sternum
11 Right front upper limb
12 Right front lower limb
13 Right front paw
14 Left front upper limb
15 Left front lower limb
16 Left front paw
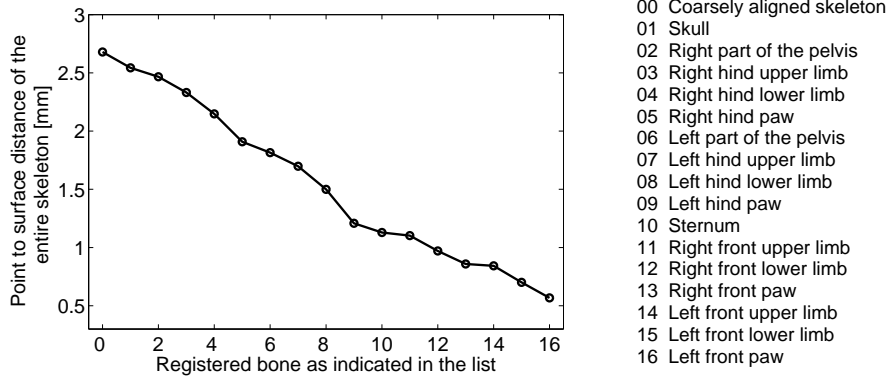
Figure 3.6: Improvement of the error criterion as the registration progresses down the anatomical tree ($1voxel \hat{=} 332 \mu$m).

8:     Define $\Theta_k = \Theta_{init}$ in the first or $\Theta_k = \Theta_{new}$ in subsequent iterations

9:     Determine the local transformation matrix $T(\Theta_k) = Trans(\Theta_k) * Rot(\Theta_k) * S(\Theta_k)$

10:    Determine the global transformation matrix $T_{total}(\Theta_k) = T_{local2global}^{-1} * T(\Theta_k) * T_{local2global} * T_{k-1} * \ldots * T_1 * T_0$ and transform the current element

11:    Calculate the error between the source and the target:

$$E(X, Y, T_{total}(\Theta_k)) =$$
$$\frac{1}{M_k} \sum_{i=1}^{M_k} \min_{j=1 \ldots N}(\|y_j - T_{total}(\Theta_k) * x_{ki}\|) \qquad (3.1)$$

12:    Search for another set of parameters Θ_{new} that yields a smaller error, using a trust-region approach that is based on the interior-reflective Newton method [101]

13:    **until** $|\Theta_k - \Theta_{new}| \leq \epsilon$, with ϵ being the user defined parameter tolerance

14: **end for**

The spinal centerline is extracted using three dimensional region growing, where a landmark at the skull-atlas connection serves as the seed point and the region growing is stopped when the vertebra connecting the spine to the pelvis is reached. The 26 intervertebra connections are subsequently mapped from the atlas to the subject, relative to the length of the spine.

3.2.4 Determination of skin correspondence

Because of the high variability of animal positioning during data acquisition, the shape of the animal skin surface may have high rotational symmetry with respect to the anteroposterior body axis (Fig. 3.1, C) and may be symmetric to the sagittal (Fig. 3.7) or the transverse plane. However, one can exploit the already registered skeleton and lungs to remove postural ambiguity, and thus derive a sparse set of correspondences on

the skin to provide landmark support over the entire animal surface [102, 103]. Following the skeleton registration, the manually defined landmarks in the atlas reference frame can be mapped to the target domain. As a result, the location of the atlas-annotated landmarks is known in the target domain as well. Since bone is adjacent to the skin at many locations in the animal body, an equal amount of skin correspondences can be derived by selecting the skin points closest to the bone and lungs landmarks. This sparse set of skin correspondences can only provide landmark support in regions where bones are present e.g. near to the spine. To determine a dense set of correspondences on the skin, a method is needed that handles abdominal deformations and articulated limbs.

Available methods that determine shape correspondence in the spatial domain, for example the RPM framework, have to include a transformation model to handle large nonlinear deformations. Another approach is to represent the shape intrinsically. This can be done e.g. by using Euclidean distances between points [104], rendering the representation invariant to rigid body transformations or by using geodesic distances (the shortest path between two points on a manifold), to obtain invariance to rigid body transformations and bending [105]. Using appropriate normalization of the representations, invariance to scaling can be obtained as well.

Elad *et al.* [105] used a bending invariant shape signature for classifying articulated shapes and Jain *et al.* [106] aimed on determining correspondence between articulated shapes. Both methods are based on global shape representations and therefore require a very densely sampled surface. This is necessary to ensure that the larger geodesic distances can be computed accurately. However, calculating a geodesic distance distribution for each node on a dense mesh is very time consuming. Given an initial set of correspondences on the surface it is possible to use a more local shape representation based on geodesic distances. This has the advantage of a reduced calculation time and that local shape variations are better represented. Above that, it is possible to use a coarser mesh sampling [107], which further reduces computational burden.

Our approach employs an intrinsic representation of the skin shape that is based on geodesic distances. We assume that elastic deformations i.e. stretching or compression of the skin play a minor role and that bending is the main form of deformation. We determine correspondence between two shapes by calculating distributions of geodesic distances locally, starting from the initial set of correspondences, and continue until the entire surface is covered. A method that is similar to ours was presented by Wang *et al.* [108], but their method requires a much larger set of initial correspondences.

Matching of local geodesic distributions

Given an initial sparse set of corresponding nodes on the source and the target surface, we determine new correspondences in the vicinity of each node in this sparse set, yielding an extended set of correspondences. The vicinity of a node is controlled by two fixed neighborhood parameters: a minimum distance g_{min}, to prevent that new correspondences are too close to already known correspondences and a maximum distance g_{max}, to ensure locality. (Details on the determination of the geodesic distances are given in the 'Appendix'). Subsequently, more correspondences are determined in the vicinity of the extended set and so on. The search for correspondences stops when there are no new

Atlas-Based Whole-Body Segmentation of Mice from MicroCT data
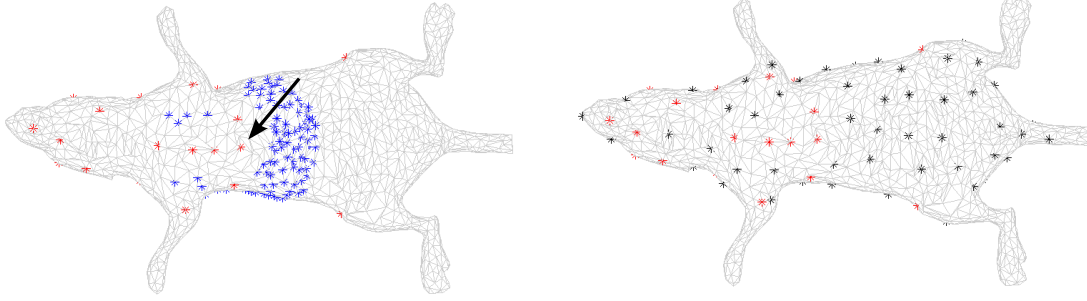
Figure 3.7: The images show an example skin surface in bottom view. Depicted are an initial sparse landmark set (red stars) and candidates for new correspondences (blue stars), based on a known landmark (arrow) on the chest (left). The final dense set of correspondences is indicated by black stars (right).

candidates left on the mesh. Parameter K controls how many already known correspondences are taken into account to derive the distribution of geodesic distances. To find optimal parameter values, g_{min} and g_{max} were fixed and K was determined as a tradeoff between the quality of the mapping and the processing time. The quality investigation was based on the mean distance between the source and the target skin surfaces, after determining correspondence and mapping the source to the target surface (mapping details are given in section 3.2.5) and on a triangle quality measure.

Let $P = \{p_i, i = 1, 2, \ldots, m\}$ and $Q = \{q_j, j = 1, 2, \ldots, n\}$ be the nodes of respectively the target and source surfaces to be matched, g_i and g_j be the geodesic distances between two nodes on P and Q and $h_i(k)$ with $k = 1, 2, \ldots, K$ and $h_j(k)$ with $k = 1, 2, \ldots, K$ be a distribution of local geodesic distances for the nodes $p_i \in P$ and $q_j \in Q$ based on K known correspondences on the surface. So $h_i(k)$ contains the geodesic distances from node p_i to K other nodes of P, in the vicinity of p_i and $h_j(k)$ contains the geodesic distances from node q_j to K nodes of Q, in the vicinity of q_j.

1: Determine geodesic distances for each node on the target surface to the remaining nodes (for the atlas skin surface, this calculation only has to be done once).
2: Initialize a list with the initial sparse set of corresponding nodes. (Shown as red stars in Fig. 3.7, left)
3: **repeat**
4: Select possible candidates for new correspondences on P and Q in a surface area of interest with respect to the next element on the list with $g_{max} > g_i > g_{min}$ and $g_{max} > g_j > g_{min}$. (Blue stars in Fig. 3.7, left)
5: Calculate $h_i(k)$ and $h_j(k)$ for all possible candidates in P and Q
6: **repeat**
7: Calculate the cost C_{ij} for matching two nodes p_i and q_j by using the χ^2 test statistic [104]:

$$C_{ij} = \frac{1}{2} \sum_{k=1}^{K} \frac{[h_i(k) - h_j(k)]^2}{h_i(k) + h_j(k)} \tag{3.2}$$
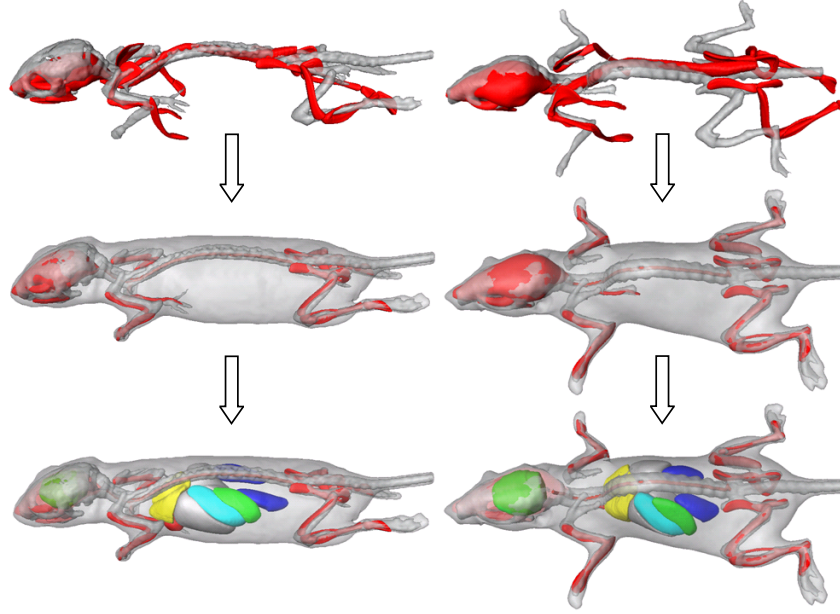
Figure 3.8: Registration results between the atlas (red) and two different subjects (gray) after coarsely aligning the skeleton (top), after the articulated registration (middle) and after organ interpolation (bottom).

8:      Find the best match $C_{min} = \min_{i,j}(C_{ij})$

9:      Add the nodes p_{Cmin} and q_{Cmin} to the list of correspondences

10:     Remove landmark candidates around p_{Cmin} and q_{Cmin} if $g_i \leq g_{min}$ or $g_j \leq g_{min}$

11:    **until** No landmark candidates are left on P

12: **until** No new elements in the correspondence list are left

An example of a mouse skin surface with a dense net of correspondences is shown in Fig. 3.7 (right).

3.2.5   Atlas organ interpolation

The established point correspondences (landmarks) on bone, lungs and skin provide sufficient data support to constrain a nonrigid mapping of organs from the atlas domain to the subject domain for the entire body. For this purpose, we chose Thin-Plate-Spline (TPS) interpolation [80, 109] because correspondences can be distributed non-uniformly within the image domain and the transformation can be determined analytically.

A TPS transformation is based on the combination of a set of radial basis functions (RBF) whose coefficients determine the displacement field. RBFs are functions of the Euclidean distance between an interpolation point $\mathbf{x}$ and a landmark point $\mathbf{x}_i$, based on a kernel $R_i = R(|\mathbf{x} - \mathbf{x}_i|)$. The RBF for TPS interpolation has the form:

$$f(\mathbf{x}) = \sum_{i=1}^{n} w_i R_i \qquad (3.3)$$

Atlas-Based Whole-Body Segmentation of Mice from MicroCT data
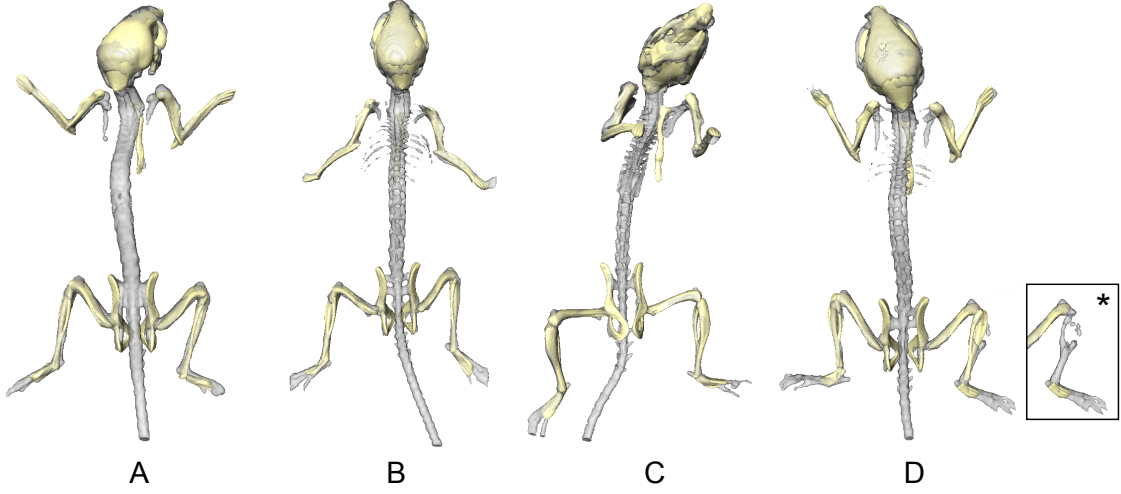
Figure 3.9: Several examples of skeleton registration results. The subject skeletons are shown in gray and the atlas bones in yellow. Three mice were in prone (A, B, D) and one mouse in supine position (C) respectively. The last example shows the result of an additional experiment to demonstrate the robustness of the method with respect to moderate bone resorption. The tibia without the registered bone is shown in the framed box (*).

with in 3D, $R_i = |\mathbf{x} - \mathbf{x}_i|$ [110], n is the amount of landmarks and w_i are the coefficients.

TPS interpolation also includes a global, linear (affine) component and so the TPS transformation $\mathbf{u}$ is determined as:

$$\mathbf{u}(\mathbf{x}) = \mathbf{A}\mathbf{x} + \mathbf{B} + \sum_{i=1}^{n} w_i R_i \tag{3.4}$$

$\mathbf{A}$ and $\mathbf{B}$ are coefficient matrices of the affine part of the transformation.

In its original form, TPS interpolation maps a set of source points $\mathbf{p}_i$ to their corresponding target points $\mathbf{q}_i$, with $i = 1, \ldots, n$, exactly. The smoothness of the interpolation is ensured because the transformation $\mathbf{u}$ minimizes an energy functional J_{TPS} that represents the bending energy of $\mathbf{u}$ [80]. However, exact landmark matching implies that the landmark locations should be known exactly, especially for landmarks that are in close proximity to each other, to ensure that the transformation remains invertible. In our case, a node on the target skin, with a specific distribution of geodesic distances, may not have an exact match on the source skin because of the discretization of the surface. This may lead to small landmark localization errors. To deal with such errors, approximating TPS (Rohr *et al.* [111]) have been proposed. The method is similar to smoothing TPS [109] but has the advantage that a localization uncertainty can be added for each landmark individually. This is formulated into an energy functional J_λ, where J_{TPS} is incorporated by means of a regularization parameter λ:

$$J_\lambda(\mathbf{u}) = \frac{1}{n} \sum_{i=1}^{n} \frac{|\mathbf{q}_i - \mathbf{u}(\mathbf{p}_i)|^2}{\sigma_i^2} + \lambda J_{TPS}(\mathbf{u}) \tag{3.5}$$
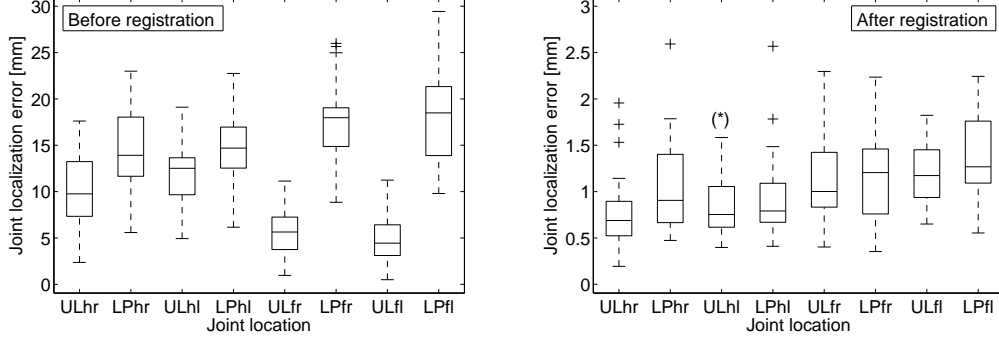
Figure 3.10: Boxplots of the joint localization errors for the limb joints (U = upper limb, L = lower limb, P = Paw, h = hind, f = front, r = right, l = left) before (left) and after the articulated registration (right). (*) There exists a joint localization error at 4.408 mm for this joint location that is not shown in the Figure (1voxel≘332 μm).

The first term measures the distance between the corresponding point sets $\mathbf{q}_i$ and $\mathbf{u}(\mathbf{p}_i)$ i.e. between n target points and n source points $\mathbf{p}_i$, mapped to the target domain by $\mathbf{u}$. Isotropic landmark localization errors can be integrated using the weighting factors σ_i, for each landmark individually. Depending on how smooth the final transformation should be, λ has to be chosen accordingly ($\lambda_{norm} = 0$: interpolation, $\lambda_{norm} = 0.1$: nearly affine transformation, $\lambda_{norm} = 0.001$: intermediate value). Like with conventional TPS, the transformation $\mathbf{u}$ of the approximating TPS can be determined analytically [111].

3.3 Experimental setup

Several experiments were executed to evaluate different aspects of the developed method. Experiments were performed on two different types of data, therefore the following sections are separated accordingly:

1. Assessment of the registration performance for the skeleton and the lungs, using *non-contrast-enhanced* data

2. Evaluation of skin landmark errors and organ interpolation performance, using *contrast-enhanced* data

3.3.1 Evaluation of skeleton and lungs registration

Data acquisition and preprocessing

For evaluation of the registration errors in skeleton and lungs, twenty-six data sets were acquired from twenty-one healthy, 6- to 10-week-old mice (Balb/c, Charles River WIGA, Sulzfeld, Germany), 20 female and 1 male, with a mean weight of 21.7g±2.2g, in prone and supine position and with arbitrary limb position. In total, 180 images were taken with step size 1°, using a Skyscan 1178 MicroCT (Kontich, Belgium), with 50keV x-ray

Atlas-Based Whole-Body Segmentation of Mice from MicroCT data
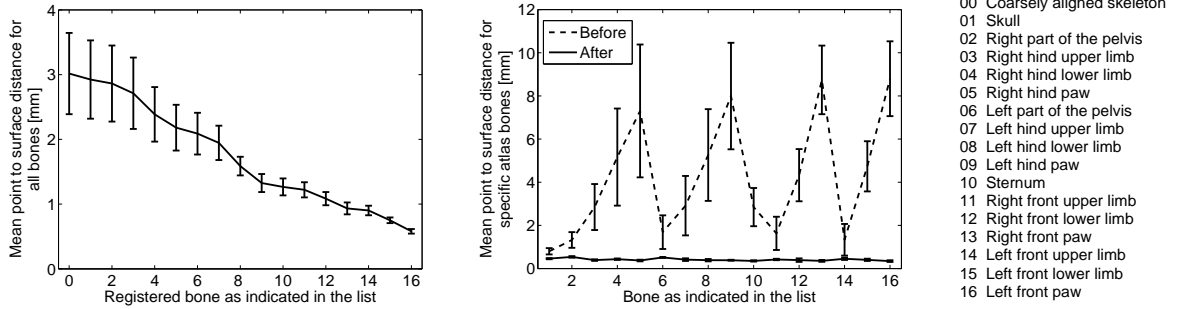
Figure 3.11: Overall mean error improvement during traversing the anatomical tree and mean error for specific bones before and after registration (1voxel≙332 μm).

voltage, an anode current of 200μA, an aluminum filter of 0.5mm thickness, an exposure time of 640ms and *without* using a contrast agent. The reconstructed datasets covered the range between -1000 (air) and +1000 (bone) Hounsfield units (HU). Neither cardiac nor respiratory gating was used.

The data with resolution 83 μm × 83 μm × 83 μm was subsampled by averaging with a factor of 4, yielding a voxel size of 332 μm × 332 μm × 332 μm, and smoothed using a Gaussian filter with kernel = 5 and sigma = 3. Subsequently, the skeleton, the skin and the lungs were segmented according to section 3.2.2. Triangular meshes were generated with ≈ 20000 nodes for the atlas skeleton (without ribs, spine and shoulder blades) and ≈ 30000 nodes for the CT skeleton surface. For skeleton registration, the set of atlas and subject surface nodes was reduced by factor 10. The lungs were represented with ≈ 400 nodes for the atlas and with ≈ 500 nodes for the CT surface.

Matching parameters

For each tree level (except $L0$), the registration was performed in two iterations. The first iteration involved was used for coarse rigid alignment allowing 6 DoFs i.e. translation and rotation in 3D, covering the entire anatomically realistic range of motion. Although not anatomically realistic for ball and hinge joints, translation was allowed to a small extent, to ensure that registration inaccuracies do not influence lower hierarchical levels. The second iteration incorporated non-isotropic scaling ($\leq 15\%$), allowing 9 DoFs. The minimization was terminated when the difference between subsequent parameter estimates was below 0.01 degrees for the rotation, 3.2 μm for the translation and 0.001 (0.1%) for the scaling parameters.

Evaluation metrics for skeleton and lung registration

To evaluate the skeleton registration performance, joint localization errors were calculated. These were expressed as the Euclidean distance between corresponding anatomical landmarks (point to point distance). To this end, the locations of the upper-lower limb and the lower limb-paw joints of all 26 data sets were indicated manually using the extracted skeleton surfaces. The difference in measured length of corresponding bones

on the right and the left side of the animal thereby gives an indication of the manual joint localization error (0.38 ± 0.25 mm, which is in the order of the data resolution). For validation, the found joint locations were compared to those determined after registration of the skeleton.

To assess the performance in areas where anatomical landmarks cannot be located manually in a reliable manner (on large parts of the bones and the lungs), the point to surface distance was determined to quantify border positioning errors, yielding an indication of the registration error of the entire object.

3.3.2 Evaluation of the skin and organ mapping

Data acquisition and preprocessing

The accuracy of the organ interpolation was determined based on datasets presented in Henning *et al.* 2008 [112]. These were acquired from fifteen healthy, 4- to 6-week-old female mice (C3H, Charles River WIGA, Sulzfeld, Germany), with a mean weight of 17.8g±0.83g, in prone position and with arbitrary limb position. The CT system was a MicroCAT II (ImTek Inc, Knoxville, TN), with 70keV x-ray voltage, an anode current of 500μA, an aluminum filter of 0.5mm thickness and an exposure time of 300-500ms. In total, 360 images were taken with step size $1°$ and *with injected contrast agent* Fenestra LC (ART Inc., Montreal, Canada), which is particularly suitable for increasing liver and spleen contrast. Neither cardiac nor respiratory gating was used.

Note that the contrast enhancement was only used for manual segmentation of organs to assess the performance of the organ interpolation. It was *not* used during registration as a registration feature. Although the strain of the animals in this dataset was different from the strain used for the skeleton registration validation, in our experience bone dimensions are very similar. For the femur, this has been shown in [77] (however, the density and thus the bone volume differ). For the lungs, longitudinal expansion is significantly larger for C3H mice [100].

In all the datasets the liver, the lungs and the spleen were segmented manually, based on their large contrast with respect to the surrounding tissue. The brain did not show an increased contrast but its extent is strongly restricted by the skull. Also the kidneys are not enhanced but show sufficient contrast with surrounding tissues (liver, spleen and abdominal fat deposits) for segmentation. In a subset of five datasets, the heart was also segmented, because these datasets were acquired within 30 minutes after Fenestra administration, yielding high contrast in the heart and vascular system.

To ensure the same conditions as for the skeleton registration evaluation, the data was preprocessed and the skeleton, the lungs as well as the skin were extracted in the same manner as presented in section 3.3.1. Only the subsampling parameter has been adjusted to 2, since the original resolution of the contrast-enhanced datasets was lower ($107~\mu$m $\times~107~\mu$m $\times~107~\mu$m).

Atlas-Based Whole-Body Segmentation of Mice from MicroCT data

Matching parameters

To determine skin correspondences, meshes were used with ≈ 7500 vertices for the atlas and ≈ 2000 vertices for the subjects. To derive the dense set of corresponding nodes, the parameters g_{min} and g_{max} were chosen such that the amount of correspondences is sufficient for the torso (relatively small surface curvature) and that almost the entire animal surface could be covered in three iterations. With $g_{min} = 15$ ($1 voxel \hat{=} 214$ μm) and $g_{max} = 50$, $K = 8$ was determined, based on the criteria described in section 3.2.4 (A detailed motivation for the selection of K is given in the 'Appendix'). The initial sparse set of correspondences was replenished by ≈ 120 nodes from the skin, all over the torso. Together with 30 correspondences on the surface of the lungs and the 32 anatomical landmarks, ≈ 182 corresponding nodes were used for mapping of the skin and major organs from the atlas domain to the subject domain. The regularization parameter for the approximating TPS was set to $\lambda = 1000$, yielding $\lambda_{norm} = \frac{\lambda}{x\_dim * y\_dim * z\_dim} = \frac{1000}{160*150*400} \approx 0.0001$ [111]. Since the initial sparse set of landmarks are considered as highly accurate, we assume a variance of $\sigma = 0.01$. All newly determined correspondences are considered as less accurate $\sigma = 2.2$ (the mean internode distance of the atlas skin surface is ≈ 5). During the experiments, the smoothness of the mapping was monitored using the determinant of the Jacobian of the final transformation, which was positive in all cases (more details are presented in the 'Appendix').

Fig. 3.8 shows two examples of mice with registered skeleton and approximated organs.

Evaluation metrics for the skin and the organs

For evaluation of the skin registration error, the Euclidean point to surface distance was employed. Note that this experiment was performed with a net density of skin correspondences that was appropriate for the torso and therefore the calculated surface distance does not include the limbs.

To assess the organ interpolation performance, the Dice coefficient s [81] was computed. This measure takes two individual absolute volumes V_1 and V_2 as well as their overlap into account and is defined as follows:

$$s = 2 \frac{|V_1 \cap V_2|}{|V_1| + |V_2|} \tag{3.6}$$

The stomach, spleen and intestines were not considered for determining dice coefficients, because of the large environmentally dependent variability in shape and location.

All experiments were run using Matlab 2007b (The Mathworks, Natick, USA). The time requirements are ≈ 3 mins for the data preprocessing and the articulated skeleton and lungs registration, ≈ 3 mins for calculating the geodesic distances and ≈ 3 mins to determine the dense landmark correspondences on the skin and warping the organs.
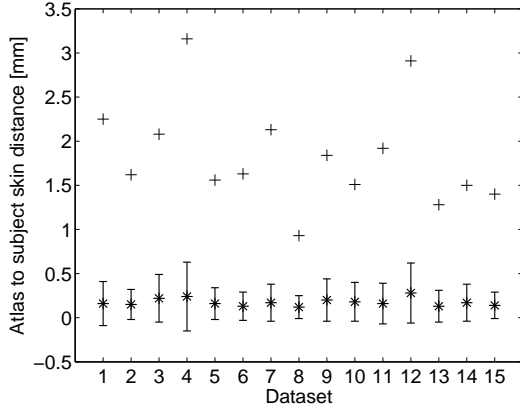
Figure 3.12: The mean atlas to surface distance after registration for the contrast-enhanced datasets. Maximum values are indicated with plus signs. (1voxel≙214 μm).
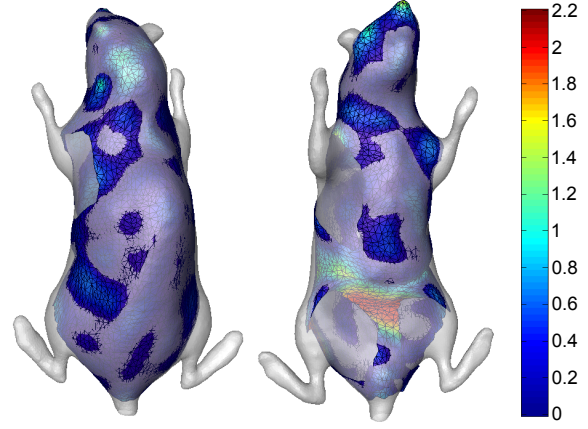
Figure 3.13: An original (gray) and an approximated animal skin. The colorcoding represents the Euclidean distance between the two surfaces (units in millimeters).

3.4 Results

3.4.1 Skeleton and lung registration

In all 26 cases, the matching converged to a correct solution from the automatically estimated initial position. Fig. 3.9 shows several examples of animals in prone and supine position. The Euclidean point to point distance between the manually defined joint locations and the ones determined by the articulated bone registration is shown in Fig. 3.10. The boxplots show the lower quartile, median and upper quartile values. The whiskers extend within 1.5 times the interquartile range. Outliers are indicated with a plus sign.

The mean Euclidean point to surface distance between atlas and subject skeleton surfaces decreases from 2.93 ± 0.63 mm to 0.58 ± 0.04 mm and between the lungs surfaces from 1.76 ± 0.49 mm to 0.42 ± 0.07 mm, including all 26 cases.

3.4.2 Skin registration and organ interpolation

In 4 out of the 15 contrast-enhanced datasets, the automated skeleton initialization was incorrect, and required manual correction. The subsequent hierarchical matching succeeded in all cases given a manually corrected initialization. The mean Euclidean point to surface distances between atlas and subject torso after registration for all 15 datasets are presented in Fig. 3.12. Fig. 3.13 gives an indication of the distribution of the error over the surface. The volumes of the manually segmented and the approximated organs as well as the calculated Dice coefficients are given in Fig. 3.14. Qualitative examples of the skeleton registration and subsequent organ interpolation are shown in Fig. 3.15 and Fig. 3.16.
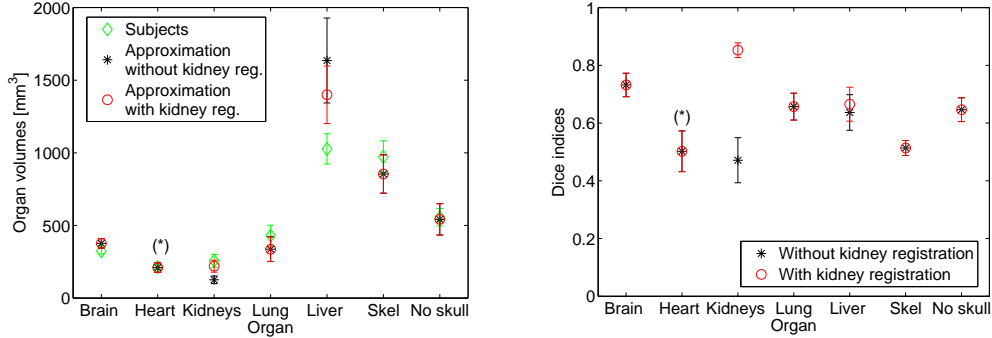
Figure 3.14: Mean value and standard deviation of the organ volumes (left) and the Dice coefficients (right). The Dice coefficient for the skeleton is given with and without including the skull. Additional results are given if the kidneys are registered as well (see 'Discussion'). For the brain, heart, lungs and the skeleton, the results are identical with or without kidney registration. (*) The result is based on a subset of the data (see text).

3.5 Discussion

The experiments demonstrate that the method performs highly robust in the presence of large postural variations, with successful fully automated matching in 37 out of a total of 41 cases. In the remaining 4 cases, only the initial animal pose estimate required manual correction. The achieved accuracies are discussed in the following.

3.5.1 Skeleton and lungs registration

Using articulated registration, a mean surface distance between the atlas and the target skeleton and lungs within two voxel dimensions is accomplished and we show that the method can handle bones with moderate osteolysis. This performance, given the large variety in the data with respect to posture, strain, gender and size of the animals, demonstrates the robustness of the method. The results are comparable to the accuracy reported in [26]. However, our approach is more than an order of magnitude faster.

An important fact to notice is that there exists a clear dependency between the mean surface distance and the joint location distance before the registration: the lower the bone or the joint in the hierarchy, the larger the distance. The dependency does not appear anymore after the registration (Fig. 3.11). This is an indication that possible registration errors made at a high hierarchical level do not propagate down the tree and do not influence the registration result of elements at a lower hierarchical level. For all joints, the joint localization error decreases an order of magnitude as a result of the registration.

Although it appears from Fig. 3.10 that the joints of the front limbs could be determined significantly less accurate than the hind limbs (balanced one-way ANOVA $p < 0.05$). This is caused by the fact that the hind limbs are modeled as rigidly connected to the pelvis, whereas the front limbs are modeled as dependent on the skull registration only (without a rigid connection). As a result, the front limbs are occasionally placed
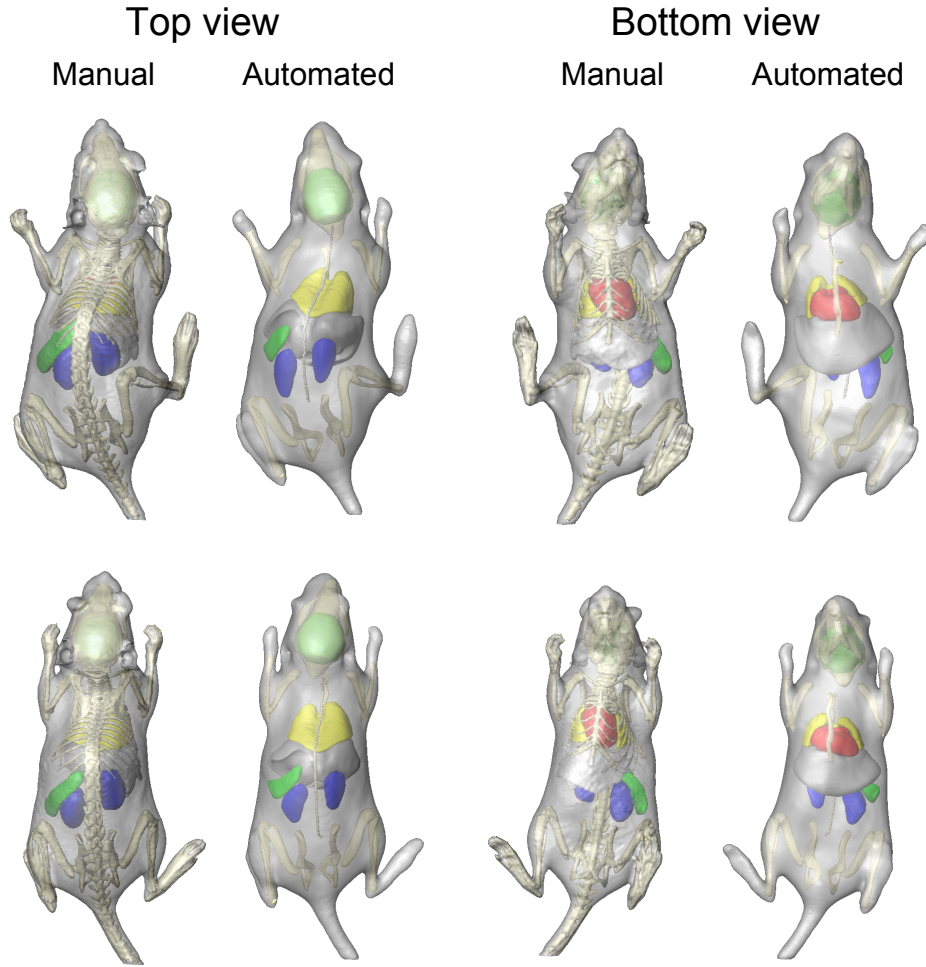
Figure 3.15: Skeleton registration and organ interpolation result for two different mice (top and bottom row). The rows show alternately the manually segmented animal and the mapping result. Only those objects are shown that are used for calculating the Dice coefficients (except of the spleen and the skin).

relatively further away from their target after initialization. In such a situation, the final registration result may be suboptimal. There are no significant differences among the hind limbs and among the front limbs themselves.

Another situation where suboptimal registration results can occur is when two adjacent long bones are pointing in almost the same direction or the opposite direction (meaning that they are almost aligned next to each other). In some of these cases, the resulting scaling factor along the longitudinal bone axis was the maximum value that was considered anatomically realistic for this particular bone (scaling by 15%). As a result, parts of the adjacent bones were erroneously assigned to belong to the target bone during registration. These cases are shown as outliers in Fig. 3.10. A remedy for this problem would be to register adjacent bones simultaneously or to traverse the hierarchical tree several times. The previous registration result could be used for initialization.

3.5.2 Skin registration

As presented in Fig. 3.12, the mean surface distance between the atlas and the subject skin is in the order of one voxel dimension. This indicates that the chosen amount of correspondences, together with the minimum and maximum geodesic distance constraints and the regularization parameter λ result in a proper interpolation of the surface while surface smoothness is retained (Fig. 3.13).

There are some areas on the surface where the surface distance becomes larger (red areas in Fig. 3.13). In these areas there are either not enough skin correspondences available because they are too far away from bone, or the automatically extracted subject surface contains elements that are not included in the model skin (eyes). In applications where a high accuracy particularly in the lower abdomen is needed, the minimum and maximum geodesic distance constraints should be defined for all the correspondences individually instead of using the same values for all of them. This would allow to better deal with the area specific density of the initial sparse landmarks on the skin. Another advantage would be that the amount of candidates around already found correspondences could be drastically reduced in areas with dense initial landmarks. Another way to improve the accuracy of the skin interpolation would be to assume the landmark localization errors on the skin to be non-isotropic i.e. to allow shifting correspondences only tangential to the surface [111] during TPS interpolation.

3.5.3 Organ interpolation

For the soft tissue interpolation step we only considered the animal torso and therefore derived a coarse net of correspondences. To include surface areas that have a large curvature like the limbs as well, determination of corresponding nodes should start at a coarse scale (in terms of intervertex distance) and, depending on the required amount of detail, continue at a smaller scale, e.g. as proposed in Wang *et al.* [108]. This however is only feasible, if the model is detailed enough. Furthermore, the limbs should not touch each other or the torso since the calculated geodesic distances may be wrong in such a case.

The calculated Dice coefficients of volume overlap indicate the feasibility of the presented soft tissue interpolation but in addition show some limitations of the method. Since the interpolation does not distinguish between stiffness properties of different tissue types, all the organs are treated in the same manner. This means that in areas where the shape differs most between the atlas and the subject, typically the abdomen, organs may deform in a way that is anatomically not realistic. An example are the kidneys, which may be squeezed and underestimated up to half of their actual volume after warping (Fig. 3.14). As a result, the Dice coefficient is smaller for the kidneys.

Although the Dice coefficients for the registered objects i.e. the skeleton (and as a result the brain) and the lungs are high as expected, they are limited by the fact that the volumes for both are systematically underestimated. The reason for this is that the preprocessing of the CT data causes all parts of the joints to be represented as bone. Especially in the knee and the ankle joints this leads to an overestimation of the bone volume. As for the lungs volume, its underestimation is the result of a simplified

Coronal (Kidneys)		Coronal (Heart)		Sagittal	
Manual	Automated	Manual	Automated	Manual	Automated
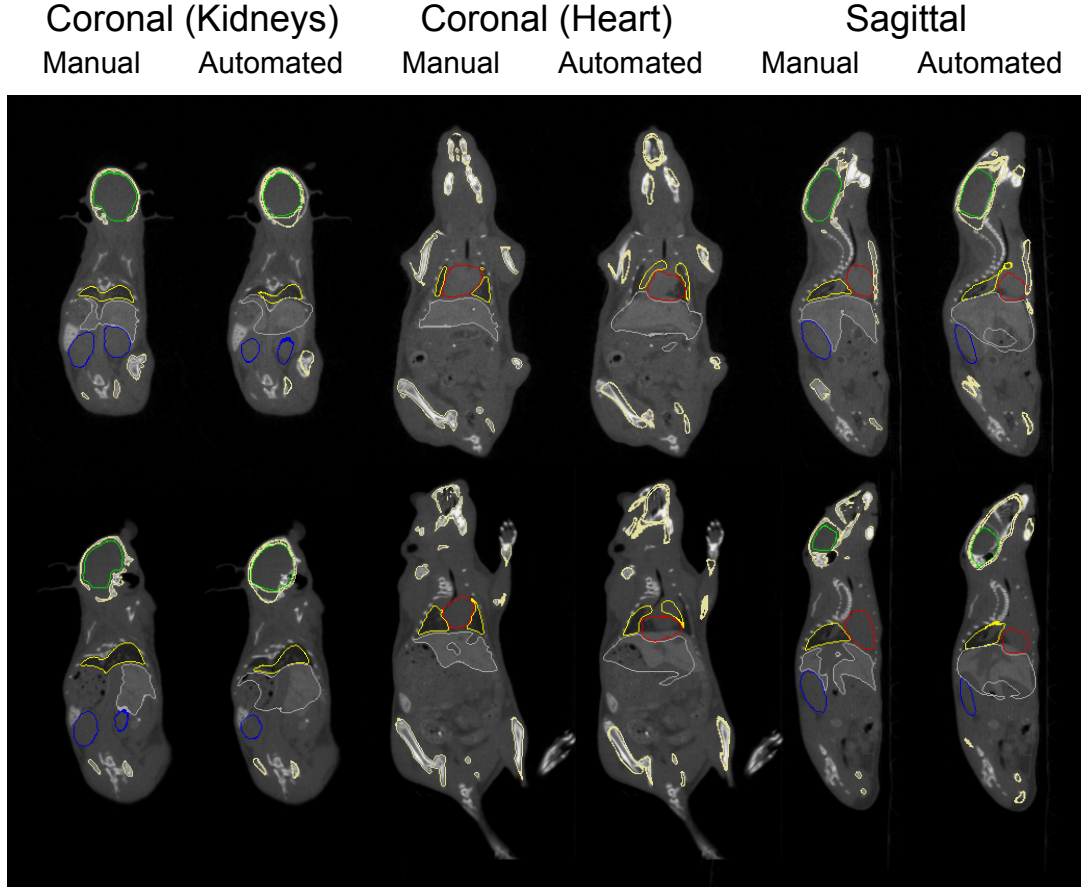
Figure 3.16: Comparison of manual bone and organ contours of two different mice (top and bottom row) in contrast-enhanced MicroCT data. Each row shows alternately the result of the manually drawn contours and the estimated contours for two coronal planes and one sagittal plane. Note that the contrast is only used for delineation of the organs and not for registration.

representation of the lungs in the atlas.

Triggered by the large difference in volume between the subject and atlas liver, we designed an experiment to further investigate on the influence of the shape simplifications in the atlas for this particular organ. Since the liver is adjacent to the lungs and the kidneys we aimed on defining as many correspondences as possible on these two organs before the mapping. The lungs are already registered and therefore a dense landmark set can easily be obtained. As for the kidneys we decided to integrate them into our hierarchical framework (on $L3$). Since we do not expect large shape variations among healthy subjects, allowing 9 DoFs as for the bones suffices to approximate intersubject shape differences. The target kidneys were segmented manually as described in section 3.3.2. The experiment was performed using the 15 contrast-enhanced datasets. The effect on the organ volumes and the Dice coefficients is shown in Fig. 3.14. After registration, the measured kidney volume is almost the same as the target volume and the Dice coefficient has increased. As for the liver, the volume has decreased but is still significantly different from the target (paired t-test $p = 5.5e^{-07}$). From this we conclude that the model

simplifications are the prominent limiting factor of the interpolation result for the liver. Further investigation using an improved animal model has to be conducted to be able to clearly distinguish between segmentation inaccuracies because of model simplifications and physiological intersubject variability.

3.5.4   Segmentation accuracy

The registration of the skeleton was achieved with high accuracy and enables to accurately segment individual bones of the skeleton from the data. For applications that require a higher accuracy e.g. to assess morphological bone changes locally, the amount of DoFs for the articulated registration of the skeleton should be increased i.e. the transformation model should include nonlinear deformations as well. To render the registration robust to large postural variability, the results of our method could serve as an initialization.

Compared to the results for the skeleton and lungs, the segmentation accuracy for the abdominal organs is restricted. However, it is still high enough for anatomical referencing or to provide a heterogeneous tissue model for Bioluminescence Tomography, because even a coarse segmentation can significantly improve the reconstruction result [9, 91]. A possibility for improvement would be to use our result as an initialization of a nonrigid, voxel-based registration method for the entire body. This would require sufficient soft-tissue contrast in the data. However, in many routine MicroCT studies, contrast agents (e.g. eXIA and Fenestra), highlighting abdominal organs, are not part of the experimental protocol.

3.6   Conclusion and Future Work

This paper presents a fully automated method for atlas-based whole-body segmentation in non-contrast-enhanced MicroCT. We proposed a solution that divides the problem into an atlas constrained registration based on high-contrast organs in MicroCT (skeleton, lungs and skin) and a soft tissue approximation step. Experiments demonstrated the method's effectiveness to overcome exceptionally large variations in posture and shape, even in the absence of soft tissue contrast in *in vivo* MicroCT data. By combining an articulated skeleton with a hierarchical anatomical model and a suitable registration framework for individual bone elements (ICP), a final registration result could be obtained very time efficient but yet with high accuracy (between one and two voxel dimensions). We also showed the robustness of the method with respect to moderate bone resorption. In addition, the presented performance of the organ approximation proved that the missing soft tissue contrast in the data can be compensated for and the results of the calculated Dice coefficients outperform previously reported results [20].

To our knowledge, there are no reports to date of other unsupervised methods that can deal with such a high variability in posture and shape and that have been validated as extensively as in this work.

The method is suitable for intrasubject as well as intersubject registration using data acquired *in vivo* and is applicable for referencing of internal processes in molecular imaging research. The absence of any user interaction to initialize the procedure would make

this method suitable for high-throughput batch processing, and posterior result checking and occasional manual initial pose correction. Above that, it could serve as a way to provide a whole-body heterogeneous tissue model for bioluminescence tomography.

The method was tested using whole-body data of mice only but would be applicable to other animals as well, if an atlas is available. Besides that, we want to point out that not only data of entire animals but also data including only parts of an animal can be handled by simply removing the missing body parts from the hierarchical anatomical model. The determination of skin correspondences and the organ mapping can in principle be restricted to a certain volume of interest as well.

In the future we plan to develop multiple small animal models and investigate how to minimize the influence of shape differences between the model and the target, especially in the organ interpolation step. We also plan to generalize the whole-body registration to other modalities as well. The focus will not only be on volumetric data (MRI or SPECT) but also on photographs from the subject surface (mono- or biplanar) for posture estimation, using skeleton based motion constraints.

The modified MOBY atlas is publicly available in the 'Downloads' section at `http://www.lkeb.nl`.

Acknowledgements

Appendix

Calculation of geodesic distances

To determine geodesic distances on the skin surface, the Fast Marching Algorithm [113] is used, a very time efficient method to solve the Eikonal equation $|\nabla T| = F(\mathbf{x})$ using triangulated domains. Given a starting point $\mathbf{x}$, a front with speed F is expanded on the mesh and arrival times T can be determined for all other vertices. By setting a constant propagation speed $F = 1$ all over the mesh, the arrival times are equal to the geodesic distance between the starting point and a given endpoint. The fact that the accuracy of the derived geodesic distances depends on how dense the mesh is sampled requires analyzing the calculation error in practice for the application at hand. For the underlying problem, the target surface is represented with 2000 nodes, which is sufficient to represent the major deformations that are caused by postural variations. Experiments showed that, given a starting point, the mean error for determination of geodesic distances to nodes within a given range g_{max} is below one voxel dimension. Therefore, the chosen sampling is a good tradeoff between calculation time for the geodesic distances
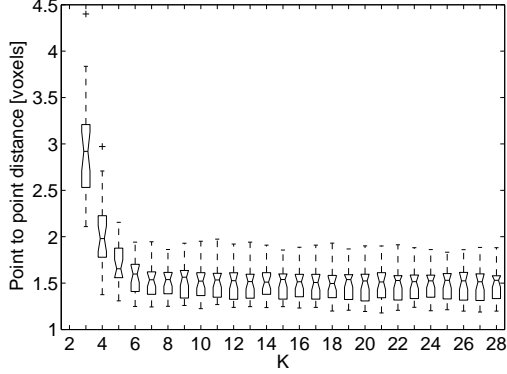
Figure 3.17: Median distance between the subject surface and the mapped atlas surface for 26 subjects, depending on the parameter K (see text). Note that the point to point rather than the point to surface distance is presented here.
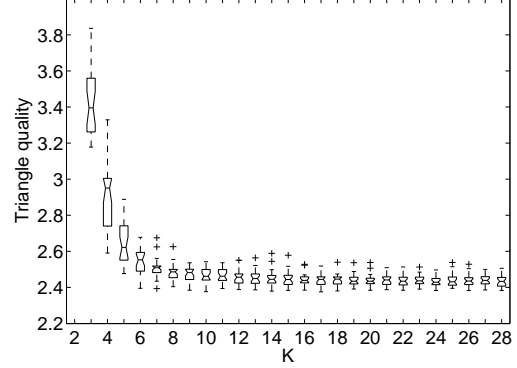
Figure 3.18: Median triangle quality of the mapped surfaces, depending on K. The median quality of the atlas skin triangles before the mapping is 2.28.

and possible correspondence localization accuracy. Note that the geodesic distances have to be calculated for each target but only once for the source (atlas) surface. Therefore the atlas skin surface can be sampled very densely and the distribution of geodesic distances be calculated offline.

Optimum value determination for parameter K

To derive the optimum value for the parameter K we chose $g_{min} = 15$ and $g_{max} = 50$ and varied K within a range of 2 and 28. For this experiment, we used the skins of all animals of the non-contrast-enhanced study (26 animals). Quantification of the performance is based on the median point to point distance between the source (atlas) and the target skin surface, after determining correspondence and mapping the atlas torso to the target surface, a triangle quality measure, applied to the mapped atlas surface and the processing time. The triangle quality is defined as the ratio of the radius of the circumcircle and the radius of the incircle of a triangle (a value of 2 is the optimum). Fig. 3.17, Fig. 3.18 and Fig. 3.19 show the results of the experiment. The boxplots indicate, that $K = 8$ is a reasonable choice and a good tradeoff between accuracy and calculation time, since neither the surface distance nor the triangle quality improve significantly for $K > 8$.

Invertiblity of the Thin Plate Spline transformation

To investigate if the regularization of the energy functional (section 3.2.5) leads to an invertible transformation, given a dense set of skin and skeleton correspondences (section 3.2.4), we calculate the determinant of the Jacobian of the final transformation for all 26 datasets that were used for the skeleton registration validation. The determinant was determined in steps of 180 μm (twice the phantom voxel size) i.e. in a total vol-
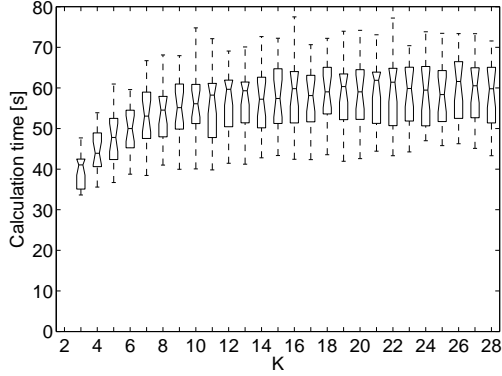
Figure 3.19: The calculation time for determining skin correspondence for 26 subjects, depending on K.
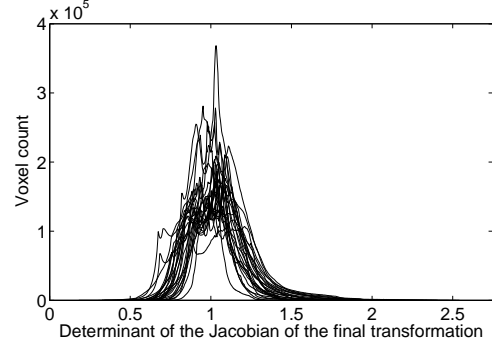
Figure 3.20: Histograms of the determinant of the Jacobian of the final transformations for all 26 datasets used for validating the skeleton registration.

ume of $201 \times 201 \times 601$ voxels and was based only on the non-affine parts of the final TPS transformations. Figure 3.20 shows the results. The first observation is that all values are positive, proving that the transformation is in principle invertible. Second, the vast majority of the determinants lie between 0.5 and 1.5. This means that only moderate expansion and compression takes place (1: neither compression nor expansion, <1: compression, >1: expansion [114]).

Atlas-Based Whole-Body Segmentation of Mice from MicroCT data

4

Articulated Planar Reformation for Change Visualization in Small Animal Imaging

Chapter 4

Abstract

The analysis of multi-timepoint whole-body small animal CT data is greatly complicated by the varying posture of the subject at different timepoints. Due to these variations, correctly relating and comparing corresponding regions of interest is challenging. In addition, occlusion may prevent effective visualization of these regions of interest. To address these problems, we have developed a method that fully automatically maps the data to a standardized layout of subvolumes, based on an articulated atlas registration. We have dubbed this process articulated planar reformation, or APR. A subvolume can be interactively selected for closer inspection and can be compared with the corresponding subvolume at the other timepoints, employing a number of different comparative visualization approaches. We provide an additional tool that highlights possibly interesting areas based on the change of bone density between timepoints. Furthermore we allow visualization of the local registration error, to give an indication of the accuracy of the registration. We have evaluated our approach on a case that exhibits cancer-induced bone resorption.

4.1   Introduction

MOLECULAR IMAGING offers new possibilities in lifescience research, because it allows *in vivo* imaging of biochemical processes at a macroscopic level. This means that the onset of pathological processes can be studied at an early stage, long before large-scale anatomical changes occur [3], and followed over time in the same subject [2]. Nowadays a large range of small animal scanners is available that enable acquisition of data of the entire animal body and thus to assess disease progression globally. This is of high interest for example in oncology research because it enables monitoring metastatic behavior of different types of cancer [5,6].

Typical molecular imaging modalities are Bioluminescence Imaging (BLI) and Fluorescence Imaging (FLI), which enable *in vivo* imaging of gene expression. Both have a very high sensitivity but their spatial resolution is low, which complicates linking the signal to the corresponding anatomy [7]. Therefore, the data is often fused with a modality that provides high anatomical detail, such as microCT. An example is given in [5], where BLI is used to monitor metastatic activity of breast cancer cells in the mouse skeleton over time. The BLI data is combined with microCT, to assess cancer-induced bone resorption. However, since light has a very limited penetration depth in biological tissue, the positioning of the animal in the scanner during the acquisition is critical to achieve maximum optical signal. As a result, it is difficult to standardize the data acquisition protocol and animal positioning can vary to a great extent among different animals at the same time point or the same animal in a follow-up study (Fig. 4.1). Lacking anatomical structure in optical imaging except for contours, the subject is placed in the BLI and the CT scanner in the same holder, in order to minimize posture differences and to facilitate the registration and fusion of BLI and microCT data [7]. Thus, the posture variability issue transfers to microCT as well. Also, in follow-up studies with only microCT, there is no standardized positioning protocol and the animal posture will greatly vary.

In the current workflow, the biologists resolve this postural variability by visually comparing subsequent image sets to find differences with regard to their hypotheses on drug effects and disease progression. In the case of an experiment on cancer-induced bone resorption, this would result in a search for local intensity decreases in the bones. Researchers that aim at comparing the same structures, e.g. a particular bone, face the problem that they have to localize the structure of interest in each dataset separately, which is complicated by the fact that these structures of interest are not aligned due to the large differences in animal posture between time points. To a large extent, the biologists are able to form a mental picture of the entire subject and the relative position of a region of interest, but we aim to standardize this into a fully automatic procedure that facilitates comparison and data interpretation.

In a first step to address the problem of varying animal posture, we earlier presented an approach for fully automated skeleton registration [17]. The method registers the skeleton of an anatomical animal atlas bone by bone to a skeleton derived from whole-body microCT data. Subsequently, it is possible to interpolate low-contrast areas (most major organs), yielding a segmentation into these organs. The resulting registration and segmentation allow to highlight the same structure in several datasets and significantly

Chapter 4
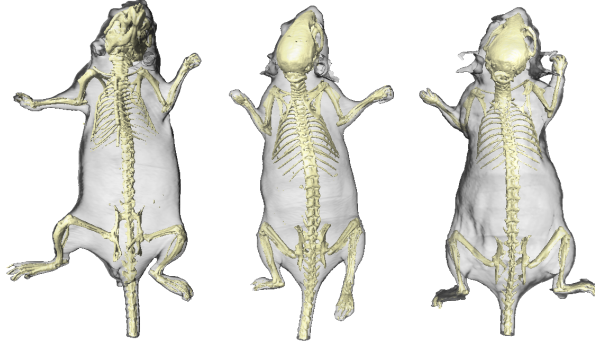
Figure 4.1: Three examples that demonstrate the large variability in animal posture between different scans. The subjects were scanned in supine (left image) and prone (right two images) position. Shown are isosurfaces of the CT data corresponding to the skin and the skeleton.

facilitate data navigation, but still require multiple, unaligned datasets to be analyzed side by side.

Therefore there is a great need for visualization methods that present one or multiple whole-body datasets in an integrated and interactive fashion: This would greatly facilitate the assessment of differences between datasets qualitatively and quantitatively.

In this work, we present several methods to facilitate the comparison of whole-body data from cross-sectional or follow-up studies. Our contributions are threefold:

- We describe a method to fully automatically transform anatomically relevant regions of interest from a whole-body small animal dataset into a standardized layout in order to facilitate comparison despite large differences in animal posture.

- Based on this standardized layout, we present a comprehensive coupled view approach for the visualization of change in whole-body datasets. Our approach is based on a two-level localization strategy that enables researchers to quickly identify areas of interest in a global whole-body view, and then to zoom in on and study the changes in a linked local per-segment view. This process is enhanced with the integration of derived features that further highlight areas of change.

- Finally, we investigate the role and utility of our application in molecular imaging research by means of a case study with two experienced domain scientists.

In this paper we focus on the analysis of microCT data because our whole-body segmentation method is based on this type of data. However, the presented methods can be used for other modalities as well, given an atlas and a registration of it to the skeletal structure of the animal.

In the next section, we discuss related work and in Section 4.3 we describe our approach in detail. Section 4.4 addresses implementation details and in Section 4.5 we look at the performance and evaluate our work. Finally, we present conclusions and future work in Section 4.6.

4.2 Related work

Visualization of three dimensional data often suffers from effects such as occlusion and the lack of depth cues. In order to gain a better understanding of three dimensional data in this respect, it is useful to map it to a standardized frame or onto a 2D plane. This becomes even more relevant when different three-dimensional datasets are to be visually compared.

Mapping to a standardized frame can be done for elongated structures such as vessels or the colon. Methods to achieve this are often based on curved planar reformation (CPR), which can be used to map tubular structures onto a plane. Kanitsar *et al.* [115] describe three methods to generate CPR images: projection, stretching and straightening. An application based on CPR is presented by Ochi *et al.* [116], who describe how CPR can be useful for the evaluation of aneurysms in CT angiography data. Lee *et al.* [117] present an approach that results in a topological and orientation invariant visualization of vascular trees. Finally, Ropinski *et al.* [118] describe a method to create a standardized visualization of mouse aorta PET and CT scans by applying CPR. Several visualizations are applied to enable comparisons between data.

Similar approaches are available to visualize the colon, which can be virtually unfolded or flattened to a 2D representation. Two of these methods are described by Hong *et al.* [119] and Lee *et al.* [120]. The resulting visualization enables showing the entire inner colon surface in a single view. An approach that combines CPR with volume rendering of the colon is described by Williams *et al.* [121].

The visualization of three-dimensional objects with a complex structure is facilitated by decomposition of the structure into distinct elements. This decomposition enables the application of exploded views, which is a commonly applied technique for depiction in technical drawings. It can clarify a visualization because it shows elements that would otherwise be hidden behind others. In Li *et al.* [26], an interactive exploded view is described that can be automatically generated from a complex solid model. Sonnet *et al.* [122] present a technique that uses a probe to interactively explode a 3D model.

Exploded views can also be used for the direct visualization of volume data. An approach for this is described by Bruckner *et al.* [123], where user-indicated parts of volumetric data are arranged based on a force model. A different technique is presented by McGuffin *et al.* [124], who describe a number of volume deformation methods that for example spread apart or peel away the volume.

Our approach extends these ideas by integrating a priori knowledge of the subject under study, in this case the endo-skeleton and the known modes of articulation that it affords. By making use of the skeleton as a model for articulation, we are able to create a standardized visualization that facilitates navigation in complete whole-body datasets and enables effective comparative visualization between different timepoints or between different subjects.

There are certainly parallels between our work and the volume animation method of Gagvani *et al.* [125], where a derived skeleton is employed to enable the realistic animation of volume datasets such as the Visible Human. However, where the APR is completely automatic, their skeleton is derived from volume data by a thinning process, and joints

are manually assigned by an animator. In addition, they make use of a number of sample points to transform spherical parts of the volume into new poses of the skeleton. Finally, the purpose of their method is the lifelike animation of volumes, whereas we focus on the standardized analysis of anatomically relevant subvolumes of whole-body datasets.

In this work, we focus on the role of articulated planar reformation in facilitating the visualization of change in small animal datasets. Within this context, we have also implemented a number of existing comparative visualization techniques [126, 127]: Side-by-side views or small multiples, animation, red-green channel overlays and image checkerboarding. In addition, we present the integration of a domain-specific change metric, in our case bone change, that can be mapped onto the atlas geometry and acts to facilitate the rapid localization of interesting changes both in the whole dataset and also in separate elements that are being focused on. This is an extension of previous comparative visualization approaches where differences were explicitly represented by geometry [128] or where multiple volumes could be combined to form new features for comparison [129].

4.3   Method

The complete pipeline is illustrated in Fig. 4.2. We start by briefly summarizing the steps, after which the details are further explored in the following subsections.

A standard atlas is automatically registered to all of the CT datasets that are to be compared, either of multiple small animals or of multiple timepoints of the same animal, using the method of Baiker *et al.* [17]. The atlas is based on that published by Segars *et al.* [59], but has been further manually segmented into its constituent bones. For each segment of the atlas, we derive a linear transform using the articulated registration approach in Section 4.3.1 (Fig. 4.2b).

Then, for each bone in the atlas, an object-aligned bounding box is automatically determined based on the surface representation of the bone in the atlas and the corresponding linear transform that was determined during registration. Using the bounding box and the resampling transform, the volume data is resampled for each bone with the aim of obtaining the volume in a standard coordinate frame, which facilitates comparison (Fig. 4.2c). This is described in Section 4.3.2.

Per CT dataset, the collection of resampled data volumes can be visualized in a standardized layout to give a global overview of the data (Fig. 4.2d). This is explained in detail in Section 4.3.3. Importantly, having multiple datasets in the same reference frame, in this case the atlas, allows element-wise visual inspection (Fig. 4.2e). See Section 4.3.4.

Furthermore, features can be visualized that pinpoint interesting areas in the global view. This further facilitates data exploration. One such feature is the bone density change metric, which is discussed in Section 4.3.5. Aside from this, we enable visualization of the registration error, giving the user an impression of the registration accuracy. See Section 4.3.6.

The resulting user interface consists of the standardized layout, henceforth referred to as the APR view, at the top, with a number of focus views of the multi-timepoint data side-by-side at the bottom. By clicking on any segment of the APR view at the top, the focus views at the bottom switch to that subvolume. The APR views and
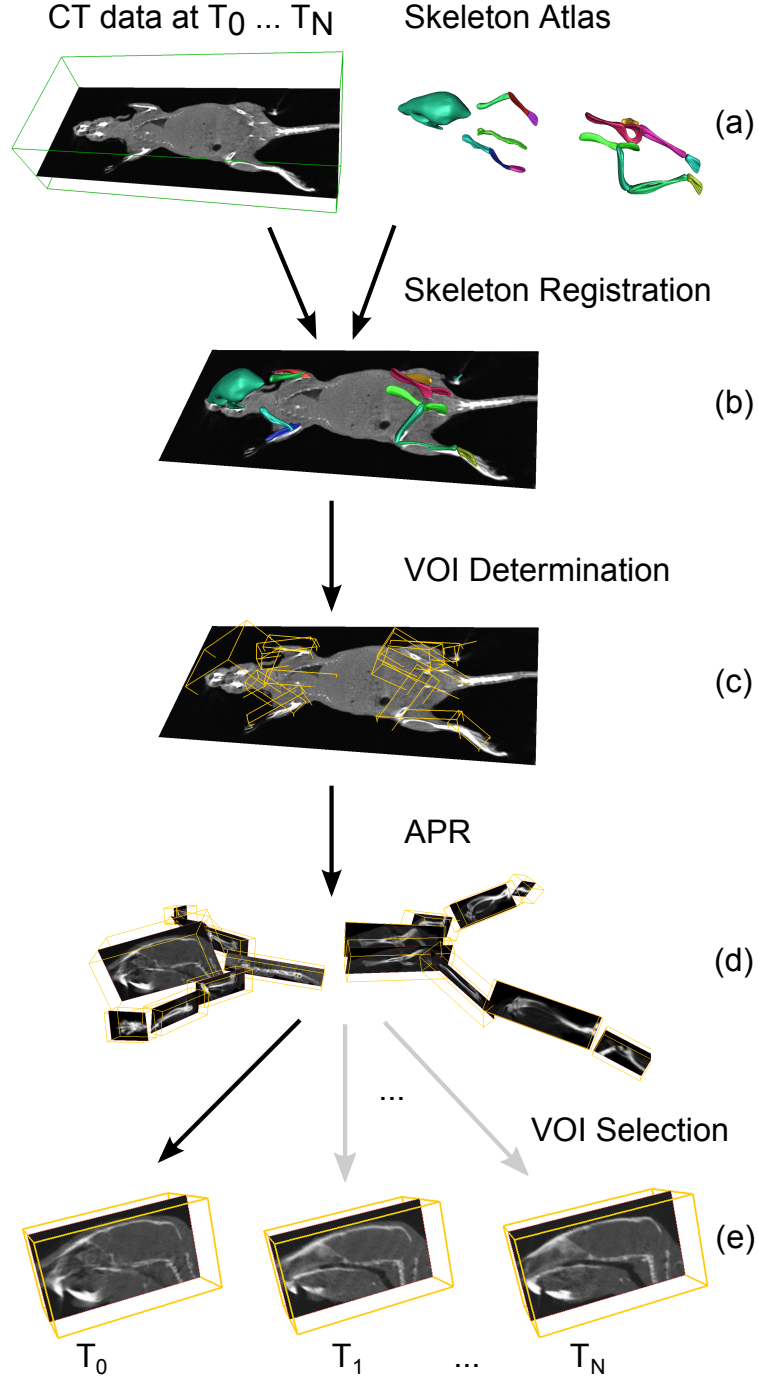
Figure 4.2: An overview of our method. For each timepoint, the input data is the CT data and the surface representation of the atlas (a). The atlas is registered to the CT data using articulated skeleton registration (b). Based on bounding boxes of the atlas segments, we determine the volumes of interest (VOI) from which the data will be sampled (c). Then we perform the articulated planar reformation and visualize the resulting VOIs in a standardized layout (d). After this, any of the segments can be interactively selected for closer inspection. This procedure is performed similarly for the other timepoints, which enables comparison (e).
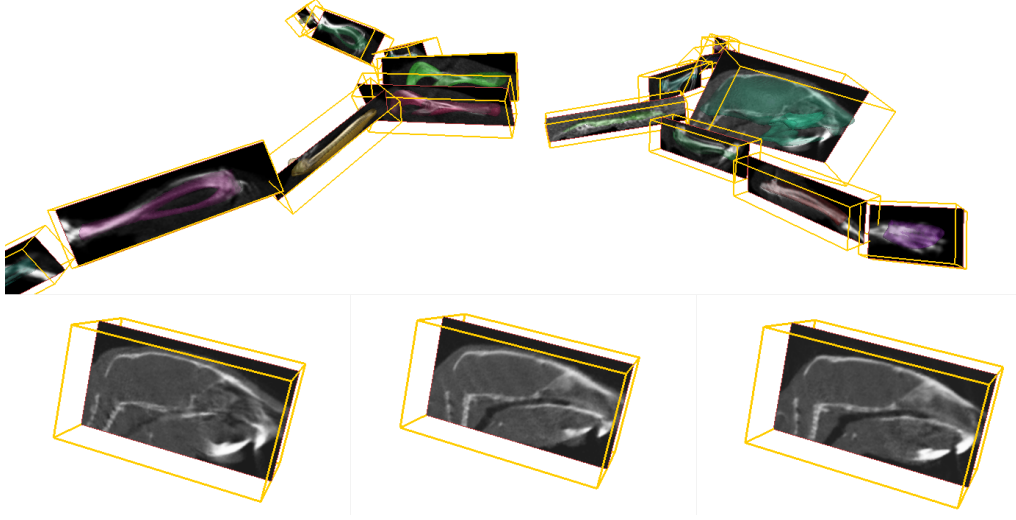
Figure 4.3: An articulated planar reformatted visualization of a mouse, where the skull has been selected and is shown at three different timepoints in the focus views. The visualization shows a slice of the volume with a corresponding bounding box. Additionally, the global overview shows a semitransparent surface rendering of the atlas surfaces.

focus views can be configured for any combination of visual representations, for example surfaces with mapped derived features, subvolume slices, and so forth. Fig. 4.3 shows an example where all views have been configured to show volume slices, whereas Fig. 4.5 shows surfaces with mapped features.

4.3.1 Whole-body registration

In order to register a common atlas to all whole-body datasets under investigation, we employ the automated approach described in [17]. For completeness, we briefly explain the method in this subsection. It is based on the publicly available MOBY whole-body atlas of a mouse [59], which we modified by segmenting the skeleton into individual bones, identifying joints and by adding anatomically realistic joint rotation models [17]. Using this modified atlas, we first register the elements that show high-contrast in non-contrast-enhanced microCT, namely the skeleton, the lungs and the skin. To deal with possibly large articulations between bones, we perform the registration based on a hierarchical anatomical model of the animal. After a coarse alignment of the entire skeleton, the individual bones are registered step by step, starting at the skull, proceeding with the spine and then moving down the front and hind limbs separately. The used transformation models for the individual bones are dependent on the joint type. Therefore, the number of degrees of freedom (DOFs) varies between seven for a hinge joint (translation, non-isotropic scaling, one rotation) and nine for a ball joint. The lungs and the skin are registered subsequently, based on the skeleton registration result. Finally, we derive a set of correspondences from the registered elements to define a Thin-Plate-Spline (TPS) interpolation of major organs. An example of a segmented animal is given in Fig. 4.4. For the work described in this paper, we made use of the skeleton only.
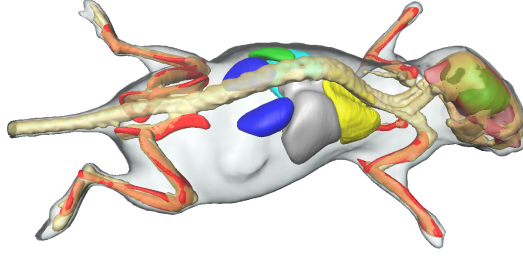
Figure 4.4: An example of a segmented mouse body. Shown are the original skeleton (beige), the atlas skeleton (red), major organs and the skin.

The algorithm is fully automatic and only needs the microCT dataset as input. The restricted number of DOFs for the individual bones renders the method highly robust to large postural variations but also to moderate pathological bone malformations (e.g. bone resorption as a result of metastatic activity).

4.3.2 Articulated Planar Reformation

In order to obtain the data for each atlas segment in a standard coordinate frame, we perform Articulated Planar Reformation (APR). A bounding box to resample from is acquired for each segment by performing principal component analysis (PCA) on the surface representation of the bone. This results in three principal components. The direction of the principal components are used to determine the edges of the bounding box and the magnitude of the components maps to the size. By using the direction of the principal components, the volumes of interest are automatically aligned with the bones. An additional margin can be added to the bounding box, partly for aesthetic purposes, but this also ensures that the entire bone falls inside the bounding box. The margin is a parameter that can be changed by the user. The resulting bounding boxes are shown in Fig. 4.2c.

Using the bounding box and the registration transform, a new data volume can be created for each bone, the size of which is equal to the bounding box. Using the registration transform and the necessary correction for the direction from the PCA, a cubic resampling is applied to the original CT data to obtain the new volume. The result is a series of small image volumes that each contains the resampled image data of the bone aligned with the principal components of the corresponding atlas bone.

4.3.3 Articulated Planar Reformation View

For each resulting image volume, we can now apply various existing visualization techniques to visualize its contents. The appropriate visualization method entirely depends on the kind of data and the user's requirements. We provide a range of commonly used techniques, such as image planes that can be moved through the volume interactively, isosurfaces and volume renderings. The image planes, such as those shown in Fig. 4.2, 4.3, 4.5 and 4.6 are positioned in three dimensional space in order to provide the

user with a cue concerning their local context, which is anatomically relevant. Parameters for all the visualizations, such as brightness and contrast, color maps and isovalues can be interactively adjusted.

Considering the entire collection of image volumes, we can apply an articulated planar reformation view (APR-view), which puts all the image volumes in the scene together in any desired layout. To prevent the image volumes from occluding others, we have designed a planar arrangement so that subvolumes can be separated from each other using an "exploded view" layout (Fig. 4.2d). This makes all the elements separately visible at the same time. The layout in the figure has been created beforehand by manually positioning the atlas segments in space and saving it to a configuration file, combined with the atlas itself. The standardized layout was carefully designed, keeping in mind planarity, anatomical consistency and occlusion reduction. The layout is automatically applied to all datasets. For a different layout or a new atlas, a new configuration file will be required. Alternatively, the user has the option of generating the layout automatically, which moves all segments to the same plane (flattens) and then outward in that plane with respect to the center (explodes).

4.3.4   Focus view

An articulated layout of all image volumes may be useful for some purposes, but one of the strengths of our approach lies in being able to visualize each element of the atlas separately in its own reference frame. The user can interactively select a part of the atlas from the APR-view by clicking on it. This element is then shown in a separate focus view, which allows closer inspection of the data without any of the other elements being in the scene. To facilitate orientation, the current camera position and direction is visualized in the global APR-view by way of a cone. This is illustrated in Fig. 4.5a. The selected bone, in this case the femur, has been selected and is shown in the focus views (Fig. 4.5b and c).

A further advantage of the alignment between the segment and the axes of the reference frame is that the segment is now in an anatomically relevant orientation, which facilitates visualization using image planes by slicing through the volume in the direction of the principal components.

In the following subsections, we discuss the features that we implemented to enable comparison of corresponding bones in different datasets. These techniques could be applied for intertimepoint comparisons as well as intersubject or other types of comparisons.

As shown in [17], the automatic atlas registration is accurate enough for many comparative purposes. However, a further rigid per-segment registration can improve registration results and facilitate finer comparison, such as some of the methods described below. Therefore, we have integrated an optional additional registration, the results of which were used to create the visualizations in Fig. 4.6. This additional registration step applies an adaptive stochastic gradient descent method using voxel-based normalized correlation. This method is described in [130]. It is an optional step, which we applied manually in order to optimally demonstrate the comparitive visualization methods. We are currently in the process of integrating this method into the pipeline.

Figure 4.5: A global articulated planar reformatted visualization of the atlas with the bone change metric between the first two timepoints color coded onto the surface (a). The bone change metric highlights potentially interesting areas that the user may want to further inspect. The femur has been selected and is shown side-by-side in the focus views for the three available timepoints at 3, 5 and 6 weeks into the experiment (b) and (c). Shown for each timepoint are an image plane that can be interactively moved through the volume (b) and an isosurface (c). At 5 and 6 weeks, bone resorption can clearly be seen near the knee area (indicated by the arrows), even though the animal posture in the original data was highly variable. Note that between the first and second timepoint, with the subject at 10 and 12 weeks of age respectively, some growth is still taking place, which has to be taken into account when analyzing the images. More details about the data are presented in Section 4.5.
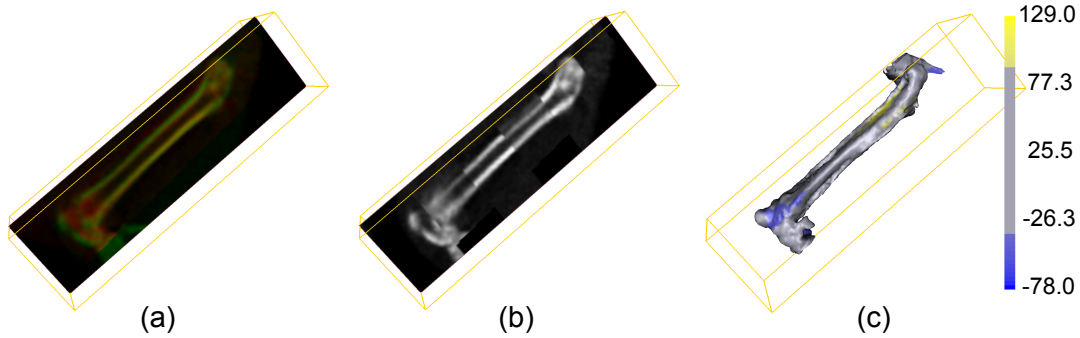
Figure 4.6: Using the same data as in Fig. 4.5, different modes of comparative visualization are applied to the first two timepoints. We have performed an additional rigid registration in order to maximally illustrate the capabilities of these techniques. A red-green overlay is shown in (a). In (b), a checkerboard visualization is shown that can be used to assess the quality of the registration. In (c), the bone change metric has been applied and mapped to the surface representation of the atlas.

Side-by-side visualization

The first technique is a side-by-side comparison and involves showing the data from different timepoints in separate viewer frames. The cameras of these viewer frames can be synchronized, as well as any image planes that are used to slice through the volumes. This way, the user has exactly the same view for the different timepoints. This is demonstrated in Fig. 4.5. There are several advantages to this approach. First, side-by-side visualization closely resembles the traditional way in which biologists compare datasets. Second, even when there is a relatively large registration error, the human visual system can correct for this discrepancy and link corresponding regions of interest. Finally, this approach allows for all kinds of visualization, including slicing image planes, isosurfaces and volume renderings, without the rest of the mouse body obstructing the view.

Comparing by switching

In this approach, the visualizations of all timepoints are shown in the same viewer frame and a slider can be used to quickly switch between the datasets. Assuming the registration between the timepoints is satisfactory, this approach allows the user to spot minute changes by flipping back and forth between timepoints. As in the side-by-side approach, this visualization allows all available types of visualization.

Overlays

In this approach, the visualizations of all timepoints are shown in the same viewer frame and a slider can be used to quickly switch between the datasets. Assuming the registration between the timepoints is satisfactory, this approach allows the user to spot minute changes by flipping back and forth between timepoints. As in the side-by-side approach, this visualization allows all available types of visualization.

Checkerboard

A final option is to use a checkerboard combination of two timepoints (Fig. 4.6b), which is useful for assessing whether two datasets are properly aligned. When this is not the case, this will be clear by the appearance of jagged edges in the visualization.

4.3.5   Feature visualization

Our approach is well suited for integration with feature visualization. For the case of research into cancer-induced bone resorption, which we will elaborate on in the evaluation (Sec. 4.5), we provide a bone density change metric. This tool can be used to estimate the change in bone density, which is directly related to the intensity values in the CT data. The bone density change is mapped onto the atlas surfaces and can be visualized using a color map as is shown in Fig. 4.6c.

The metric is calculated using one of two variations of the same method: With *simple bone change*, values are first interpolated at all vertices of the atlas mesh, from both of the atlas-registered volume datasets that are to be compared. At each vertex position, the value interpolated from the second dataset, referred to as the followup, is subtracted from that of the first dataset, referred to as the baseline. The end result is a new dataset, defined over all vertices of the atlas, where each value describes the signed change in density. If the value is negative, bone density has decreased, and vice versa. With *locally aggregated bone change*, we additionally sample values at a configurable distance, measured along the surface normal, both on the outside and the inside of each vertex. For each vertex, the average of the three samples (inside, outside and at the vertex itself) from the followup dataset is subtracted from the average of the three samples from the baseline dataset. This variation is more robust but less sensitive than the simple bone change.

The integration of this metric into both the global APR view and the focus views enables a two-level change localization approach. When we apply the visualization of this metric in the global overview, such as in Fig. 4.5a, the user can directly spot potentially interesting regions. The corresponding sub volume can be selected and brought into focus for a closer inspection of the bone change metric. This process assists the user in rapidly pinpointing specific regions where high bone change indicates that further analysis could be fruitful.

To further facilitate the visual pinpointing of interesting regions, we have implemented an interactively configurable significance threshold for all colormaps. With this functionality, the user determines above which threshold a feature is considered interesting. An example is shown in Fig. 4.5a, where areas below the significance threshold are colored gray, and regions outside are assigned a color, usually from a perceptually linearized colormap. The surface rendering is interactively updated during changes to the significance threshold, further helping to understand the mapped feature.

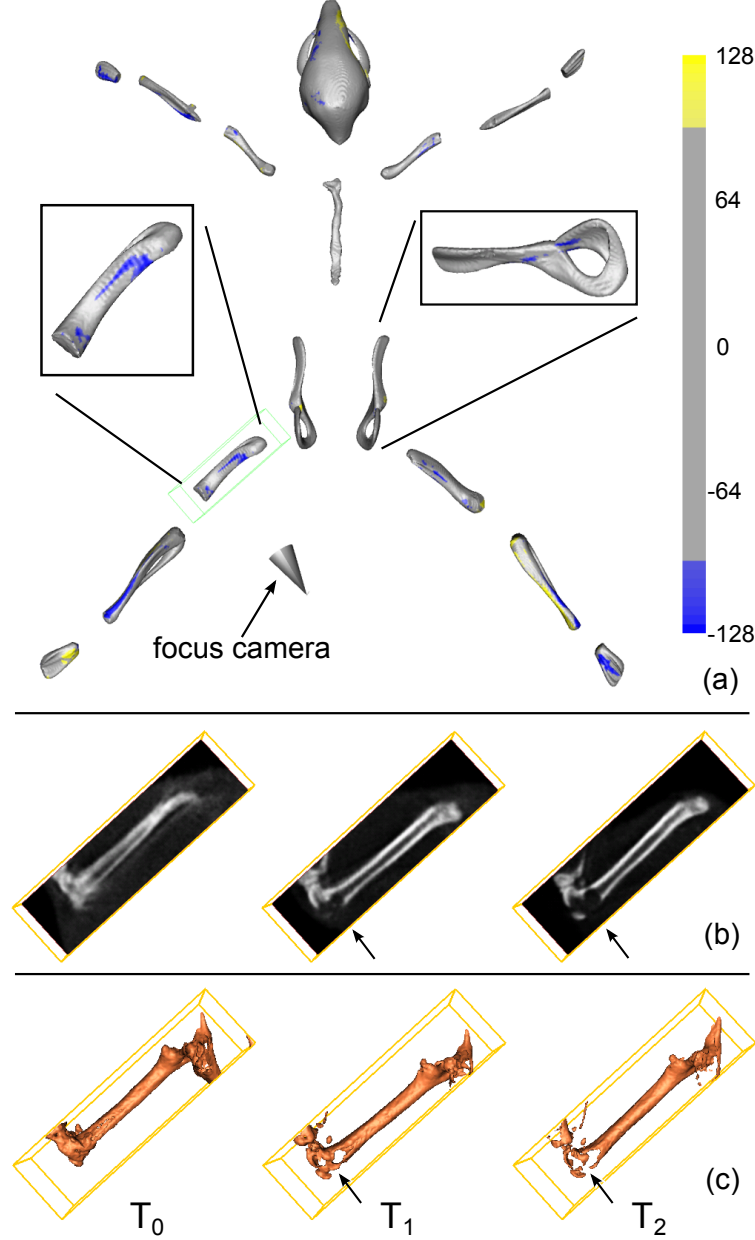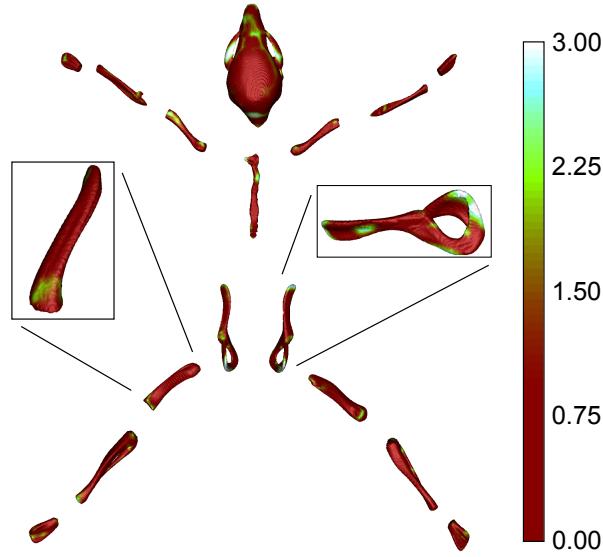*Figure 4.7: A global articulated planar reformatted visualization of the atlas with the registration error at the first timepoint color coded on the atlas surface. The registration error is the distance (in voxels) to the CT surface that was used in the registration (Sec. 4.3.6). We use a color map that is perceptually linear [131].*

4.3.6 Confidence visualization

Residual error in the atlas registration process has an effect on the accuracy of the analysis. In order to give the user feedback on the localized registration error and hence help them to judge the results, we provide the option to color code the surface according to the registration error at each point. This is the distance between the surface representation of the atlas element and the CT surface that was generated and used in the registration process. Fig. 4.7 illustrates this idea.

Importantly, the registration error is also high in areas of high bone resorption, exactly the phenomenon under study in this case, an observation that should be used in the interpretation of both error and bone change. In areas of real bone change, we expect the confidence visualization to show focused low confidence surrounded by high confidence. When the error visualization shows a pattern that deviates from this, the bone change visualization should be verified by studying the direct comparative visualizations.

4.4 Implementation

We implemented our approach as an extension of the Cyttron Visualization Platform (CVP), which has been developed by us as a part of the Cyttron project [132]. The CVP is a software package for visualization of multimodal data and provides a number of tools for this purpose. It is mainly aimed to be used by biologists to visualize and explore their data. The CVP is written in Python and uses the Visualization Toolkit (VTK) for visualization, which in turn is based on OpenGL. Essentially, the CVP provides a

framework and a graphical user interface around visualization methods that are available in the VTK libraries.

We implemented the APR functionality as an extension package to the CVP. The articulated registration functionality was written in Matlab, the reformation and visualization functionality as plugins written in Python, using VTK libraries. We plan to release the APR-package as open-source at a later stage.

4.5 Evaluation

First, we will present some details about the performance of our implementation, after which the user evaluation will follow.

The articulated registration of the atlas to the CT data is a process that is only required once for each dataset. It takes a few minutes on a recent Intel Core2 PC and could be further optimized if required. The articulated planar reformation itself takes a second or two. When the entire pipeline is regarded, excluding the registration, but including loading the data, applying APR and setting up the preconfigured visualization, we are looking at about 10 to 20 seconds. After that, the visualizations can be inspected interactively. Due to memory constraints on the 32-bit machines that are in common use by the domain scientists, we applied cubic subsampling to reduce the size of the datasets from an original resolution af about 512x512x1200 voxels to about 256x256x600 voxels. On 64-bit PCs, to which our users will be gradually upgrading, this step would not be necessary.

In order to investigate the possible role of our application in the research pipeline of molecular imaging domain scientists, we performed a case study evaluation according to the guidelines set out by Yin [133]. We opted for this evaluation methodology, as the contributions of our work mainly target the outer levels of the nested model proposed by Munzner [134], and as we desired to study the real-world application of our pipeline. The main study question was defined as "How can the APR change visualization tool assist domain scientists in studying changes over time, pathology-related and otherwise, in small animal whole-body CT?" whereas the *case* was defined as the "guided application of the APR change visualization tool by two domain scientists referred to as CL, a widely published expert in molecular imaging and oncology research, and MH, a leading small animal and molecular imaging expert, to datasets of cancer metastasis induced bone resorption". The application was guided, as at this stage our assistance was still required in operating the software. CL is also the sixth author of this paper. He contributed to this work with an extensive analysis of the problem domain and by giving feedback on our prototypes, but did not work on the implementation itself. In this context, his role as test user and case study subject was not compromised. MH was not involved in any stage of the project before taking part in the case study evaluation described in this section.

Together with each of the domain scientists, in two separate sessions, we used the software to analyze a dataset consisting of three small animal CT scans, made at 3, 5 and 6 weeks into the experiment. Breast cancer cells had been introduced when the subject was 7 weeks old (week 0 of the experiment). The purpose of the analysis was to study the metastasis of these cells into bony tissue. As per usual for case studies, we

defined a number of propositions beforehand in order to better answer the main study question. During the analysis session, we gathered feedback on the application of the tool, structured according to the study propositions. In the following text, each proposition is stated, together with its related feedback, after which we discuss general comments and our preliminary conclusions.

The standardized APR view speeds up navigation in a dataset, i.e. selecting anatomical elements of interest. CL confirmed that this functionality was important in being able to select anatomical structures of interest, further adding that analysis is often based on *a priori* expectations of the pathology under study. For example, breast cancer is known to metastasize mostly to the long bones, favoring subregions of high bone turnover. MH agreed with the proposition, adding that he found the camera icon (section 4.3.4) intuitive in relating the focus view to the global view.

Automatic anatomical alignment of the subvolumes facilitates comparison of the data. CL confirmed this statement. Confirming the feedback of MH on the previous proposition, he found the camera orientation glyph useful in understanding the relation of a focus view to the global view. The user further indicated that aligning slices with the long bones, as is automatically done in our approach, was definitely preferred. MH commented that this type of alignment was in his view the most natural, further explaining that he would have requested it had it not been available. He added that he liked the way that every subvolume could be treated independently from the global slicing direction.

The switched view is the preferred view for qualitatively investigating bone change. Domain scientists usually eyeball datasets side-by-side in order to compare them. CL commented that with the switched view the registration error was more visible. He further remarked that being able to slice through the data was important in helping to distinguish between real bone change and registration errors. MH also noticed that there were remaining registration errors. He commented that switching was helpful to study geometric alterations, even in cases where registration can't be successfully performed due to gross changes, for example due to global growth or curvature.

The checkerboard view is primarily useful for further verifying the quality of the registration / matching. The utility of this view was not directly apparent to CL. It was finally remarked that it would be useful mainly for checking the quality of the alignment. MH was also not familiar with this representation and remarked that he preferred the switched view, also as they were used to paging through MR image stacks. He concluded by stating that it was an interesting / different approach, but would require training.

The overlay view is primarily useful for detecting minute changes between timepoints (when registration is accurate). Again the growth-related misalignment between the first two timesteps dominated. CL suggested that manual alignment functionality, with this view as feedback, would be very useful. In cases where the registration was better, for example between the second and third timepoints, he considered this view equally important to the switched and side-by-side views. MH was familiar with this representation, commenting that it was an ideal way to study edge differences and mentioning that the red-green mixing helped in interpreting differences. MH's lab already uses this type of representation to look for minute changes and to check the quality of registration.

The coordinated side-by-side view is the preferred view for qualitatively investigating

bone change. CL sees it as advantageous that this view extends and improves on the traditional method of manually comparing two datasets side-by-side. CL confirmed that it was possible to compensate for misregistration, as an internal 3D representation was mentally constructed and used to simultaneously judge change and registration error. MH explained that side-by-side comparisons were done routinely in his lab as part of a first screening of image data, albeit with side-by-side print-outs as they did not yet have suitable software tools for this. With side-by-side comparisons they are able to detect points of interest that should be further investigated. He commented that the 3D interaction possibilities made this representation more user-friendly, concluding that this would probably be the visualization that he would start with, followed by the overlay representation to further study suspected differences.

Global bone change metric facilitates localization of interesting areas in terms of bone resorption. and *The local bone change metric helps to further refine the location of areas of high bone resorption.* During the analysis sessions, the bone change metric visualization was affected by registration issues, but worked well enough to illustrate its use to the scientists. CL stated that in areas where bone cancer metastatic bone resorption occurs, there is a tell-tale pattern of bone density decrease surrounded by bone density increase. Other types of cancer have different tell-tale patterns. He continued that this visual feedback would be ideal for the fast location of interesting areas in the global view as well as further examination in the focus view. MH recognized that this served as an overview of all changes in the whole dataset and stated that, in his opinion, first screening the whole body for changes and then focusing on each of the changes for more in-depth study was indeed the most suitable approach. He agreed that the local bone change metric helped to further refine change locations.

The registration error visualization helps in the interpretation of the bone change feature as well as the comparison views (side-by-side, switching, overlay, checkerboard). CL considered this to be an important tool. He did make the suggestion that we should use distinctive color maps to differentiate between different types of metrics, especially registration error and change features. He further explained that he would check the data more carefully if the registration error is high. Interestingly, MH did not see a use for the registration error visualization in better judging change, stating that the domain expert was capable of differentiating between registration error and real change by local examination and that the error metric was in his opinion too implicit. He did see potential in using the error visualization as a way to study deviation from a standard atlas and hence to phenotyping individual small animals.

The tool will help guide the quantitative study of metastasis-related bone resorption, in that interesting areas can be localized and qualitatively studied before further analysis. CL agreed with this proposition and added that this correlated with the initial goals that were set for the analysis software. He further underlined that the software was to play a role at the start of the analysis pipeline, where domain scientists are exploratively analyzing acquired data to generate hypotheses for further analysis using traditional methods. MH strongly supported this proposition and explicitly underlined the potential value of the tool. He further commented that he believed that the tool could in some cases even answer research questions directly, i.e. without a further traditional analysis step.

4.5.1 Study conclusions

CL was generally impressed with the system, and enthusiastic about its application to future studies by his research group. Other applications of the current functionality were mentioned, including the study of general growth-related deviations. He indicated that future functionality for group studies as well as for side-by-side comparisons of multi-timepoint datasets would be useful. MH was in general positive also, and saw potential for the APR approach also in the study of soft tissue changes in MR. MH independently suggested the future possibilities of projecting groups of datasets onto the standardized layout in order to study group statistics in the same space.

Further, we can derive a number of lessons from this case study. Importantly, it was confirmed that mimicing the existing analysis approach as far as possible with a new visualization application is a good strategy. It facilitates acceptance by the users, and also allows them to leverage their existing experience in applying the new tool. The case study was performed with the blue-yellow colormap for both the bone change and error. Since then, we implemented the suggestion to use intuitively differentiable colormaps for different types of quantities, as can be seen in Figs. 4.5a and 4.7, where respectively bone change and error are represented. Change metrics should be made more robust to residual registration error. The optional additional rigid registration, mentioned in section 4.3.4, is an important step in this direction. Finally, the suggestion to implement manual alignment with real-time comparative feedback will be added in a future version of the software.

Based on the case study, we answer the main study question with the observation that the tool can assist domain scientists in studying pathology-related changes over time by enabling the rapid localization and qualitative study of interesting areas, particularly by the combination of global view for navigation and focus view for more low-level investigation. More globally speaking, it has an important role in the early explorative stages of the analysis pipeline.

4.5.2 Limitations

During this evaluation, we focused on comparing multi-timepoint data of one mouse. However, our implementation also allows intersubject comparisons, which is required when comparing the subject to a control mouse. Judging differences will become more challenging, as apart from the pathological differences that we want to highlight, the two subjects will also have a different anatomical structure. Still, our technique constitutes an improvement over the existing approach of comparing regions of interest in a non-articulated and hence unstandardized manner.

In spite of the possible positive bias, it has been advantageous involving one of our collaborators in the case study, as it made possible far more extensive and in-depth discussion of the results and possible future directions. We did of course take reasonable precautions, for example not involving the user in the actual implementation and also explicitly requesting objectivity during the evaluation. Importantly, we involved an unbiased external domain expert at a later stage who, except for the role of the registration error visualization, confirmed the findings of our primary user.

Furthermore, due to the direct involvement of the collaborating research group, the tool will now find more widespread and longer term use. This will allow us to enter a new phase of evaluation during which we will be able to collect longer term feedback from a larger group of users.

4.6 Conclusion and Future Work

We have presented a method to fully automatically perform standardized articulated planar reformation for a whole-body CT dataset based on an atlas, in order to overcome the limitations caused by varying animal posture and occlusion effects that occur in traditional visualization approaches.

In an articulated registration step, linear transforms are acquired that map each atlas segment of the skeletal structure onto the CT data. Based on these transforms and a principal component analysis of the atlas surfaces, we set up a bounding box in the original CT data where we resample our data from. We called this method articulated planar reformation (APR). This results in a collection of sub volumes, each of which we can visualize separately in its own reference frame. When we apply this approach for each dataset of a cross-sectional or follow-up study, we can place the sub volumes side-by-side, which enables direct comparison of corresponding segments, even though in the original scans the animal posture was highly variable. An additional advantage of APR is that the segments, in our case bones, are automatically aligned with their principal axes, which is anatomically relevant and is more useful to our users.

We have shown how a two-level localization approach combined with an appropriate change metric, such as bone change, can be used to indicate interesting areas in the global whole-body view that can be further inspected in the focus view after interactively selecting the segment. In addition, we have implemented several approaches that allow for comparative visualization between multiple datasets, such as interactive switching, side-by-side, overlays and checkerboard visualizations. To further facilitate comparisons, we applied an additional rigid registration to each of the segments. Also, there is an option to show the local registration error mapped onto the atlas surface, which gives an indication of the accuracy of the registration and thus of the reliability of the comparison results.

Finally, we have presented an elaborate case study in which the potential role of our application was investigated in separate sessions with two experienced domain scientists. Although there were some questions about the usefulness of some of the visualizations, such as the checkerboard, the overall assessment was positive, with our primary user stating that he would certainly use it in his lab's research and the secondary user also expressing interest in applying the methods documented in this paper. We have thus shown that our approach is useful for comparing whole-body data in cross-sectional and follow-up studies.

For the time being, we decided to focus on the skeleton only, but our approach is also suitable for organs. Because of the lack of contrast in the data that was available, the location of the organs could only be estimated using interpolation based on the skeleton [17]. In the future, it will be interesting to use a contrast agent for imaging,

which would allow proper registration of the organs and would increase the usefulness of visualizing them in an articulated manner. In addition, our approach can be applied for other modalities, such as MRI, as long as articulated registration transforms and the corresponding atlas segments are available.

Furthermore, with the resolution of scanners growing, datasets are rapidly increasing in size. Loading several gigabyte-size datasets will be problematic on many systems. We want to implement a level-of-detail approach where we load a subsampled version of the data for the global APR view, while on selecting a segment, we load a subset of the data in full resolution to show in the focus view. Also, in order to maintain the modular structure of our design, we currently apply a straightforward resampling method to obtain a collection of sub volumes. However, we would like to replace this with an approach that directly renders the transformed data, in order to eliminate any unnecessary interpolation steps and to reduce the amount of memory that is required to keep the sub volumes in.

We plan to develop more advanced comparative visualization techniques to assist in multi-timepoint and intersubject comparisons. In this context, we will investigate relevant change features other than bone density. Depending on the feature, we plan to apply different visualization methods. For example, it may be desirable to geometrically visualize the amount of change. It would also be interesting to try and discern between physiological changes and registration errors.

Globally speaking, we aim for our approach to become an invaluable and general tool for cross-sectional and follow-up studies in preclinical small animal research.

Acknowledgements

APR for Change Visualization in Small Animal Imaging

5

Automated bone volume and thickness measurements in small animal whole-body MicroCT data

Chapter 5

Abstract

Purpose: Quantification of osteolysis is crucial for monitoring treatment effects in preclinical research and should be based on MicroCT data rather than conventional 2D radiographs, to obtain optimal accuracy. However, data assessment is greatly complicated in the case of three dimensional data. This paper presents an automated method to follow osteolytic lesions quantitatively and visually over time in whole-body MicroCT data of mice.

Procedures: This novel approach is based on a previously published method to coarsely locate user defined structures of interest in the data and present them in a standardized manner (Baiker et al. 2010, Kok et al. 2010). Here, we extend this framework by presenting a highly accurate way to automatically measure the volumes of individual bones, and demonstrate the technique by following the effect of osteolysis in the tibia of a mouse over time. Besides presenting quantitative results, we also give a visualization of the measured volume for qualitative assessment. In addition, we describe an approach to measure and visualize cortical bone thickness, which allows assessing local effects of osteolysis and bone remodeling. The presented techniques are fully automated and therefore allow obtaining objective results, which are independent of human observer performance variations. In addition, the time typically required to analyze whole-body data is greatly reduced.

Results: Evaluation of the approaches was performed using MicroCT follow-up datasets of fifteen mice ($n = 15$), with induced bone metastases in the right tibia. All animals were scanned three times: at baseline, after three weeks and after seven weeks. For each dataset, our method was used to locate the tibia and measure the bone volume. To assess the performance of the automated method, bone volume measurements were also done by two human experts. A quantitative comparison of the results of the automated method with the human observers showed, that there is a high correlation between the observers ($r = 0.9996$), between the first observer and the presented method ($r = 0.9939$) and also between the second observer and the presented method ($r = 0.9937$). In addition, Bland-Altman plots revealed excellent agreement between the observers and the automated method (Interobserver bone volume variability: $0.59\pm0.64\%$, Obs1 vs. Auto: $0.26\pm2.53\%$ and Obs2 vs. Auto: $-0.33\pm2.61\%$). Statistical analysis yielded no significant difference ($p = .10$) between the manual and the automated bone measurements and thus the method yields optimum results. This could also be confirmed visually, based on the graphical representations of the bone volumes. The performance of the bone thickness measurements was assessed qualitatively.

Conclusions: We come to the conclusion that the presented method allows to measure and visualize local bone volume and thickness in longitudinal data in an accurate and robust manner, proving that the automated tool is a fast and user friendly alternative to manual analysis.

Bone Volume and Thickness Measurements in MicroCT Data of Mice

5.1   Introduction

Breast cancer metastasizes preferentially to bone. Post mortem evaluation revealed that 70% of patients who died of breast cancer had bone metastases present in the skeleton [135]. Bone metastases cause severe morbidity in living patients such as bone pain, fracture, hypercalcaemia and nerve compression [136, 137]. As a result, quantification of osteolytic lesion size is pivotal in preclinical research of metastatic bone disease and treatment evaluation in small animal models.

Osteolysis is currently quantified using 2D radiographs [138, 139]. The scoring of these radiographs is performed manually by drawing a Region-of-Interest (ROI) around the lesion and measuring the bone area. The problem with this procedure is that lesions may be projected on top of each other and will therefore be underestimated when quantified, due to the flattening of the three dimensional structure [140] (Fig. 5.1). The same may happen for lesions on the side of bone. Furthermore, performing the analysis manually is prone to observer bias. MicroCT datasets provide spatial information, suitable for measurements of various bone parameters such as bone volume, bone thickness and bone mineral density. These measurements are potentially more informative than the radiographic analyses. Also, MicroCT enables the researcher to study the overall bone structure.

The use of MicroCT for quantitative measurements is not without difficulties. The shape and position of a Volume-of-Interest (VOI, the three dimensional counterpart of a ROI in 2D) in a 3D dataset greatly influence the measurement results. Therefore, it is crucial that the selection of a VOI is reproducible and not affected by the scan orientation or the observer who performs the procedure. We previously published a manual approach for the normalized selection of a region of interest in complex shapes [140]. This manual approach provides good and reproducible results but is very time consuming and requires well trained observers.

The comparison of whole-body datasets from longitudinal studies is even more difficult. Variation in posture of the animal during scans taken at different scan dates makes it nearly impossible to spot subtle disease induced differences between scans [17]. We previously published an approach to automatically align the skeletons of animals that were scanned at different points in time. The method can handle large postural differences between animals and as a result, specifically designed holders that are sometimes used to coarsely align animals [18], are not required. In addition, the user can select individual bones and generate side-by-side visualizations of these bones from multiple longitudinal datasets (Fig. 4.3). Such normalized visualizations greatly facilitate detailed qualitative assessment of structures in multiple complex and large datasets [16].

Here we describe an addition to this method, which enables the user to perform automated quantitative measurements of bone volume and thickness alongside the visual output. For evaluation, we applied the method to segment the femur and the tibia/fibula in whole-body follow-up MicroCT datasets and measured the bone volume and cortical thickness at three points in time: baseline, three weeks and seven weeks. To test whether this approach could be used to quantify biologically relevant changes in bone volume, breast cancer cells were injected into the right tibia after the baseline scan. The left tibia
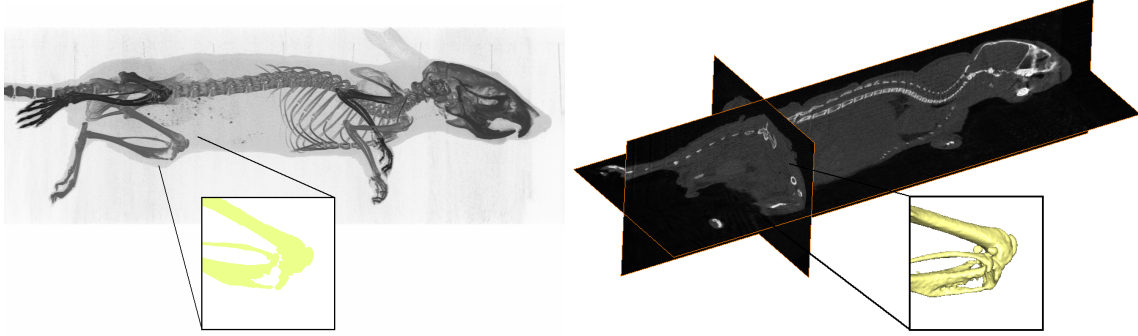
Figure 5.1: Examples of datasets for analysis of osteolysis based on a 2D radiograph (left) and a 3D MicroCT dataset (right). The insets are examples of the target structure to be analyzed. A ROI can easily be determined on the left whereas definition of a VOI on the right is not straightforward.

remained untreated and served as a reference. The results of the automated measurements are compared to manual measurements of two experts. We show that the automated segmentation and volume measurements perform equally accurate and reproducible as manual segmentation and volume measurements.

In summary, the goals of this work are to:

- Automate the task of measuring the volume of a user defined bone in whole-body in vivo MicroCT data and demonstrate the method by measuring the bone volume of the proximal tibia/fibula at several points in time.

- Compare the automated measurements with two human observers and show that the results are not significantly different.

- Present a way to assess the measurement quality visually, by providing proper visualization and

- Present a method to assess effects of osteolysis and bone remodeling locally (site-specific bone loss or gain) by automatically measuring and visualizing cortical bone thickness.

5.2 Materials and Methods

5.2.1 Animals

Fifteen ($n = 15$) female nude mice (BALB/c nu/nu, 6 weeks old) were acquired from Charles River (Charles River, L'Arbresle, France), housed in individually ventilated cages, food and water were provided ad libitum. Surgical procedures and MicroCT imaging were performed under injection anesthesia ($100mg/kg$ ketamine + $12.5mg/kg$ xylazine). Animals were sacrificed by cervical dislocation at the end of the experimental period. Animal experiments were approved by the local committee for animal health, ethics and research of Leiden University Medical Center.
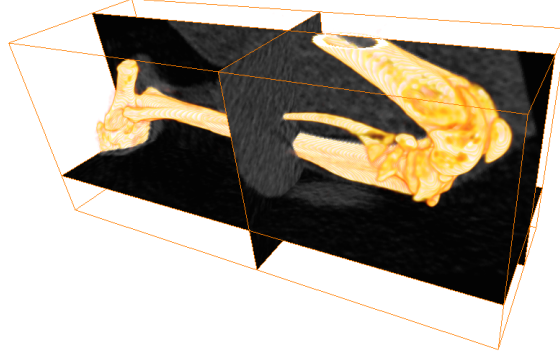
Figure 5.2: Example of an automatically determined subvolume, including the right tibia. The bone surface is shown together with the corresponding subvolume.

5.2.2 Cell Lines and Culture Conditions

The cell line MDA-231-B/Luc+ (hereafter MDA-BO2), a bone-seeking and luciferase-expressing subclone from the human breast cancer MDA-MB-231 [141,142], was cultured in DMEM (Invitrogen, Carlsbad, CA USA) containing $4.5g$ glucose/l supplemented with 10% fetal calf serum (FCS) (Lonza, Basel, Switzerland), $100units/ml$ penicillin, $50\mu g/ml$ streptomycin (Invitrogen) and $800\mu g/ml$ geneticin/G418 (Invitrogen). The cells were monthly checked for mycoplasma infection by PCR. The cells were donated by G. van der Pluijm (Leiden University Medical Center, Leiden, The Netherlands).

5.2.3 Experimental Setup

MDA-BO2 cells were injected into the right tibiae as described previously [142]. In brief, two holes were drilled through the bone cortex of the right tibia with a 25-gauge needle (25G 5/8, BD MicroFine, Becton Dickinson, Franklin Lakes, NJ USA) and bone marrow was flushed out. Subsequently, 250,000 MDA-BO2 cells/$10\mu l$ PBS was injected into the right tibiae of the animals. MicroCT scans were made before the tumor cell inoculation (T0) in supine position, three weeks after tumor cell inoculation (T1) in prone position and seven weeks after tumor cell inoculation (T2) in supine position. The animals were scanned with arbitrary limb position.

5.2.4 MicroCT Data Acquisition

MicroCT scans were made using a SkyScan 1076 MicroCT scanner (SkyScan, Kontich, Belgium) using a source voltage and current set to 50kV and $200\mu A$ respectively, with an X-ray source rotation step size of $1.5°$ over a trajectory of $180°$. Reconstructions were made using the nRecon V1.6.2.0 software (SkyScan) with a beam hardening correction set to 10%, a ring artifact correction set to 10 and the dynamic range set to -1000 - 4000 Hounsfield Units (HUs). The datasets were reconstructed with voxelsize $36.5 \times 36.5 \times 36.5\mu m^3$. Neither cardiac nor respiratory gating was used.

5.2.5   Manual Segmentation of the Tibia / Fibula

To assess the performance of the automated tibia volume measurements, two field experts were asked to segment the proximal part of the right tibia. To be able to use the data at full resolution, this was not based on the whole-body dataset but on a subvolume, corresponding to the right tibia, which was automatically determined following the procedure in Fig. 4.2. An example of such a subvolume is shown in Fig. 5.2. Starting with this subvolume, the experts were asked to segment the proximal part of the tibia/fibula, i.e. the part between the knee and the location where tibia and fibula separate. The manual segmentation was done using a tool that was developed in-house with MeVisLab V1.6 (MeVis Medical Solutions AG, Bremen, Germany) [140]. First, the user navigated through the subvolume by means of three orthogonal slices (see Fig. 5.2) and annotated the approximate bone centers at about twenty different locations in the femur and tibia, starting from the most proximal location in the femur and proceeding via the knee to the most distal location, in the tibia. Subsequently, cubic B-splines were fitted through these points, yielding a smooth curved line that runs approximately in the center of the femur and tibia, i.e. a bone 'centerline'. Subsequently, the user could navigate through the volume using slices that are perpendicular to this centerline.

Proceeding through the volume along the centerline, the expert first selected the slice (i.e. a flat plane) in the knee, which best separates the femur and the tibia, and second selected the slice, where the tibia and the fibula connect distally. To finally measure the bone volume in the region between the two slices, a three dimensional region grower was used. Starting from one or multiple seed point(s) set by the expert, this region grower decided, based on a user-defined threshold value, if the surrounding voxels are bone or not. This was iteratively repeated, until all bone voxels between the two slices were identified. Multiple seed points were necessary in case of fractured bone.

After segmentation, the number of bone voxels was determined using a threshold value to separate bone from background. To determine the optimum threshold for the in vivo datasets, the tibia of one of the animals was scanned ex vivo with high resolution ($9.125 \times 9.125 \times 9.125 \mu m^3$) after the follow-up experiment. Subsequently, the tibial bone volume was measured. To find the optimum threshold, for segmentation of bone from the background in the low-resolution data, the threshold was set such that the volume of the tibia of the same mouse in the low resolution data was the same as the volume of the tibia in the high resolution data. This threshold was kept constant for segmentation of all datasets. The result was a volume dataset with the same size as the initial subvolume with voxels labeled as relevant bone, i.e. the proximal tibia/fibula, and background (including irrelevant bone). Therefore, the bone volume of the proximal tibia/fibula could be determined by multiplying the total amount of bone voxels with the voxel volume i.e. in our case amount_of_voxels $* (36.5 \times 36.5 \times 36.5 \mu m^3)$. To be able to assess the quality of the segmentation visually, we provided a surface representation of the manually segmented subvolume. The tibia/fibula bone volume served as the reference for the automated method presented in the next subchapter.

5.2.6 Automated Segmentation of the Tibia / Fibula

An automated method should yield results that are as similar as possible to the results a human observer would obtain. Therefore, it should be designed such that it mimics the manual procedure as much as possible. Just as for the manual segmentation, presented in the previous subchapter, the automated segmentation was based on a subvolume as shown in Fig. 5.2 and the goal was to segment the proximal part of the tibia/fibula. First, a centerline was determined that runs through the center of the femur, the knee and the center of the tibia, based on the registration of the skeleton atlas to the MicroCT data. To this end, we defined 21 bone center locations (10 in the femur, 11 in the tibia) in the atlas. Subsequently, if the atlas bones are registered to the data (Fig. 4.2b), these atlas bone center locations are approximately in the bone centers of the femur and the tibia in the MicroCT data (the bone center locations do only have to be defined once for the atlas). Subsequently, a bone centerline was derived using cubic B-spline fitting through the bone centers. Next, the volume was segmented into bone and background, using global thresholding with the same threshold as was used for the manual segmentation (see previous subsection). Following the bone centerline from the knee towards the distal part of the tibia, the separation of the tibia and the fibula was determined using a hierarchical clustering technique with single linkage [143] that determined the number of bone clusters at regular spaced locations along the centerline. The Euclidean distance between points was chosen as the dissimilarity measure. The transition from two clusters (tibia and fibula) to one cluster identified the location of bone separation. Fig. 5.3 (right) shows a slice, perpendicular to the centerline, which is close to this point (tibia = large spot, fibula = small spot).

Separation of the tibia/fibula from the femur was done in a slightly different way as compared to the manual procedure, because it is very difficult to automatically determine a flat separation plane within the knee. Therefore, we chose to rely on a classifier that automatically separates all voxels labeled as 'bone' (i.e. after thresholding) into the two classes 'femur' and 'tibia/fibula'. The classifier was trained using volumetric (tetrahedral) meshes of the femur and tibia atlas after registration (Fig. 4.2b). Each node location of the meshes was weighted with a 3D Gaussian probability density function with width h (Parzen kernel density estimation [143]). Subsequently, all individual probability densities were summed up, yielding a bone dependent posterior probability density value within the entire data volume. A voxel labeled as 'bone' can thus be identified as 'femur' or 'tibia/fibula', depending on which of the two classes has the highest posterior probability at that voxel location. The parameter h was optimized using a leave-on-out test, based on the available datasets. Finally, the bone volume of the proximal tibia/fibula could be derived by counting the bone voxels classified as 'tibia/fibula' along the centerline, up to the tibia/fibula separation determined before and multiplying the total amount of bone voxels with the voxel volume. To assess the quality of the automated segmentation visually, we provided a surface representation of the result.
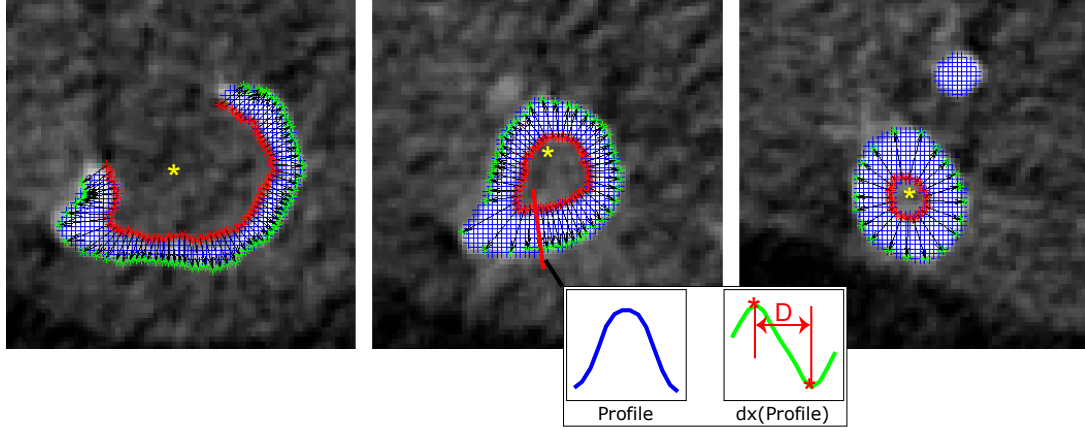
Figure 5.3: Demonstration of how the bone thickness D is determined automatically if osteolytic lesions are present. Shown are slices from the MicroCT subvolume that are orthogonal to the centerline, with an overlay of the voxels labeled 'bone' (blue net). Along the bone centerline (orange stars), grayvalue profiles are taken in axial direction at evenly spaced locations along the centerline. Shown are (left) a location close to the knee, (middle) a locations halfway between the knee and the tibia/fibula separation and (right) close to the tibia/fibula separation. Points on the inner boundaries are indicated by red stars, corresponding points on the outer boundaries by green stars. The black arrows indicate the directions, along which the grayvalue profiles for the bone thickness measurement are derived. An example of a profile path is shown in red (middle). The inset shows an example of a grayvalue profile in blue and its gradient values in green (dx symbolizes a mathematical derivation). The bone boundaries can be found where the gradients are maximum (red stars in the inset) and the bone thickness D is the distance between the boundaries.

5.2.7 Automated Segmentation of the Femur

As a proof of concept that the automated segmentation method can be applied to other skeletal elements besides the tibia as well, we demonstrate an automated segmentation of the femur. The femur is connected proximally to the pelvis and distally to the tibia. Following the procedure given in Section 5.2.6, the tibia was separated from the femur in a first step. Second, volumetric meshes of the atlas femur and the atlas pelvis after skeleton registration were used to derive a three dimensional posterior probability density function for these bones and to determine the separation of pelvis and femur, following the same procedure as described in in Section 5.2.6. The kernel width h was identical to the one used for the separation of the tibia and the femur. To assess the reproducibility of the volume measurements, the volume of the left femur of three animals was measured at all points in time and compared to the volume of the right femur over time. In addition, the bones were segmented manually, to assess measurement accuracy. To ensure that the influence of the induced cancer cells had a minimal effect on the femur bone volume, we chose three animals where osteolysis had only slightly progressed over time.

5.2.8 Automated Bone Thickness Measurements

Accurate knowledge of local bone thickness enables to follow the progress of osteolysis and bone remodeling over time. Therefore, a method is required to measure bone thickness in 3D and to relate the measurement to the exact location on the bone. Above that, the method should be able to handle severe structural changes over time, induced by osteolysis. There are mainly two approaches described in the literature to assess bone thickness in volumetric data: volume-based methods and surface (feature)-based methods [144]. These are focusing mainly on measuring trabecular bone and the approaches generally take the entire image domain into account. The advantage is that structures with very different shape can be analyzed. Although the approaches could be used for measuring cortical bone as well, the tube-like shape of long bones enables another approach. Since the registration of the skeleton atlas to the data yields a coarse segmentation of the skeleton, we can map a bone centerline, defined in the atlas femur and tibia, to the femur and tibia in the data. Subsequently, we can employ a technique similar to that presented in Van der Geest et al. [145], where the authors measure the diameter and wall thickness of blood vessels in MRA and CTA, based on slices that are orthogonal to the vessel centerline. The great advantage of relying on a centerline is that it is possible to determine exactly at which locations along the centerline the thickness should be measured. The main difference between analyzing vessels and potentially osteolytic bone is that vessels are continuous structures while bone can be highly fractured and contain holes.

The methods for trabecular thickness measurement generally take the entire image domain into account, which can be very time consuming, especially for large volumes or surfaces with a great amount of vertices. The proposed approach enables to greatly reduce computational burden. Above that, being able to define the thickness measurement based on a centerline allows to sample certain areas more densely than others, yielding more accurate measurements.

To determine the cortical bone thickness of the tibia automatically, we relied on the bone centerline presented in the previous section and the subvolume according to Fig. 5.2. At regularly spaced locations, following the centerline in distal direction, grayvalue profiles were extracted in axial direction, starting from the centerline and progressing outwards. In total, 360 profiles were taken per location, with 1° angle difference between them, covering an entire circle, oriented orthogonal to the centerline. Since the centerline lies in a low intensity area (bone marrow), the grayvalue profile will consist of low values at the beginning, high values within the bone and again low values outside the bone (muscle tissue). An example of such a profile is given in Fig. 5.3 (middle, inset). Subsequently, the inner boundary of the bone can be determined, using the highest positive gradient of the profile. Doing this for all 360 profiles, yielded 360 points located at the inner boundary of the bone. However, since the centerline may not always lie exactly in the center, these points are usually not evenly distributed along the boundary. Therefore, we applied an additional resampling step so that the points had a minimum distance of one voxel. Examples of resulting inner boundaries are shown in Fig. 5.3 (red stars). Next, again grayvalue profiles were taken, but this time orthogonal to the inner boundary of the bone, starting inside the bone and progressing outwards. An example path of such a profile is shown as a red line in Fig. 5.3 (middle). Finally, the bone thickness D could
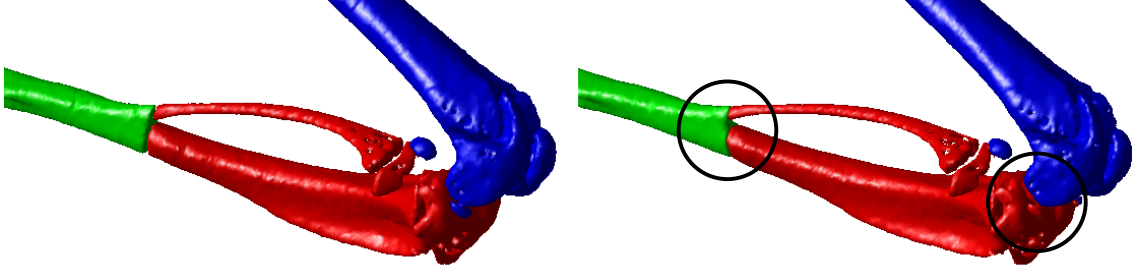
Figure 5.4: Bone surface visualization after manual (left) and after automated (right) segmentation of the proximal tibia/fibula. (femur = blue, proximal tibia/fibula = red, distal tibia/fibula = green). The circles highlight differences between the segmentations.

be determined using the highest positive and the highest negative gradient of the profile, demarcating the inner and the outer boundary of the bone. This is demonstrated in the inset in Fig. 5.3 (middle). Hence, our definition of bone thickness is the distance from the inner boundary to the outer boundary of the cortex, orthogonal to the inner boundary.

The bone thickness measurements can be uniquely related to the location on the bone, where they were derived. To be able to assess the bone thickness locally and still have the anatomical context information available, we present a visualization that is based on a surface representation of all bone in the subvolume (Fig. 5.2). To each location on the bone surface, we linked the corresponding bone thickness and assigned a value-dependent color. The result is a surface representation of the bone, on which the color indicates the bone thickness. The automated segmentations and bone thickness measurements and visualizations were performed using Matlab 2010b (The Mathworks, Natick, USA).

5.2.9   Quantitative Analysis of Measurement Results

To assess how similar the results of the automated method and the human experts are, Bland-Altman [146] plots as well as Pearson's correlation coefficients are presented. To investigate in detail the influence of the time point (i.e. baseline, first and second follow-up), the bone (i.e. healthy and pathologic) and the observer (i.e. automated, observer 1 and observer 2) on the bone volume measurement, we performed a statistical analysis using a three-way repeated measures analysis of variance (ANOVA) [147], with the bone volume as the dependent variable and observers, bone (i.e. healthy and pathologic) and time point as the independent variables ($3 \times 2 \times 3$ levels). A repeated measures design requires the variances of the differences between levels to be equal. Therefore, Mauchly's sphericity test should be non-significant if we are to assume that the condition of sphericity has been met. If the results of the test indicated that the assumption of sphericity was violated, the degrees of freedom were corrected using Greenhouse-Geisser estimates of sphericity [147]. To identify significant differences between group means for main and interaction effects, a Tukey HSD (honest significant difference) post hoc test was used. Effects were considered to be significant if $p < .05$. The statistical analysis was performed using Statistica 8.0 (StatSoft, Tulsa, USA).
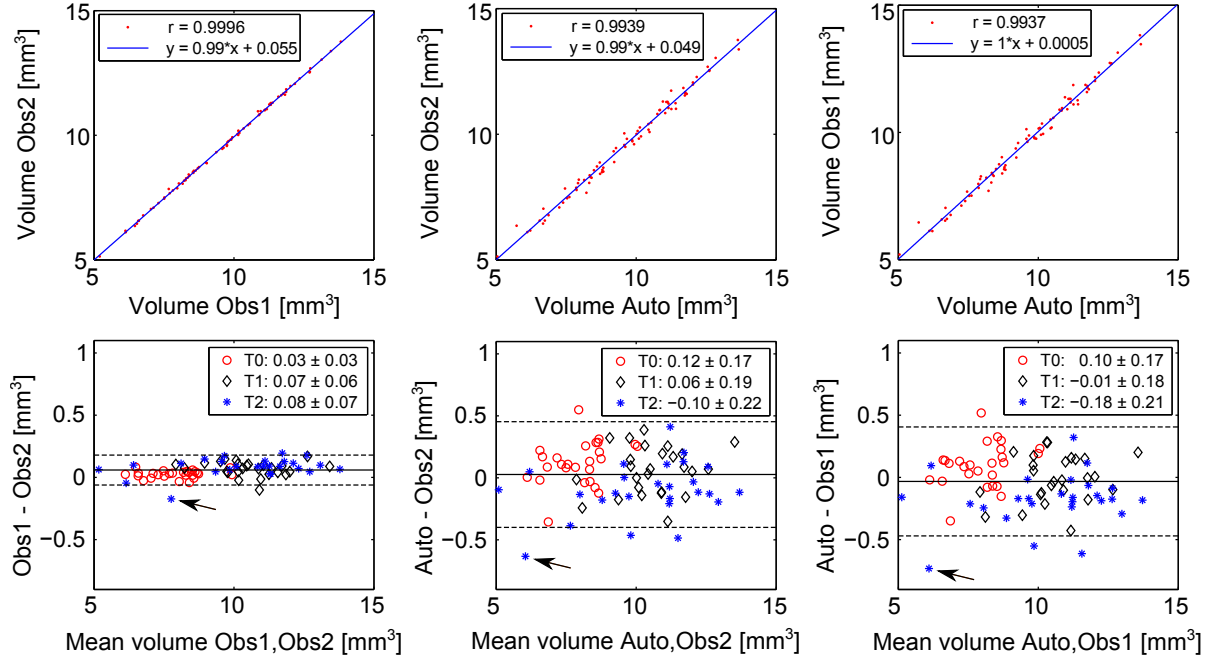
Figure 5.5: (Top row) Correlation between the measurements (in mm^3) of the two human observers and the automated method. Shown are Obs1 vs. Obs2, Auto vs. Obs2 and Auto vs. Obs1. The blue line represents a linear best fit, defined by the function in the legend. The Pearson correlation r, based on the data (red), is also shown in the legend. (Bottom row) Bland-Altman plots representing the measurement agreement between the two human observers and the automated method. The black lines indicate the grand means (–) ± 1.96 times the standard deviation (- -), which are $0.06 \pm 0.12 mm^3$, $0.03 \pm 0.43 mm^3$ and $-0.03 \pm 0.44 mm^3$ respectively. The arrows indicate the measurement with maximum disagreement between the observers. To assess, if the agreement is dependent on the time point when the data was acquired, these are shown in different colors (Baseline or T0 = red circles, T1 = black diamonds, T2 = blue stars). Note that the values in the legends are the means ± 1 time the standard deviation.

5.3   Results

To be able to assess the accuracy of a manual and an automated segmentation of the proximal tibia/fibula, surface visualizations are generated after the measurements. Examples are shown in Fig. 5.4.

The results of the correlation tests are shown in the top row of Fig. 5.5 and the measurement agreements are presented in the bottom row of Fig. 5.5. To assess a possible influence of the time point on the agreement, the data is shown for each time point individually (see legends).

Mauchly's test indicated a violation of the sphericity assumption and therefore degrees of freedom were corrected using Greenhouse-Geisser estimates of sphericity (see Tab. 5.1 in the 'Appendix' for details). The results show that there are significant differences in measured bone volume for the main effect Time, $F(1.39, 16.73) = 28.80$, $p < .001$, as well as the interaction effects Method * Time, $F(1.63, 19.59) = 16.71$, $p < .001$, and Bone * Time, $F(1.08, 12.93) = 12.75$, $p < .05$. The Tuckey HSD post hoc tests revealed a
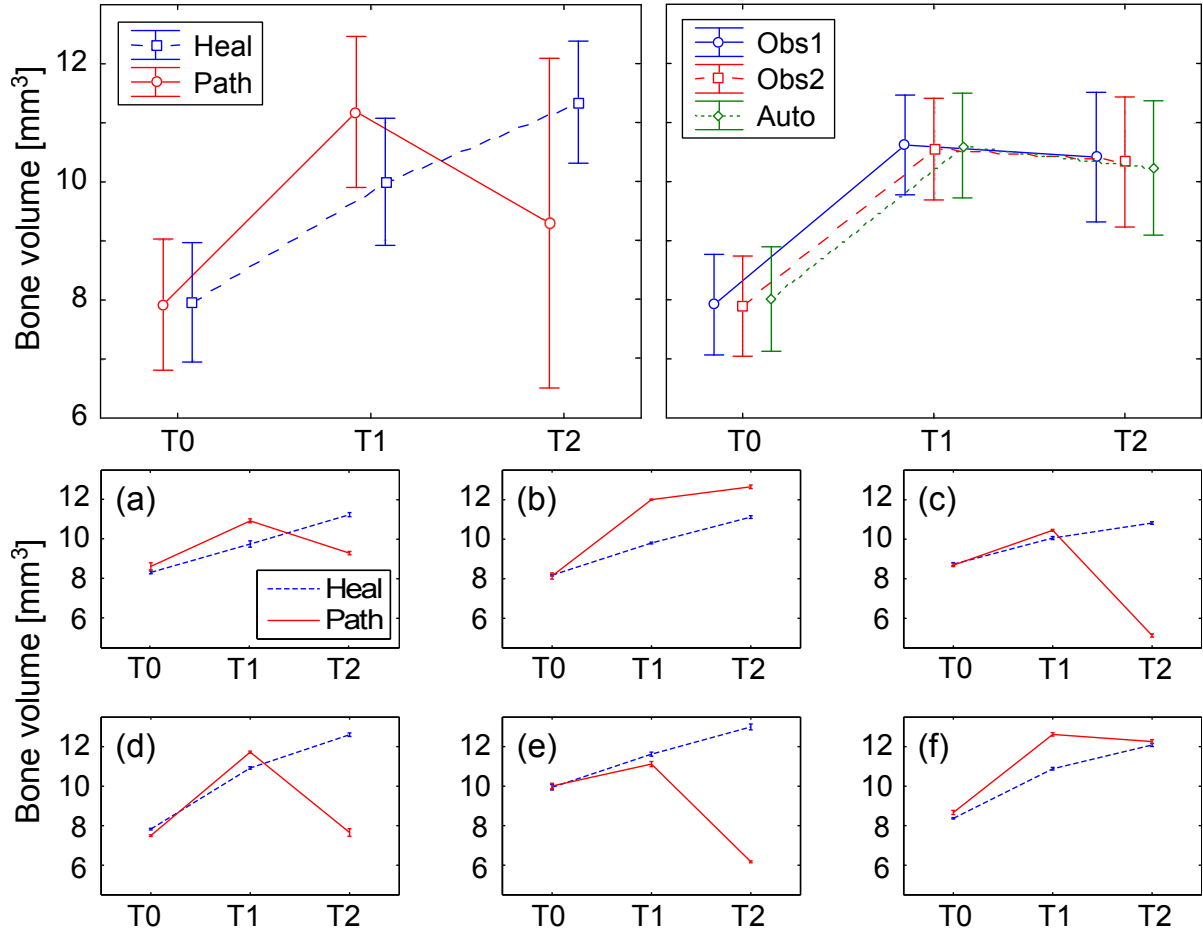
*Figure 5.6: (Top row) Mean bone volume (mm³) over time for the pathologic (Path) and the healthy (Heal) bones respectively, Bone * Time interaction (left), and bone volume over time for the two human observers (Obs1, Obs2) and the automated method (Auto), Observer * Time interaction (right). The results are based on including all mice. Error bars indicate 95% confidence intervals. (Middle and bottom rows) Mean bone volume (mm³) and the standard deviation of the healthy (Heal) and pathologic (Path) bones for six different mice (a-f) over time, averaging the measurements of the automated method and the two human observers.*

significant difference in bone volume between T0 and T1 ($p < .001$) as well as T0 and T2 ($p < .001$). There was no significant difference between T1 and T2 ($p > .05$).

For the Bone * Time interaction effect (Fig. 5.6, top left), relevant significant effects were present for healthy vs. pathologic bone at T2 ($p < .001$), but not at T0 and T1 (both $p > .05$). For the Method * Time interaction effect (Fig. 5.6, top right), relevant significant effects were present for Obs1 vs. Auto and Obs2 vs. Auto at T0 ($p < .05$ and $p < .001$) but not for Obs1 vs. Obs2 at T0 ($p > .05$). Furthermore there were significant effects for Obs1 vs. Auto and Obs2 vs. Auto at T2 ($p < .001$ and $p < .05$) but not for Obs1 vs. Obs2 at T2 ($p > .05$). There were no significant effects at T1.

The results of the comparison of the difference in bone volume between healthy and pathologic bone for six different mice are given in Fig. 5.6 (middle and bottom rows).

The results of the femur segmentation and subsequent volume measurements are

shown in Fig. 5.7. The average volume of the right and the left femur was $0.89 \pm 0.64\%$ when measured manually and $0.83 \pm 0.53\%$ when measured automatically. To see if there is a significant difference between the human observer and the automated method, a similar statistical analysis as presented in section 5.2.9. was performed, this time including one human observer instead of two. Mauchly's test indicated no violation of the sphericity assumption ($p > .05$). The results show that the main effect Method is significant $F(1, 2) = 92.894$, $p < .05$, and the mean difference between the automated and the manual method is $-2.15 \pm 0.75\%$. This means that the automated method results in lower measured volumes than the manual method.

A comparison of the development of the bone thickness over time for a healthy and a pathologic bone are given in Fig. 5.8 by means of bone surface visualizations where color indicates the bone thickness.

5.4   Discussion

In this article, we described a fully automated approach to analyze skeletal changes in rodent whole-body MicroCT scans. The automated approach is capable to 1.) align scans of the same animal, taken at different time points, 2.) automatically segment a subvolume (VOI) in these scans, 3.) measure the bone volume, 4.) measure cortical thickness and 5.) visualize it by means of assigning thickness-dependent colors. In addition, the user can visually check the segmentation performance using 3D bone surface representations and can generate normalized sections of identical sectioning planes in longitudinal scans for side-by-side comparison.

Conventional analysis of radiographs involves identifying osteolytic lesions manually. The procedure of manually drawing a region of interest is prone to observer bias and small changes in thickness or multiple lesions projected on top of each other are easily overlooked [140]. Manual analysis of MicroCT data is a better alternative, but is very labor intensive [140].

An automated method for MicroCT analysis has several advantages over manual analysis. The risk of non-objectivity and interobserver variability are greatly reduced by minimizing the active manual input of the researcher. Only an automated approach can be purely objective and handle every dataset in exactly the same manner. Additionally, an automated analysis method is much faster than any manual procedure. Thus, by automating the analysis, a relatively larger number of scans can be evaluated, compared to a human observer.

Researchers want to know exactly how quantified data is generated and tend to dislike automated 'black-box' approaches. To enable the researcher to check every step along the way, the automated method generates visualizations of the segmented volume. These visualizations can be evaluated after the analysis is complete. The automatic segmentation can be overruled manually or some datasets can be excluded from further analysis. Moreover, the cortical thickness maps enable the researcher to directly pinpoint where structural changes of the cortical bone occurred. This way, the cortical thickness maps help to identify areas of interest in the original scan data and in other modalities such as histological sections. Assessment of trabecular bone is not possible with the proposed
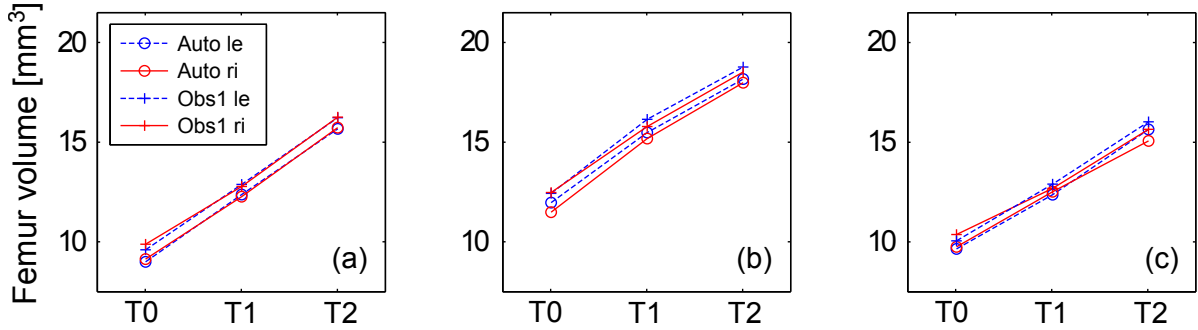
Figure 5.7: Result of the automated (auto) and manual (Obs1) volume measurement for the right (ri) and left (le) femur for three different mice (a-c) over time.

method, because the relatively low resolution of the in vivo data ($36.5 \times 36.5 \times 36.5 \mu m^3$) renders measuring the trabecular thickness accurately very difficult [148].

We validated the presented automated method by comparing it to the 'best available' method, namely manual bone segmentation and bone volume measurements. Therefore, we acquired datasets of 15 mice ($n = 15$) with induced bone metastases in the tibia at three points in time. The volume measurement results show that there is an excellent correlation between the human observers and the automated method: $r_{Obs1Obs2} = 0.9996$, $r_{AutoObs2} = 0.9939$ and $r_{AutoObs1} = 0.9937$. The Bland-Altman plots (Fig. 5.5, bottom row) based on all data indicate excellent agreement among the two human observers (interobserver variability) as well as the observers and the automated method. There is no obvious relation between the difference and the mean. Residual disagreement can therefore be explained by the bias and the deviation, which is very low in all cases, namely $0.59 \pm 0.64\%$, $0.26 \pm 2.53\%$ and $-0.33 \pm 2.61\%$ respectively. The residual errors are the result of mainly two factors that may influence the measurement outcome: the registration accuracy, and subsequently the segmentation accuracy, and the chosen threshold to separate bone from the background. The registration accuracy has the largest influence on the result and therefore, improving the accuracy would require a modification of the registration method. Special attention should be paid to the robustness of potential methods with respect to bone resorption. The thresholding procedure also influences the measured volume, because both values are inversely related i.e. if the threshold value increases, the volume decreases and vice versa. We chose a global threshold since the resolution of the in vivo data does not allow to reliably segment the trabecular bone [148] but methods including local thresholds may be more accurate, if data resolution increases.

Ideally, the automated measurements are identical to the manual measurements. The ANOVA revealed no significant difference between observers (Method, $p = .10$), which means that the automated method is performing equally well as the two human observers. However, the low p value indicates that significant interaction effects may be present. It appears that there is a dependency of the performance of the automated method on the time point since the automated method is significantly different from the human observers at T0 and T2. Visual inspection of Fig. 5.6 (top right) suggests overestimation of the volume at T0 and underestimation of the volume at T2. There is no significant difference at T1. This is supported by the Bland-Altman plots (Fig. 5.5, bottom row) in which

the mean difference in measurement is close to zero at T1. However, the differences are borderline and probably due to the very small variation between the human observers.

The bone volumes of pathologic bones were significantly decreased compared to the healthy bones at T2 (Fig. 5.6, top left). There are no significant differences at T0 and T1. There are two explanations why there is no volume decrease at earlier time points. Firstly, the bone marrow is partially flushed out of the bone during the intra osseous injection of tumor cells. This partial bone marrow ablation has profound anabolic effects on local bone turnover. Bone formation induced by bone marrow ablation reaches a maximum one week after the intervention. After this initial week the bone volume normalizes gradually over time as the bone recovers from the procedure, a process that can take weeks [149, 150]. Secondly, starting osteolytic lesions around the tumor create weak areas in the bone. The mechanical stress on other, healthy parts of the bone will increase due to these weak areas. Both the anabolic effects due to the partial bone marrow ablation and due to the increased mechanical stress result in a local increase of bone volume alongside osteolytic lesions. Combined, these anabolic and osteolytic processes influence the volume measurements as can be seen in Fig. 5.6 (middle and bottom rows, a-d and f). The cortical thickness maps provide an excellent tool to see exactly where the volume changes occur in relation to the osteolytic lesion site (Fig. 5.8).

The presented segmentation method is not restricted to the tibia, but can be applied to any bone of the skeleton in whole-body MicroCT scans, as long as it is contained in the MOBY mouse atlas [16, 17, 59]. We are currently implementing the volume measurements of every segmented skeletal element using the same principle. We segmented the femur as preliminary proof of concept. Several conclusions can be drawn from the results in Fig. 5.7. The volumes of the right and the left femur are very similar for the manual and the automated measurement, meaning that measuring the femur is highly reproducible. The automated method however, underestimates the volume compared the manual method. This underestimation is to be expected since the femur included in the MOBY mouse atlas does not include the femoral head and neck. Therefore the segmentation result 'cuts' the femoral neck approximately in the middle and the amount of underestimated volume thus corresponds to the volume of the femoral head and part of the femoral neck. Note that this is a systematic error and only leads to inaccurate results if the femoral head and neck are of particular interest within a study. The same type of measurement error may occur for other bones as well, since most of the bones in the MOBY atlas are simplified versions of the real bone shape. However, as is the case for the femur, this should not lead to problems because the error is systematic. If higher segmentation accuracies are required in a particular part of the bone that is simplified, another animal model with more details could be employed. One should however bear in mind that using simplified bone shapes has the advantage that the influence of e.g. differences in strain or animal size can be minimized by leaving out the fine details.

The increased radiation dose of MicroCT compared to radiographs has always been a major concern limiting its use in cancer research. This is not a problem anymore as modern MicroCT scanners can perform whole-body scans in less than a minute [151]. The delivered radiation dose during these scans is well below a dose that would affect tumor growth, even during longitudinal follow-up studies [151–153].
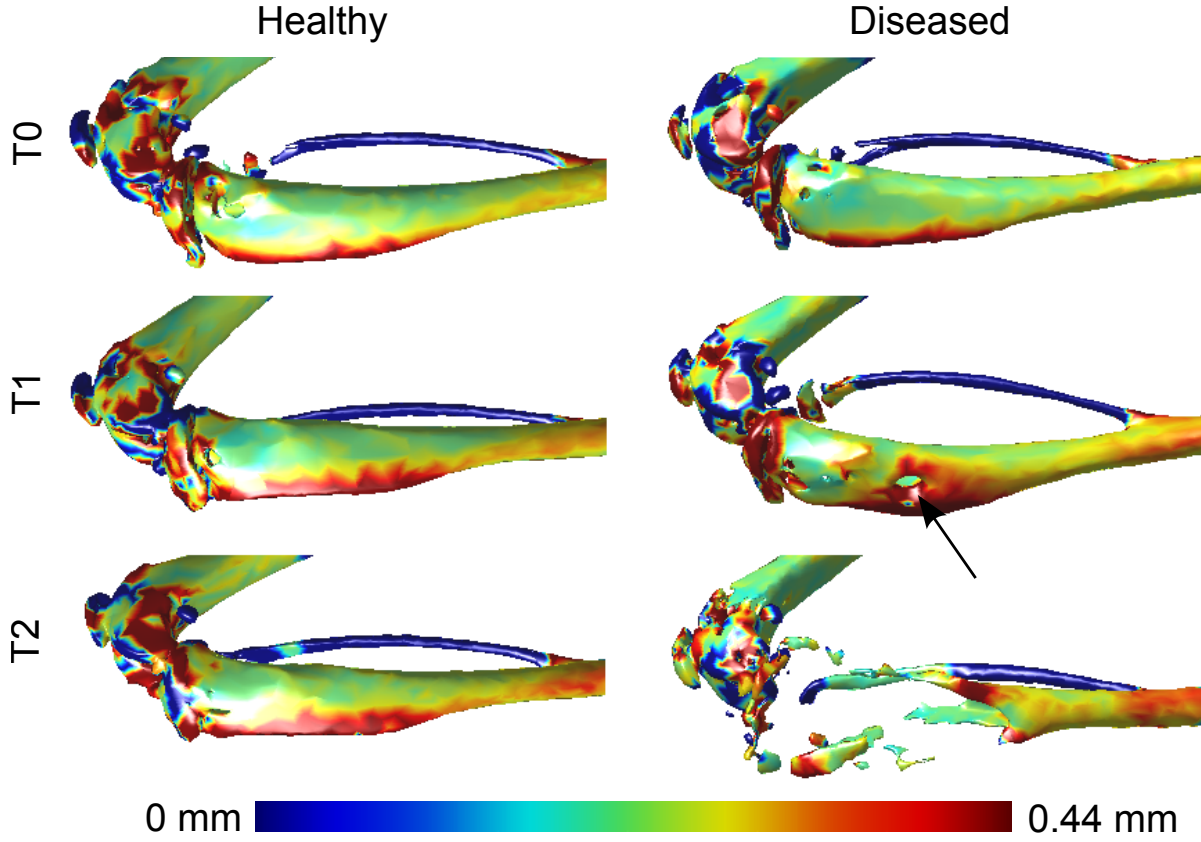
Figure 5.8: Comparison of the bone thickness development over time for a healthy and a pathologic (diseased) bone. Shown are bone surface representations. The colors indicate the bone thickness at each location on the bone. The bone marrow was partially flushed out of the bone during the intraosseous inoculation used to induce bone metastases. This partial bone marrow ablation leads to a local increase in bone volume preceding cancer-induced osteolysis [140]. The arrow indicates this local increase in bone thickness around the site of early osteolysis. Note that the measurements at the distal end of the femur and the proximal end of the tibia are not meaningful, because at these locations, a substantial amount of trabecular bone is present. However, bone thickness measurements are only meaningful for cortical bone.

All datasets used in this article have been generated with a standard scanning protocol using the Skyscan 1076 MicroCT. However, the described methods can be performed on any other whole-body MicroCT dataset acquired on a different machine and with a different protocol. Other scans might require an adjustment of threshold values and the initial scan resolution will always be a limiting factor during further analysis.

Finally we want to stress, that the described method is general and can be applied to others species as well as long as an anatomical skeleton atlas is available.

5.5   Conclusion

We suggested a new MicroCT analysis paradigm based on the combined approach of previously published methods for animal posture correction, normalized visualization of

follow-up data and the quantification and visualizations discussed in this paper. Together, this results in a fast and automated workflow, in which the user can easily compare whole-body MicroCT scans on the whole-body level, zoom in to the level of a single bone or bone segment of choice and gain qualitative and quantitative data of that segment. The animals can be scanned in any posture. Normalized and interactive side-by-side visualizations of the exact same section of skeletal elements at different time points can be generated from longitudinal scans in which one animal is scanned multiple times over time. The detailed side by side visualizations greatly help the researcher to identify changes in the skeleton. The researcher can then identify and zoom in on the bone or bone segment of interest and automatically generate quantitative volumetric data alongside visualizations of the segmented volume and visualizations of the cortical thickness of that specific skeletal element. This new workflow greatly reduces analysis time, aids the handling of complicated scan data and improves the overall qualitative and quantitative assessment of MicroCT scans. The method was validated by quantification of osteolytic effects over time in the tibia but can easily be adapted to other bones of the skeleton. In addition, the approach can be used for other species as well, given that an animal skeleton atlas exists for that animal.

Acknowledgements

Conflict of interest disclosure: The authors declare that they do not have a conflict of interests.

Appendix

5.6 Results of Mauchly's test and Greenhouse-Geisser correction

Table 5.1: Results of Mauchly's test and Greenhouse-Geisser correction.

| | Mauchly's test | | | | Greenhouse-Geisser correction | | | | | | | |
	W	χ^2	df	p	df M	df E	F	p	ϵ	Adj. df1	Adj. df2	Adj. p
Method	.05	33.72	2	.00	2	24	3.18	.06	.51	1.02	12.29	.10
Bone	1				1	12	0.69	.42	1	1.00	12	.42
Time	.57	6.26	2	.04	2	24	28.80	.00	.70	1.39	16.73	.00
Method * Bone	.18	18.9	2	.00	2	24	0.80	.46	.55	1.10	13.18	.40
Method * Time	.03	35.3	9	.00	4	48	16.71	.00	.41	1.63	19.59	.00
Bone * Time	.14	21.3	2	.00	2	24	12.75	.00	.54	1.08	12.93	.00
Method * Bone * Time	.05	31.3	9	.00	4	48	2.81	.04	.55	2.18	26.18	.07

Bone Volume and Thickness Measurements in MicroCT Data of Mice

6

Automated Registration of Whole-Body Follow-Up MicroCT Data of Mice

Chapter 6

Abstract

In vivo MicroCT imaging of disease models at multiple time points is of great importance for preclinical oncological research, to monitor disease progression. However, the great postural variability between animals in the imaging device complicates data comparison.

In this paper we propose a method for automated registration of whole-body MicroCT follow-up datasets of mice. First, we register the skeleton, the lungs and the skin of an articulated animal atlas (Segars et al. 2004) to MicroCT datasets, yielding point correspondence of these structures over all time points. This correspondence is then used to regularize an intensity-based B-spline registration. This two step approach combines the robustness of model-based registration with the high accuracy of intensity-based registration.

We demonstrate our approach using challenging whole-body in vivo follow-up MicroCT data and obtain subvoxel accuracy for the skeleton and the skin, based on the Euclidean surface distance. The method is computationally efficient and enables high resolution whole-body registration in $\approx$17 minutes with unoptimized code, mostly executed single-threaded.

6.1 Background

THE POSSIBILITY to scan the entire body of small animals with dedicated hardware in vivo offers great benefits for preclinical research, because it allows to follow e.g. pathology development over time within the same subject. This excludes intersubject variability and has ethical and economical benefits.

A problem that arises with imaging entire bodies is the potentially large postural variability of animals that are imaged at different time points (Fig. 1.3, left). This significantly complicates data examination, because researchers have to 'align' structures of interest visually and navigate through large whole-body datasets. For some applications, dedicated animal holders can be used to reduce the postural variability [18]. However, such holders may influence the study, e.g. by obstructing light in optical imaging based studies [5].

To deal with the problem of high postural variability, in [17] we presented a robust method for registration between the skeleton, the lungs and the skin of a mouse atlas (MOBY [59]) and whole-body MicroCT data of mice. We subsequently used the point correspondences on these structures to map the remainder of the body using Thin Plate Spline (TPS) interpolation. However, in areas with few correspondences, the accuracy of the mapping may be limited.

In this paper we aim at improving the accuracy of the TPS mapping by integrating intensity information during the registration. We present an accurate, time efficient and highly robust method for registration of follow-up MicroCT datasets that contain articulated objects. This we achieve by regularizing an intensity-based registration criterion with the Euclidean distance metric, based on sets of anatomical correspondences. We evaluate the method using non-contrast-enhanced MicroCT data of eight animals, imaged at two time points.

6.2 Previous work

Several strategies are described in the literature that focus on registration of images with multiple structures of interest with varying structural properties. Staring et al. [23] describe an approach that adds a local rigidity penalty term to the registration function in order to penalize the deformation of rigid objects. They apply the approach to CT follow-up data of the thorax. Somayajula et al. [19] present an intensity based registration of whole-body MicroCT follow-up datasets of mice. They register multiple levels of a scale-space simultaneously. A method that relies on skeleton segmentations from MicroCT is described in Li et al. [26]. The skeletons are aligned using nonrigid robust point matching, followed by intensity based nonrigid registration based on radial basis functions. Suh et al. [27] register the skeleton using extended demons with subsequent intensity based registration using normal demons. These approaches exploit the high CT contrast to avoid unrealistic bone deformation without [19] and with [23, 26, 27] using the skeleton explicitly. All methods may suffer from local minima when bones are in close proximity, but especially in case of large postural variability.
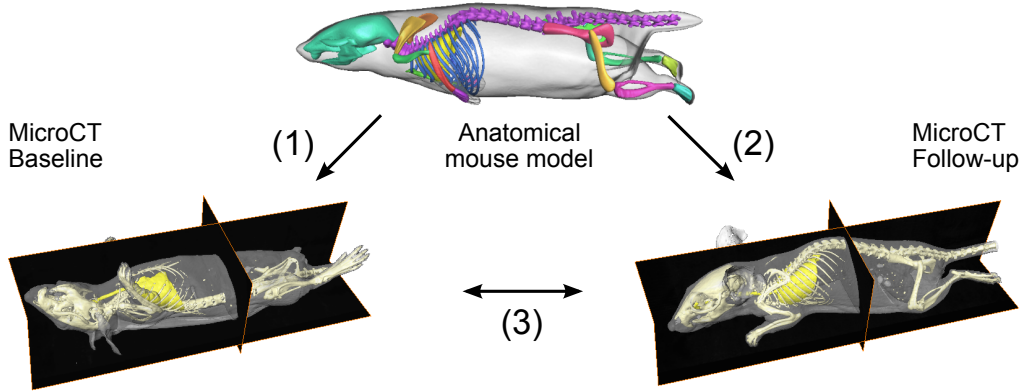
Figure 6.1: First, an anatomical animal atlas (skeleton, lungs, skin) is registered to a baseline (fixed image, 1) and one or multiple follow-up (moving image, 2) MicroCT datasets. The point correspondence between the atlas and the datasets allows to establish point correspondences between the datasets as well, which can subsequently be used to regularize intensity-based registrations (3).

A possibility to increase the robustness of whole-body registration is to model and register individual parts of an animal. Approaches range from registration of individual Volumes Of Interest and subsequent interpolation (block-matching), that do not take relationships between VOIs into account [31] to methods that register structures of interest simultaneously [34] or hierarchically [18]. Other methods are based on realistic anatomical modeling of the relationship between structures, so-called articulated registration approaches, and were applied to registration of hand radiographs in 2D [92] and mouse hind limbs [35].

6.3   Method: whole-body mouse registration

In the following, we shortly describe an atlas-based framework for articulated registration presented in earlier work [17] and then the proposed extension for intensity-based registration. An overview of the framework is shown in Fig. 6.1. The fixed and moving images are denoted with I_F and I_M respectively, and the transformation relating the two by $\boldsymbol{T_\mu}$, with parameters $\boldsymbol{\mu}$.

6.3.1   Articulated whole-body registration

The mouse atlas used in this work is the publicly available MOBY atlas [59] that we modified by manually segmenting individual bones and organs, identifying joint locations and adding anatomically realistic joint models. The registration of this atlas to MicroCT was presented in previous work [17] and will be described briefly. Using a hierarchical anatomical model of the skeleton, each atlas bone is registered individually to an *unlabeled* skeleton surface representation, using the Iterative Closest Point (ICP) algorithm [79]. In each step, the Degrees of Freedom (DoFs) of the transformation function are defined by the joint type, by which the current bone is connected to the bone that is higher in

the hierarchy. To account for differences in bone size, anisotropic scaling is added to the motion parameters of each bone. Thus, the DoFs vary between seven for a hinge joint (translation, non-isotropic scaling, one rotation) and nine for a ball joint. The surfaces of the lungs and the skin are subsequently registered, initialized by the skeleton registration result. The final result is a dense set of corresponding points on the skin, the skeleton and the lungs. Establishing such a point correspondence between the atlas and a target for data of several timepoints, allows to subsequently establish point correspondence between the timepoints as well (see Fig. 6.1). Corresponding pointsets of two different timepoints are in the following denoted as $\mathcal{Z}_F$ and $\mathcal{Z}_M$.

6.3.2 Regularized Intensity Based Registration

The articulated skeleton registration is surface-based and mostly neglects intensity information in the data. To combine the robustness of the articulated registration with the accuracy of intensity-based methods, we propose to regularize an intensity-based registration with the point correspondence from the articulated registration. Registration is formulated as an optimization problem:

$$\arg\min_{\boldsymbol{\mu}} \mathcal{C} = \arg\min_{\boldsymbol{\mu}} \mathcal{S}_{\text{sim}}(\boldsymbol{T_\mu}; I_F, I_M) + \alpha \mathcal{S}_{\text{CP}}(\boldsymbol{T_\mu}; \mathcal{Z}_F, \mathcal{Z}_M), \tag{6.1}$$

where the cost function $\mathcal{C}$ is optimized with respect to the transformation parameters $\boldsymbol{\mu}$. $\mathcal{S}_{\text{sim}}$ measures the image intensity similarity. We chose Normalized Cross Correlation (NCC), because all datasets are acquired with the same modality. We thus assume a linear relationship between the intensity values of I_F and I_M. $\mathcal{S}_{\text{CP}}$ is a metric incorporating the similarity of the corresponding pointsets $\mathcal{Z}_F$ and $\mathcal{Z}_M$ and is defined as the mean Euclidean distance between them:

$$\mathcal{S}_{\text{CP}} = \frac{1}{P} \sum_{\boldsymbol{x}_F^i \in \mathcal{Z}_F} \left\| \boldsymbol{x}_M^i - \boldsymbol{T_\mu}(\boldsymbol{x}_F^i) \right\|, \tag{6.2}$$

where P is the number of corresponding points, and $\boldsymbol{x}_F^i, \boldsymbol{x}_M^i$ corresponding points from the fixed and moving image pointsets, respectively. The two terms of Eq. 6.1 are weighted by the parameter α. The optimization problem is solved using a parameter-free Adaptive Stochastic Gradient Descent (ASGD) optimization routine [154], in a multiresolution fashion, using Gaussian pyramids. For each resolution, the optimal value of α is set manually, depending on how much the image intensity and the point distance measure should contribute to $\mathcal{C}$. In the first resolutions, $\mathcal{S}_{\text{CP}}$ should have a relatively large impact on $\mathcal{C}$, to remove large postural differences. Thus, α is set to a relatively large value because otherwise the optimization may get stuck in local minima. Assuming that afterwards I_F and I_M are coarsely aligned, the influence of $\mathcal{S}_{\text{CP}}$ can be gradually decreased and removed from $\mathcal{C}$ in the last resolution ($\alpha = 0$).

The intensity-based registration was initialized by a similarity registration (motion and isotropic scaling), followed by nonrigid registration with the transformation $\boldsymbol{T_\mu}$ parameterized by B-splines [155]. They were employed in a multigrid setting, gradually refining the B-spline control point grid over the resolutions.

(a) Moving I_M (b) IFFD   (c) TPS   (d) IFFD Reg   (e) Fixed I_F
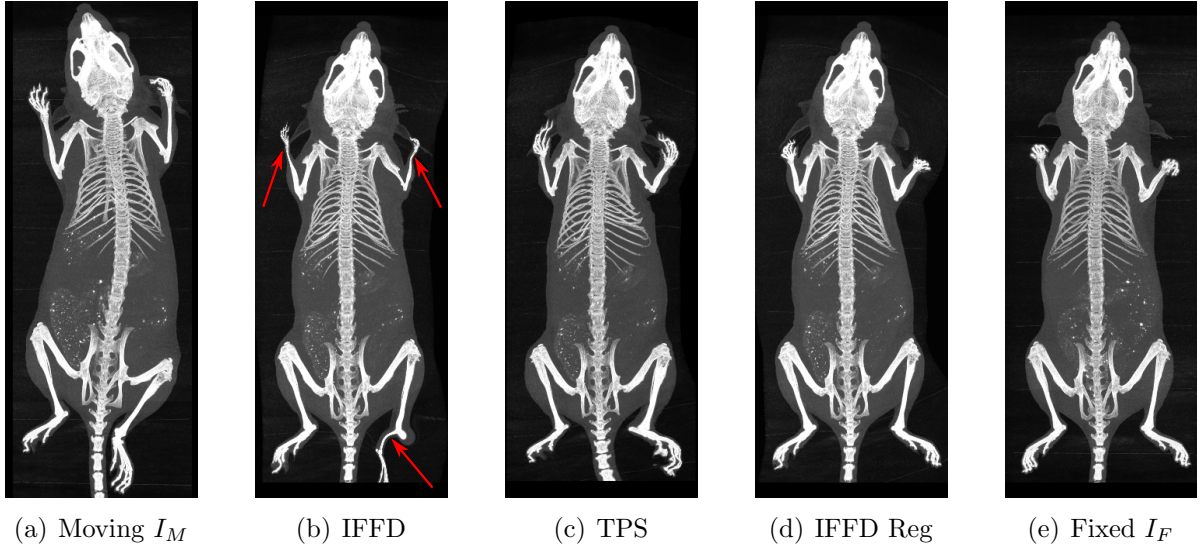
Figure 6.2: Dorsal-ventral maximum intensity projections of MicroCT volumes before and after registration with different methods. Note that (a) was acquired in prone, whereas (e) was acquired in supine position. The arrows indicate erroneous limbs after registration based on intensity information only. This is the animal shown in Fig. 6.4.

6.4   Experimental Setup

Eight female mice (Balb/c nu/nu, Charles River, L'Arbresle, France), 6 weeks old at baseline, were scanned twice, three weeks apart, once in prone and once in supine position and with arbitrary limb position. MicroCT (SkyScan 1076, Kontich, Belgium) parameters were: 1.5° steps, 180°, 50keV x-ray voltage, 200μA anode current, Al filter 0.5mm and exposure time 100ms. The datasets were reconstructed with built-in software (beam-hardening and ring artifact correction both 10) and a dynamic range of -1000 to 4000 Hounsfield units. No cardiac nor respiratory gating was used. The data was subsampled to 144^3 μm^3 voxelsize ($\approx 250 \times 200 \times 650$ voxels), smoothed with a Gaussian filter ($\sigma = 1$) and segmented using the Color Structure Code technique [156] with $T = 24$ for the skeleton and the skin and $T = 6$ for the lungs. Triangular surface meshes were extracted from the segmentations using Marching Cubes (more details in [17]).

Following the procedure in Section 6.3.1, we derived $\approx$2000 correspondences on the skeleton, the lungs and the skin. For the intensity-based registration, we used 5 resolutions (500 iterations) for the similarity registration and 6 resolutions (2000 iterations) for the B-Spline registration. α was kept constant at 0.05 in resolutions 1-4, decreased to 0.005 and 0 in resolutions 5 and 6 respectively (the corresponding parameter files are available at `http://elastix.isi.uu.nl/wiki.php`). Invertibility and smoothness of all final transformations was confirmed using the determinant of the Jacobian of the deformation fields, which was > 0 within all animals.

Table 6.1: Skeleton and skin surface distance and landmark localization accuracy (in voxels). Surface distances are based on eight animals and the landmark distances on a subset of three animals. (*) Results are based on a different, yet comparable dataset.

Skeleton distance	Mean	Median	Max	Min
Init	9.70 ± 11.68	5.59	81.16	3e-6
TPS	2.01 ± 2.72	1.32	36.91	3e-6
IFFD	1.19 ± 5.15	0.34	71.99	5e-7
IFFD Reg	0.49 ± 0.80	0.33	17.83	3e-7
Li et. al [26] (*)	0.61 ± 0.19	N/A	N/A	N/A
Skin distance	**Mean**	**Median**	**Max**	**Min**
Init	9.56 ± 10.30	6.46	76.62	9e-6
TPS	3.79 ± 3.63	2.71	36.70	1e-6
IFFD	1.37 ± 4.58	0.50	68.64	4e-7
IFFD Reg	0.83 ± 1.16	0.49	16.41	9e-8
Landmark distance	**Mean**	**Median**	**Max**	**Min**
Init	65.24 ± 32.81	64.52	131.62	4.91
TPS	6.25 ± 3.75	5.52	25.63	2.17
IFFD	3.75 ± 7.46	1.90	51.87	0.37
IFFD Reg	1.97 ± 1.72	1.57	11.51	0.37
Li et. al [25] (*)	3.46 ± 1.88	3.64	5.96	1.04

For evaluation, the following metrics were chosen: Normalized Cross Correlation (NCC) to assess the intensity similarity and the Dice Similarity Coefficient (DSC) to assess skeleton and skin segmentation accuracy. The DSC is defined as $2(V_1 \cap V_2)/(V_1 + V_2)$ and measures structural overlap. It is well suited for elongated and thin structures, which occur in our data (Fig. 1.3, left). We also determined the Euclidean Point to Surface Distance (EPSD) between the skeletons and skins of registered datasets. We excluded the tail, since it is irrelevant for most studies. Color-coded EPSD mapping to the surfaces allows to detect local registration inaccuracies. Finally, we assessed how well specific bone structures are registered, by measuring the Euclidean Point to Point Distance (EPPD) between 19 anatomical landmarks, manually indicated before and after registration, on distal body parts like the limbs, on the spine and on the ribs. Results are given after initialization, TPS interpolation, intensity-based registration without (IFFD) and with using regularization (IFFD Reg). For comparison with published work, we present results of Li et al. [26], because their datasets are comparable to ours.

Correspondence determination was done with Matlab 2010b (The Mathworks, Natick, USA) and the intensity-based registration using the ITK-based and publicly available `elastix` software [130] on an Intel Xeon E5620 8 cores (2.4GHz) and 24GB RAM. The time requirements were ≈5 mins. for IFFD and ≈17 mins. for IFFD Reg. (including ≈5 mins. to determine correspondence).

6.5   Results and Discussion

Qualitative results of the registration are shown in Fig. 6.2, quantitative results for the DSC and the NCC are presented in Fig. 6.3 and the surface distances and landmark localization accuracy before and after registration are given in Tab. 6.1 and Fig. 6.4. The very large difference between the metrics after initialization and after IFFG are an indication for the large postural differences between the animals. Comparing TPS and
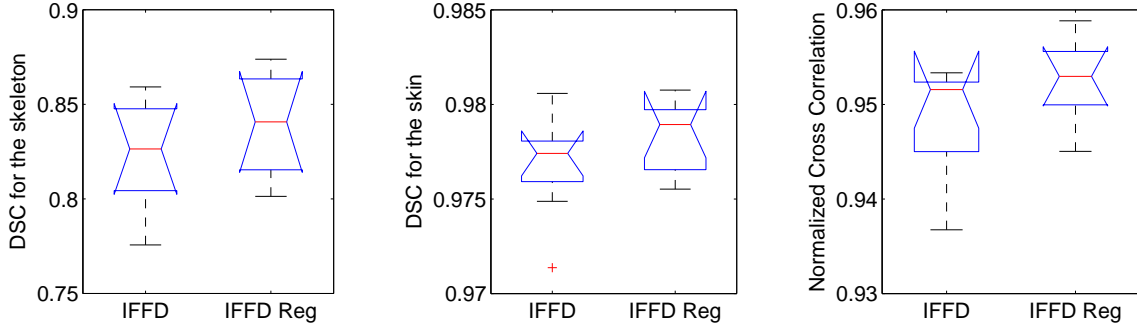
Figure 6.3: Boxplots of the DSC for the skeleton and the skin and the NCC, for IFFD and IFFD Reg. Notch overlap indicates no significant difference ($p \geq 0.05$) between medians. Note that after initialization, the medians are: DSC skeleton 0.15, DSC skin 0.81, NCC 0.65 and using TPS interpolation 0.42, 0.91 and 0.81.

IFFD, the average error is smaller for IFFD, but the maximum is much larger. The reason is the large initial postural differences between animals. TPS can deal with that and therefore, all body parts are registered equally well. IFFD is very accurate, when body parts lie within the registration capture range, but fails completely otherwise. Generally, the more distal to the body, the higher the error becomes. Fig. 6.4 and Fig. 6.2 support this because the error increases significantly at the limbs. The results of IFFD Reg reveal that our approach can handle large variability in the data without losing accuracy. The DSC plot (Fig. 6.3) shows excellent overlap for the skeleton and for the skin. We obtain subvoxel accuracy for bone and the skin in the surface distance measure (Tab. 6.1). The maximum distances mainly stem from the very distal ends of the limbs and the ribs for the skeleton, and folds for the skin (Fig. 6.4). In addition, IFFD Reg yields higher intensity similarity than IFFD (Fig. 6.3). For all presented metrics, IFFD Reg outperforms both, TPS and IFFD, proving that relying on point correspondence or intensity only is not sufficient for highly accurate registration, in case of large postural differences.

Compared to published data by Li et al. [25, 26], we have similar results for the skeleton distance and better results for the landmark localization. Their method pays special attention to registration of the ribs, thus it might yield more accurate results for these structures. However, they evaluate using ex vivo data, excluding rib movement artifacts. If accurate rib registration is required, an additional stiffness penalty could easily be added to our registration criterion [23]. In addition, we want to stress that the method in Li et al. requires 260 minutes for registration and our method takes $\approx$17 minutes. We realize that those experiments were performed on outdated hardware (Pentium PC, 2GHz, 1GB RAM), but most of our code was executed single-threaded and in addition, our image domain was approximately twice as big. It would be interesting to compare our method to the promising approach of Suh et al. [27] as well, which seems to be more time efficient and more accurate, compared to Li et al.

Finally we want to point out, that the registration of an atlas yields a segmentation of the skeleton as a by-product.
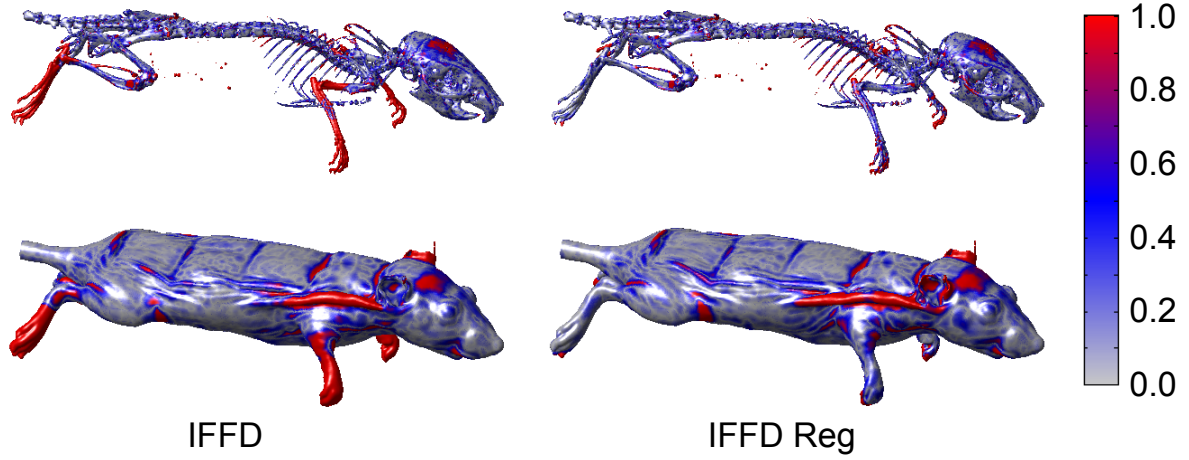
IFFD   IFFD Reg

Figure 6.4: The skeleton and the skin of an animal at baseline with color-coded Euclidean distance to the nearest surface point on the mapped skeleton and skin after registration using IFFD and IFFD Reg respectively. Values (in voxels) are based on one animal.

6.6 Conclusion

We presented a highly robust and accurate approach for registration of articulated objects with application to whole-body MicroCT data of mice. This we obtained by regularizing an intensity-based registration criterion with a distance metric, derived from point correspondence among datasets. We performed registration of in vivo whole-body MicroCT data with high resolution in ≈17 minutes and obtained subvoxel accuracy for the skeleton and the skin. Compared to competing methods, our approach is very time efficient.

7

2D/3D Registration Of MicroCT Data to Multi-View Photographs Based On a 3D Distance Map

Chapter 7

Abstract

In this work we present a method for registration of a CT-derived mouse skin surface to two or more 2D, geometrically calibrated, photographs of the same animal using a similarity transformation model. We show that by using a 3D distance map, which is reconstructed from the animal skin silhouettes in the 2D photographs, and by penalizing large angle differences between distance map gradients and CT-based skin surface normals, we are able to construct a registration criterion that is robust to silhouette outliers and yields accurate results for synthetic and real data (mean skin surface distance $0.12mm$ and $1.35mm$ respectively).

2D/3D Registration Of MicroCT Data to Multiple Photographs

7.1 Introduction

MOLECULAR IMAGING comprises imaging of biological processes at a cellular level and at molecular resolution *noninvasively* and *in vivo* [3]. A broad spectrum of modalities exists for acquiring structural as well as functional data. If modalities are combined, this can results in new insights that could not have been gained by looking at the data separately.

In some cases, it can be useful to register datasets of a different modality *and* dimensionality. An example of this is the registration of 3D anatomical (e.g. CT or MRI) data and multiple 2D views of bioluminescence imaging (BLI) data of small animals. Since BLI images do not show anatomical references, they are usually combined with diffuse light photographs. If these photographs can be registered to 3D CT/MRI data, accurate bioluminescence source localization and quantification becomes possible in 3D using Bioluminescence Tomography, assuming that a 3D map with optical tissue properties can be derived from the CT/MRI dataset [8]. There are traditionally two categories of methods for solving 2D/3D registration problems, dependent on what the registration criterion is based on [157]: feature-based methods [158] and texture(intensity)-based methods [159]. In comparison, feature-based methods are usually faster than texture-based methods but have the disadvantage that the registration accuracy is dependent on the feature selection. To combine high processing speed with high accuracy, gradient-based methods have been proposed more recently [160]. Besides the choice of the registration criterion it is important to choose the registration domain (2D or 3D). While it is relatively easy to generate a 2D representation of a 3D object, the contrary may be complicated since typically the amount of 2D data is very limited. But registration in 3D has the advantage, that the time-consuming, repeated 3D to 2D mapping and the inherent loss of information can be avoided [158].

In recently published work, Markelj *et al.* [160] present an iterative method for rigid registration of a CT or MRI-derived dense gradient field with a sparse 3D gradient field, reconstructed using multiple 2D gradient images (conventional X-ray). The presented results show that their approach combines accuracy with robustness. A drawback of the method is that it needs to search for correspondence between the gradient fields in each iteration, which is time-consuming. Iwashita *et al.* [161] employ a correspondence-free 3D/2D approach for iterative registration of a 3D shape to pre-calculated distance maps, generated using estimated 2D contours of the object. However, the method is carried out in 2D and therefore requires an expensive 3D to 2D mapping in each iteration.

In this work, a 2D/3D registration approach is presented that does *not* need to establish correspondence during registration. On the one hand the method is based on data reduction by extracting features, but on the other hand it integrates feature gradients as well. The contributions of this work are:

- We introduce a registration criterion, based on a 3D distance map, which is reconstructed from a sparse set of 2D images. To ensure robustness and to increase accuracy, it includes angle penalties based on the direction of the gradients in this distance map as well as distance penalties based on the zero level set of the map.
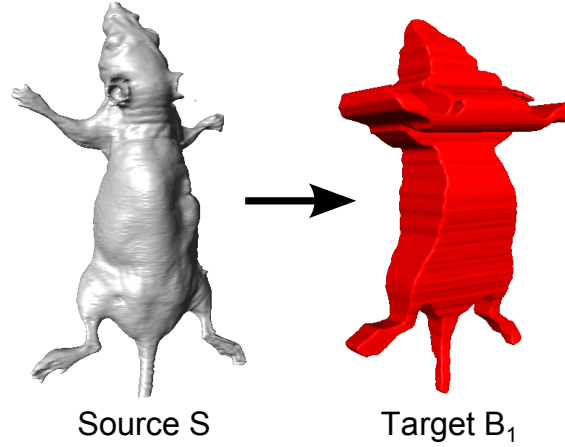
Source S   Target B_1

Figure 7.1: Examples of a CT-derived skin surface (source S) and a surface visualization of a target B_1, derived from two orthogonal photographic views.

- We apply this criterion to register CT-derived mouse skin surfaces to two or more 2D silhouettes of the animal skin using a similarity transformation model.

7.2 Methodology

7.2.1 Shape Representation and transformation type

Since the light photographs only show the animal exterior, the internal structural information in the CT data cannot be exploited for registration. Therefore the skin surface is extracted and represented as a triangular mesh. The target object is not fully determined in 3D because the photographs show projections of the animal and there is only a limited number of photographs available. Therefore an implicit shape representation in 3D is determined based on back-projection of the skin silhouettes that are derived from the 2D images. The target volume B_1 is then defined as the intersection of the back-projected silhouettes. An example of a skin surface extracted from CT and a target volume based on two photographs (top and side view) is given in Fig. 7.1. The size of the entire registration domain B_0, with $B_1 \in B_0$, is determined by the size of the 2D images. Since the CT dataset and the photographs are both acquired from the same animal but the two modalities are not calibrated, a similarity transformation model was chosen to describe the transformation from source to target.

7.2.2 Registration criterion

Given the source skin surface S with n vertices $v \in \mathbb{R}^3$ and the registration domain B_0, an energy function is defined as the sum of squared Euclidean distances (SSD) of all vertices in S to the boundary of the target volume B_1:

2D/3D Registration Of MicroCT Data to Multiple Photographs

$$E_{\text{total}} = \sum_{v=1}^{n} E(v, \Theta)^2 \tag{7.1}$$

$$E(v, \Theta) = DM(B_0, \mathbf{x}) \tag{7.2}$$

$$\mathbf{x} = \lfloor T(v, \Theta) \rceil \tag{7.3}$$

In these equations, T represents the similarity transformation (translation, rotation and isotropic scaling), which is expressed as the parameter vector Θ. $DM(B_0, \mathbf{x})$ contains the Euclidean distance between $\mathbf{x}$ and the boundary of B_1 [162]. For computational purpose, DM was precalculated for all possible (rounded) vertex locations $\mathbf{x}$ by calculating the distance transform of B_0, using Danielsson's method [163]. Note that in the following, the boundary of B_1 is referred to as S_{B1}.

The registration criterion formulated in Eq. 7.1 yields accurate results if the match only receives data support on the tangential lines between S and S_{B1}, and only if the source and the target shape are very similar [160]. However, as depicted in Fig. 7.1, S and S_{B1} differ significantly from each other because one modality may contain information that is not available in the other (Fig. 7.2) and more importantly, because B_1 is based on a very limited number of 2D images. As a result, the minimum SSD yields an overestimation of S, because all vertices on S are considered to contribute equally to the SSD (Figs. 7.3, left and 7.3, middle). To reduce the influence of surface nodes on S, that do not determine the shape of S_{B1}, three steps are implemented:

1. The maximum distance in DM is limited, by introducing a $D_{\max}$ if $|DM(B_0, \mathbf{x})| \geq D_{\max}$:

$$DM_{\text{bound}}(B_0, \mathbf{x}) = max(min(DM, D_{\max}), -D_{\max}) \tag{7.4}$$

A bounded distance map reduces the influence of vertices that cause a large distance error, even if the solution is optimal.

2. Vertices on S that fall outside S_{B1} are penalized by multiplying the distance with a factor $\alpha > 1$:

$$DM_{\text{boundOP}}(B_0, \mathbf{x}) = \begin{cases} \alpha DM_{\text{bound}}, & DM_{\text{bound}} > 0 \\ DM_{\text{bound}}, & DM_{\text{bound}} \leq 0 \end{cases} \tag{7.5}$$

Adding a penalty to all vertices that fall outside B_1 reduces the overestimation of S. Note that these vertices are by definition positioned erroneously, since S_{B1} fully encloses S.

3. The surface normal of S (which closely corresponds to the direction of the steepest gradient in the CT volume) is compared to the distance map gradient (DMG) by adding a penalty if the angle difference r_v between the gradients is above a maximum angle $r_{\max}$ (Fig. 7.3, right):

Figure 7.2: A photograph of a mouse at $0°$ (left), the true silhouette (middle) and a simulated projection (right) based on a CT of the same subject.

$$E_{\text{angle}}(v, \Theta) = \begin{cases} DM_{\text{boundOP}}, & \text{if } r_v < r_{\max} \\ \alpha D_{\max}, & \text{if } r_v >= r_{\max} \end{cases} \tag{7.6}$$

$$r_{\text{v}} = \frac{360}{2\pi} cos^{-1} \left(DMG(B_0, \mathbf{x}) \cdot vertexnormal(T(v, \Theta)) \right) \tag{7.7}$$

By integrating an angle penalty and iteratively decreasing $r_{\max}$, the influence of vertices on S, that are not 'contour'-vertices, is decreased step by step. Indeed, for $r_{\max} \to 0$, only vertices are taken into account, whose surface normal is identical to the distance map gradient (i.e. the tangential lines). In practice however, the final $r_{\max}$ will depend on the number of vertices, i.e. the sampling density of S (Fig. 7.4). The final energy function is:

$$E_{\text{final}} = \sum_{v=1}^{n} E_{\text{angle}}(v, \Theta)^2 \tag{7.8}$$

7.2.3 Minimization of the criterion function

For initialization, the Centers of Gravity (CoGs) of S and B_1 are aligned and an initial scaling parameter is derived from the dimensions of B_1. Subsequently the energy function is minimized using an iterative nonlinear regression method [101].

7.3 Experiments

7.3.1 Validation tests

To validate the proposed method, registration of a CT-derived skin surface to a reconstructed volume was performed. This volume was based either on two and four simulated 2D projections, or two real 2D photographs. For quantitative performance assessment, the transformation parameters (absolute translation of CoG, solid angle, scaling) after registration were compared to the true transformation parameters. In addition, the mean surface distance, and a mean Dice coefficient [164] were calculated between the ground truth and the registered source surface. For the simulated data, the transformation
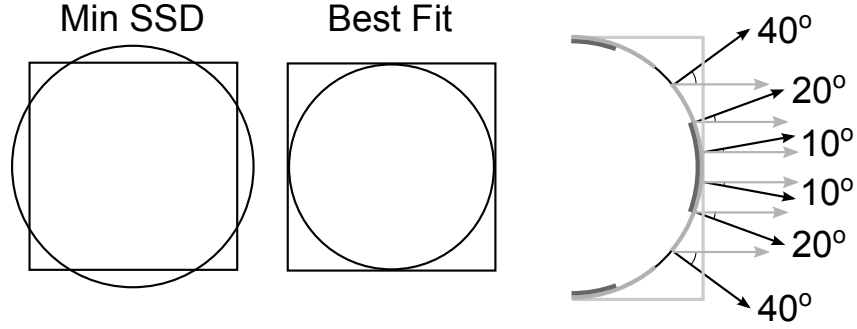
Figure 7.3: Demonstration of the source surface (represented as a circle) overestimation when all surface vertices are weighted equally. In this case, the transformation yielding the minimum SSD (left) does not correspond to the optimum solution (middle). The drawing on the right shows penalized vertices, depending on the angle difference (dark gray = 20°, light gray = 40°) between vertex normals (black) and the DMG (light gray).

Table 7.1: Results of the validation tests (voxel dimension $\hat{=}700\mu m$).

Data	Views	α	Dist. between Skin Surfaces [voxels]	Abs. Dist. of CoGs [voxels]	Scaling Error [%]	Solid Angle Error [degrees]	Dice Coefficient
Synth.	2	1	0.46 ± 0.18	0.64 ± 0.61	0.74 ± 0.54	0.59 ± 0.42	$0.995 \pm 0.75e^{-3}$
Synth.	4	1	0.54 ± 0.08	0.54 ± 0.35	1.33 ± 0.34	0.37 ± 0.27	$0.995 \pm 6.46e^{-4}$
Synth.	2	2.5	$\mathbf{0.17} \pm 0.08$	0.14 ± 0.12	-0.32 ± 0.22	0.60 ± 0.38	$\mathbf{0.998} \pm 5.10e^{-4}$
Synth.	4	2.5	$\mathbf{0.21} \pm 0.04$	0.56 ± 0.16	-0.07 ± 0.19	0.34 ± 0.22	$\mathbf{0.998} \pm 3.68e^{-4}$
Real	2	1	1.98 ± 0.59	5.59 ± 3.74	-1.65 ± 1.53	1.73 ± 1.22	$0.983 \pm 3.00e^{-3}$
Real	2	2.5	1.93 ± 0.66	4.51 ± 3.10	-3.40 ± 1.86	1.66 ± 1.03	$\mathbf{0.984} \pm 3.07e^{-3}$

parameters were known. For the real data, these were calculated, by minimizing the Euclidean distance between two sets of four manually determined anatomical landmarks in the CT data and the photographs respectively. To investigate the effect of α, all experiments were run using $\alpha = 1$ (no penalty) and $\alpha = 2.5$. $r_{\max}$ was first set to 180° (no angle penalty) and then iteratively reduced to 40° and 10°.

7.3.2 Data Acquisition

For validation, 10 mice (Balb/c) were individually placed on a holder. First, a MicroCT dataset was acquired (Skyscan 1178, Kontich, Belgium) *in vivo*, with the resolution $80 \times 80 \times 80 \ \mu m^3$. Subsequently, 2D photographs (top and side view with an angle difference of 90°) were taken from the same animal (Caliper IVIS 3D BLI system, Hopkinton, USA), and subsampled to $700 \times 700 \ \mu m^2$. The usage of the holder prevented posture changes during animal transfer between the modalities. For registration, the skin was segmented semi-automatically from the CT datasets and converted to a triangular mesh (≈ 2000 vertices). The skin boundary in the 2D images was outlined manually in this study (Fig. 7.2, middle). The entire registration domain had the dimensions $52.5 \times 52.5 \times 105mm^3$ ($150 \times 150 \times 300$ voxels). The dimensions of the simulated data as well as the
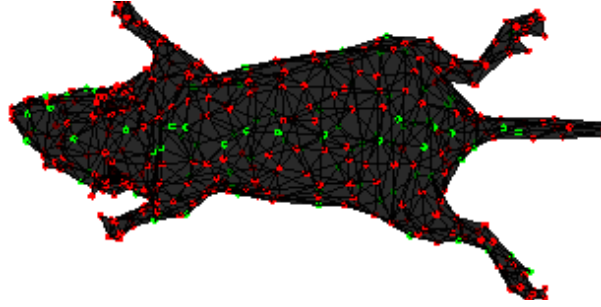
Figure 7.4: The effect of introducing an angle penalty. Vertices on S, that are penalized, are shown in red. Non-penalized vertices are shown in green. In this example, $r_{\max}$ was set to $10°$.

angles were chosen equal to the dimensions and the angles of the real data. For the four view case, two additional angles were used at $\pm 45°$.

7.4 Results and Discussion

A qualitative example of the ground truth as well as the registration result is shown in Fig. 7.5. Table 7.1 presents quantitative results for the experiments using synthetic and real data.

The experiments with the synthetic data reveal good performance of the algorithm. The mean surface error is less than a voxel dimension ($\approx 0.12mm$), the Dice coefficient is very high (0.998) and the transformation parameters could be recovered accurately. In addition, applying a penalty for overestimation ($\alpha = 2.5$) resulted in a better estimation of the scaling parameter than without using the penalty ($\alpha = 1$). Also the registration performance seems to be somewhat better for the 2 view case than for the 4 view case, which is unexpected. However, the variance is smaller in the 4 view case, which indicates that the algorithm performs more robustly, while still yielding accurate results. The other results (e.g. the surface distance) are comparable and clearly below a voxel dimension. This indicates that interpolation effects during generation of the projections at $\pm 45°$ might cause this error.

For the real data, the mean surface distance is less than two voxel dimensions ($\approx 1.35mm$) and the Dice coefficient is very high (0.984). Altogether, the results are less good than using the synthetic data. Reasons might be shape discrepancies (Fig. 7.2 and 7.5) and the non-standardized, manual 2D silhouette and 3D skin surface segmentation. Applying the penalty $\alpha = 2.5$ seems to cause results that are less good for some evaluation measures. This can be explained by the fact that the manually placed anatomical landmarks, which were used to derive the ground truth, have limited accuracy.

7.5 Conclusions and Future Work

We presented a novel method to register a 3D surface to multiple 2D photographs. The chosen registration criterion has proven to yield accurate results using synthetic and

(a)   (b)   (c)   (d)
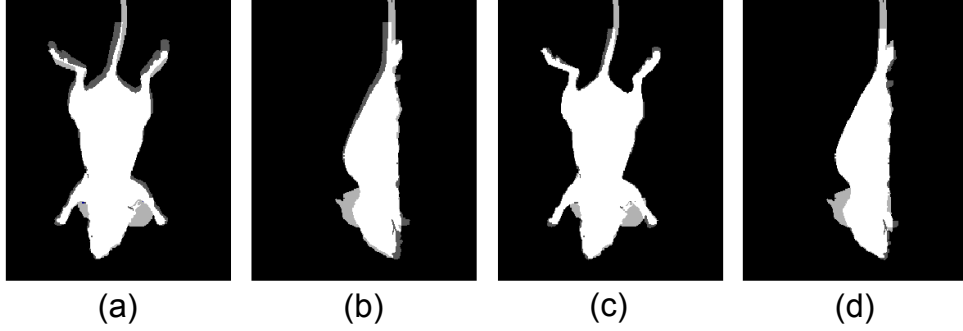
Figure 7.5: Qualitative registration result showing 2D silhouettes (light gray), CT-based projections of a skin surface (dark gray) and their overlap (white) for the ground truth (a, b) and the presented method (c, d). The method is robust against missing registration features (e.g. the ears and part of the tail).

real data and is robust to missing registration features. While the performance was demonstrated using two and four views, more views can be added easily, without adding computational overhead. Since the method does not rely on calculating correspondences, it can be implemented very efficiently.

Because the experiments using more than two (synthetic) views did not yield conclusive results, these experiments will be expanded in the future using real data. Above that, the skin silhouette and the CT skin segmentation should be automated. In addition, we plan to combine the algorithm with a method to approximate major organs from CT data [86] to provide a heterogeneous tissue model for bioluminescence tomography.

8

Summary and Future Work

8.1 Summary and Conclusions

I N THIS THESIS, several strategies are presented that aim to facilitate the analysis and visualization of whole-body in vivo data of small animals. Based on the particular challenges for image processing, when dealing with whole-body follow-up data, we addressed several aspects in this thesis. The developed methods are tailored to handle data of subjects with significantly varying posture and address the large tissue heterogeneity of entire animals. In addition, we aim to compensate for lacking tissue contrast by relying on approximation of organs based on an animal atlas. Beyond that, we provide a solution to automate the combination of multimodality, multidimensional data.

Chapter 1 gives a general introduction to molecular imaging and identifies the challenges for image processing. Furthermore it presents a review of published work that might contribute to face the challenges. It is pointed out that crucial aspects like dealing with large postural variation and tissue heterogeneity as well as handling missing tissue contrast in whole-body data are still problems to be solved and these issues are defined as the goals of this research. The chapter concludes with an outline of the thesis.

Chapter 2 describes the process of constructing articulated skeleton atlases, based on three publicly available whole-body animal atlases (MOBY mouse [59], Digimouse [36], SD Rat [60, 61]). The process includes manual skeleton segmentation, joint localization and definition of anatomically realistic kinematic joint models. The chapter also contains some application examples for the usage of these articulated atlases.

The articulated MOBY atlas is used in Chapter 3 for whole-body segmentation of mice in in vivo MicroCT data. The method is based on registration of the articulated MOBY skeleton to the skeleton extracted from the data. A hierarchical model, combined with restrictions on the amount of DoFs for the registration of the individual bones, renders the method robust to postural variation and pathological bone tissue modifications like osteolytic lesions. Subsequently, the lungs and the skin of the MOBY are registered to the data and major organs are approximated using TPS interpolation. We are able to obtain registration errors (Euclidean surface distances) of less than two voxel dimensions

for the skeleton and the lungs respectively and less than one voxel dimension for the skin. We obtain Dice coefficients of organ volume overlap between manually segmented and interpolated skeleton and organs that vary between 0.47 ± 0.08 for the kidneys and 0.73 ± 0.04 for the brain. Given the very large postural variability of the data that we used for evaluation, the results are very promising and comparable to previously published results. If subvoxel accuracy for the skeleton and the lungs is needed for a specific application, using this method alone does not suffice. However, the results can be used for initialization of a more accurate, intensity-based registration approach. How this can be done is presented in Chapter 6. The most suitable modality for applying the atlas-based skeleton registration presented in this chapter is MicroCT, because the skeleton can easily be extracted from the data. However, the method can be applied to other modalities, such as MicroSPECT [165], as well, as long as an approximation of the skeleton is available.

In Chapter 3 we showed that the skeleton of an animal can be coarsely segmented into individual bones. The true potential of being able to do this automatically is demonstrated in Chapter 4. In this chapter, a method called Articulated Planar Reformation (APR) is presented that maps subvolumes of the original MicroCT dataset to a standardized reference frame. With this framework, a structure of interest, like a particular bone, in multiple MicroCT datasets of different animals or of the same animal at different time points, can easily be related to each other in a side-by-side visualization. Usage of a common reference assures that the structures of interest from all input datasets are aligned to each other. In this way, morphological changes, which can e.g. be disease or treatment related, become apparent. Thus the method allows to easily and automatically navigate through whole-body data and to intuitively assess follow-up datasets. To be able to compare the datasets in a quantitative manner as well, several measurement and visualization strategies are introduced, including bone change visualization, overlays and checkerboard visualizations. Color-coded mapping of the registration error onto the structure of interest allows to judge the reliability of the results. Furthermore, definition of a structure of interest beforehand has the advantage, that not the entire whole-body datasets have to be loaded into memory. This is of great importance especially if multiple time points have to be compared. The data can be loaded with higher resolution because of the restricted Volumes of Interest. The approaches were evaluated by two field scientists who found it very helpful in assessing whole-body follow-up data.

In Chapter 5, the APR framework is extended by a concrete example where accurate quantification is required to follow cancer induced osteolysis over time. First, a structure of interest is selected automatically, from datasets acquired at three different time points, based on the methods presented in the previous chapters. Since the articulated skeleton registration yields a coarse segmentation of the skeleton only (the DoFs of the individual registrations are restricted), we subsequently propose a method for accurate segmentation of different bones. In this chapter, the structure of interest is the tibia and we apply the segmentation method to separate it from the femur. However, the proposed strategy is suitable for segmentation of other bones or the entire skeleton as well. Based on the segmentation of the tibia, the bone volume is followed over time. We compare the automated bone volume measurements to those determined by two human observers. Thorough sta-

tistical analysis reveals that the automated method does not differ significantly from the human observers ($p = .10$). The measurements show high correlation between the observers ($r = 0.9996$) and between the observers and the automated method ($r = 0.9939$ and $r = 0.9937$). In addition, Bland-Altman plots reveal excellent agreement between the observers and the automated method (Interobserver variability: $0.59 \pm 0.64\%$, Obs1 vs. Auto: $0.26 \pm 2.53\%$ and Obs2 vs. Auto: $-0.33 \pm 2.61\%$). Therefore we can conclude that the method can substitute a human observer in monitoring osteolysis over time. Additionally, the chapter presents automated cortical bone thickness measurements. The determined values can be color-coded and mapped onto a surface representation of the tibia to follow thickness variations over time.

It was mentioned above that highly accurate registration of the skeleton cannot be achieved with the articulated skeleton registration presented in Chapter 3. However, intensity-based registration approaches that are capable of achieving high accuracy are not robust enough to deal with data of animals with greatly varying posture. In Chapter 6, we propose to combine the robustness of the articulated registration with the accuracy of intensity-based registration. To this end we formulate the registration between two datasets as an optimization problem. The registration criterion is based on intensity similarity on the one hand and on the Euclidean distance between corresponding sets of landmarks on the other hand. The sets of landmarks in the two datasets are determined by registration of the MOBY atlas to both datasets according to Chapter 6. The optimization can be performed very effectively and fast by the software package `elastix` [154] and we could achieve a significant speedup with an accuracy comparable to previously published work. The combination of the two terms in the optimization outperforms the registrations based on either of the terms used exclusively and we obtain subvoxel accuracy for the skeleton and voxel accuracy for the skin, based on the Euclidean surface to surface distance.

In Chapter 7 we focus on a very common problem in preclinical molecular imaging practice: the fusion of 2D bioluminescence imaging data and 3D MicroCT data. Our approach is to reconstruct an approximation of the animal skin surface in 3D, based on two or more skin silhouettes in 2D photographs, and the calculation of a 3D distance map from the reconstruction. Subsequently, we use the distance map to register a MicroCT-based animal skin surface. Several penalty terms are introduced to deal with the shape differences between the two representations of the animal skin. The method yields subvoxel accuracy for the Euclidean skin surface distance for synthetic data, demonstrating the potential of the method. The experiments for real data are less accurate, with a mean surface distance around two voxel dimensions. We argue that shape differences between the reconstructed skin surface and the MicroCT based skin surfaces are probably the main reason for this. For example the animal ears are clearly visible in the photographs but because they are very thin, they are not present after skin extraction from MicroCT. Despite the limitations, the results are comparable to the results that can be obtained, by registration based on manually determined anatomical landmarks.

Based on the research goals formulated in section. 1.4 and the considerations in this chapter, we think that we achieved our targets to a large extent. The issue of automated analysis of animal data including large postural variability between animals, like follow-

up data, is covered by the articulated registration (Chapter 3) as well as subsequent reformatted visualization and quantification (Chapter 4) and accurate whole-body registration (Chapter 6). Dealing with heterogeneous tissue properties is partly covered since we pay special attention to bone and the lungs in Chapter 3 and by regularization of the registration in Chapter 6. But other tissues (major organs) are treated as being equally stiff during the interpolation and unrealistic deformations may occur. The problem of missing tissue contrast in whole-body data is approached by the strategy to rely on an anatomical animal atlas. We demonstrated this for MicroCT, but approaches for the analysis of data from other modalities could benefit from using the animal atlas as well. Because of the time constraints of this research, the issue of combining data from multiple modalities could only be addressed partly. However, initial results are promising.

8.2 Future work

There are several possibilities for future work, based on the obtained results in this thesis. Regarding the articulated skeleton registration it would be interesting to perform the registration of several bones simultaneously, subject to the motion constraints of the joints by which they are connected. In principle, the sequential nature of the bonewise registration bears the possibility that registration errors are propagated to registrations of distal bones. We compensate for that to a certain extent but it would be interesting to see how simultaneous registration performs in comparison. However, this would require an optimization strategy that can handle many more registration parameters. An improvement would be to include the limbs of the animal as well to derive corresponding landmarks on the skin. Currently, only the skin of the torso is used because the torso contains sufficient corresponding landmarks to define an interpolation of the major organs only. Furthermore, the approximation of the organs could be done in a more elaborate manner instead of taking TPS interpolation. To attach different stiffness properties to each organ, a Finite Element Model of the MOBY atlas could be created. The correspondences on the skeleton, lungs and the skin could be used to derive an estimate of external forces on the atlas, leading to realistic deformations. However, such an approach would be very calculation intensive.

A very interesting experiment would be to use the heterogeneous tissue model after segmentation of an animal with an implanted light source, and assign realistic optical tissue properties to the organs. This may be very useful for light source reconstruction by Bioluminescence Tomography because recently, these approaches were modified for in vivo applications [166, 167]. There is a great need for heterogeneous tissue models to ensure accurate results [90] and it seems, that the boundaries of the organs do not have to be known very accurately in order to still get good results [9].

The common reference of the Articulated Planar Reformation framework is currently tailored for MicroCT data and therefore only defined for the bones. However, one could take an organ approximation and define a VOI around it, similar to the automated scan planning strategy presented in [10]. Doing so for several timepoints it would be possible to map organs to the template as well. However, for MicroCT this is not very meaningful because of the missing contrast.

Summary and Future Work

The accurate bone segmentation technique presented in Chapter 5 was demonstrated for the femur, the tibia and the pelvis. However, the method could be applied to other bones of the skeleton as well, as long as the bone is included in the articulated MOBY skeleton, yielding an accurate whole-body segmentation of the individual bones. Furthermore, the bone volume is currently measured based on thresholded data. However, it might be a better choice to rely on bone mass rather than bone volume in case of bone reformation, based on the grayvalue distribution.

The whole-body registration was evaluated on non-contrast-enhanced MicroCT only. Normalized Cross Correlation is used as the similarity measure but other measures like Mutual Information are applicable as well. Therefore it would be interesting to test the method on contrast-enhanced data, eventually with varying organ contrast between different datasets. The more contrast there is, the better the registration should work.

An interesting extension of the 2D/3D registration method would be to make it independent of an accompanying MicroCT dataset. This could be achieved by relying on an articulated atlas that contains the skeleton and the skin. The skeleton could be articulated, subject to the joint constraints, with a subsequent approximation of the shape of the animal, thus the skin. This could be based on a weighted combination of the bone transformations [92] or paying special attention to the invertibility of the individual transformations [35] or by 'skinning' approaches from the computer animation literature (e.g. [168, 169]). The result would be an approximation of the animal interior, based on several photographs only.

Finally, the mentioned restrictions of the proposed 2D/3D registration method in Chapter 7 should be addressed by automation of the silhouette extraction from the photographs. This should include a priori knowledge of the shape, because not all features visible on the photographs (like the ears) are present in the extracted surface from MicroCT. The combination of such an approach with the heterogeneous tissue model of the animal, would be an important step towards a fully automated Bioluminescence Tomography system for in vivo applications.

References

[1] H. Herschman, "Molecular imaging: looking at problems, seeing solutions," *Science*, vol. 302, no. 5645, p. 605, 2003.

[2] T. F. Massoud and S. S. Gambhir, "Molecular imaging in living subjects: seeing fundamental biological processes in a new light," *Genes Dev*, vol. 17, no. 5, pp. 545–580, Mar 2003.

[3] R. Weissleder and U. Mahmood, "Molecular imaging," *Radiology*, vol. 219, no. 2, pp. 316–333, May 2001.

[4] I. J. Hildebrandt and S. S. Gambhir, "Molecular imaging applications for immunology," *Clin Immunol*, vol. 111, no. 2, pp. 210–224, May 2004.

[5] E. Kaijzel, G. van der Pluijm, and C. Löwik, "Whole-body optical imaging in animal models to assess cancer development and progression," *Clinical Cancer Research*, vol. 13, no. 12, p. 3490, 2007.

[6] E. Kaijzel, T. Snoeks, J. Buijs, G. van der Pluijm, and C. Löwik, "Multimodal imaging and treatment of bone metastasis," *Clinical and Experimental Metastasis*, vol. 26, no. 4, pp. 371–379, 2009.

[7] P. Kok, J. Dijkstra, C. P. Botha, F. H. Post, E. Kaijzel, I. Que, C. W. G. M. Löwik, J. H. C. Reiber, and B. P. F. Lelieveldt, "Integrated visualization of multi-angle bioluminescence imaging and micro CT," in *Proc. of SPIE Medical Imaging*, vol. 6509, 2007, pp. 1–10.

[8] G. Wang, W. Cong, K. Durairaj, X. Qian, H. Shen, P. Sinn, E. Hoffman, G. Mclennan, and M. Henry, "In vivo mouse studies with bioluminescence tomography," *Optics express*, vol. 14, pp. 7801–7809, 2006.

[9] G. Alexandrakis, F. Rannou, and A. Chatziioannou, "Effect of optical property estimation accuracy on tomographic bioluminescence imaging: simulation of a combined optical PET (OPET) system," *Physics in Medicine and Biology*, vol. 51, pp. 2045–2053, 2006.

[10] M. Baiker, B. Vastenhouw, W. Branderhorst, J. H. C. Reiber, F. Beekman, and B. P. F. Lelieveldt, "Atlas-driven scan planning for high-resolution mirco-SPECT data acquisition based on multi-view photographs: a pilot study," in *Proc. of SPIE Medical Imaging*, vol. 7261, 2009, pp. 72 611L–1–72 611L–8.

References

[11] S. M. Janib, A. S. Moses, and J. A. MacKay, "Imaging and drug delivery using theranostic nanoparticles," *Adv Drug Deliv Rev*, vol. 62, no. 11, pp. 1052–1063, Aug 2010.

[12] J. B. A. Maintz and M. A. Viergever, "A survey of medical image registration," *Medical Image Analysis*, vol. 2, no. 1, pp. 1–36, 1998.

[13] D. L. G. Hill, P. G. Batchelor, M. Holden, and D. J. Hawkes, "Medical image registration," *Physics in Medicine and Biology*, vol. 46, no. 3, pp. R1–R45, 2001.

[14] B. Zitova and J. Flusser, "Image registration methods: a survey," *Image and Vision Computing*, vol. 21, no. 11, pp. 977–1000, 2003.

[15] J. P. W. Pluim, J. B. A. Maintz, and M. A. Viergever, "Mutual-information-based registration of medical images: a survey," *IEEE Transactions on Pattern Analysis and Machine Intelligence*, vol. 22, no. 8, pp. 986–1004, Aug 2003.

[16] P. Kok, M. Baiker, E. Hendriks, F. Post, J. Dijkstra, C. Lowik, B. Lelieveldt, and C. Botha, "Articulated Planar Reformation for Change Visualization in Small Animal Imaging," *IEEE Transactions on Visualization and Computer Graphics*, vol. 16, no. 6, pp. 1396–1404, 2010.

[17] M. Baiker, J. Milles, J. Dijkstra, T. D. Henning, A. W. Weber, I. Que, E. L. Kaijzel, C. W. G. M. Löwik, J. H. C. Reiber, and B. P. F. Lelieveldt, "Atlas-based whole-body segmentation of mice from low-contrast Micro-CT data," *Medical Image Analysis*, vol. 14, no. 6, pp. 723–737, Dec 2010.

[18] N. Kovacevic, G. Hamarneh, and M. Henkelman, "Anatomically guided registration of whole body mouse MR images," in *Medical Image Computing and Computer-Assisted Intervention–MICCAI 2003*, 2003, pp. 870–877.

[19] S. Somayajula, A. A. Joshi, and R. M. Leahy, "Mutual information based non-rigid mouse registration using a scale-space approach," in *Proc. IEEE Intl. Symp. on Biomedical Imaging*, 2008, pp. 1147–1150.

[20] A. J. Chaudhari, A. A. Joshi, F. Darvas, and R. M. Leahy, "A method for atlas-based volumetric registration with surface constraints for optical bioluminescence tomography in small animal imaging," in *Proc. of SPIE Medical Imaging*, vol. 6510, 2007, pp. 651 024–1–651 024–10.

[21] A. Joshi, A. Chaudhari, C. Li, J. Dutta, S. Cherry, D. Shattuck, A. Toga, and R. Leahy, "DigiWarp: a method for deformable mouse atlas warping to surface topographic data," *Physics in Medicine and Biology*, vol. 55, p. 6197, 2010.

[22] M. Staring, S. Klein, and J. P. W. Pluim, "Nonrigid registration with tissue-dependent filtering of the deformation field," *Phys. Med. Biol*, vol. 52, no. 23, pp. 6879–6892, 2007.

References

[23] ——, "A Rigidity Penalty Term for Nonrigid Registration," *Medical Physics*, vol. 34, no. 11, pp. 4098 – 4108, November 2007.

[24] D. Xiao, D. Zahra, P. Bourgeat, P. Berghofer, O. A. Tamayo, C. Wimberley, M. Gregoire, and O. Salvado, "An improved 3D shape context registration method for non-rigid surface registration," in *Proc. of SPIE Medical Imaging*, 2010.

[25] X. Li, T. E. Yankeelov, T. E. Peterson, J. C. Gore, and B. M. Dawant, "Constrained non-rigid registration for whole body image registration: method and validation," in *Proc. of SPIE Medical Imaging*, vol. 6512, 2007, pp. 651 202–1–651 202–8.

[26] ——, "Automatic nonrigid registration of whole body CT mice images," *Medical Physics*, vol. 35, no. 4, pp. 1507–1520, 2008.

[27] J. W. Suh, D. Scheinost, D. P. Dione, L. W. Dobrucki, A. J. Sinusas, and X. Papademetris, "A non-rigid registration method for serial lower extremity hybrid SPECT/CT imaging," *Medical Image Analysis*, Sep 2010.

[28] J. F. Krücker, G. L. LeCarpentier, J. B. Fowlkes, and P. L. Carson, "Rapid elastic image registration for 3-D ultrasound," *IEEE Transactions on Medical Imaging*, vol. 21, no. 11, pp. 1384–1394, Nov. 2002.

[29] V. Walimbe and R. Shekhar, "Automatic elastic image registration by interpolation of 3D rotations and translations from discrete rigid-body transformations," *Medical Image Analysis*, vol. 10, no. 6, pp. 899–914, Dec 2006.

[30] O. Commowick, V. Arsigny, A. Isambert, J. Costa, F. Dhermain, F. Bidault, P.-Y. Bondiau, N. Ayache, and G. Malandain, "An efficient locally affine framework for the smooth registration of anatomical structures." *Medical Image Analysis*, vol. 12, no. 4, pp. 427–441, Aug 2008.

[31] V. Arsigny, O. Commowick, N. Ayache, and X. Pennec, "A fast and log-euclidean polyaffine framework for locally linear registration," *J. Math. Imaging Vis.*, vol. 33, no. 2, pp. 222–238, 2009.

[32] M. A. Martín-Fernández, E. Muñoz Moreno, M. Martín-Fernández, and C. Alberola-López, "Articulated registration: elastic registration based on a wire model," in *Proc. of SPIE Medical Imaging*, vol. 5747, 2005, pp. 182–191.

[33] A. du Bois d'Aische, M. De Craene, B. Macq, and S. K. Warfield, "An articulated registration method," in *Proc. IEEE Intl. Conf. on Image Processing*, vol. 1, 2005, pp. 21–24.

[34] M. Van De Giessen, G. Streekstra, S. Strackee, M. Maas, K. Grimbergen, L. Van Vliet, and F. Vos, "Constrained registration of the wrist joint," *IEEE Transactions on Medical Imaging*, vol. 28, no. 12, pp. 1861–1869, 2009.

References

[35] X. Papademetris, D. P. Dione, L. W. Dobrucki, L. Staib, and S. A. J., "Articulated rigid registration for serial lower-limb mouse imaging," in *Medical Image Computing and Computer-Assisted Intervention–MICCAI 2005*, 2005, pp. 919–926.

[36] B. Dogdas, D. Stout, A. F. Chatziioannou, and R. M. Leahy, "Digimouse: a 3D whole body mouse atlas from CT and cryosection data," *Physics in Medicine and Biology*, vol. 52, no. 3, pp. 577–587, 2007.

[37] P. J. Slomka, "Software approach to merging molecular with anatomic information," *J Nucl Med*, vol. 45 Suppl 1, pp. 36S–45S, Jan 2004.

[38] M. Jan, Y. Ni, K. Chen, H. Liang, K. Chuang, and Y. Fu, "A combined micro-PET/CT scanner for small animal imaging," *Nuclear Instruments and Methods in Physics Research Section A: Accelerators, Spectrometers, Detectors and Associated Equipment*, vol. 569, no. 2, pp. 314–318, 2006.

[39] A. Weisenberger, R. Wojcik, E. Bradley, P. Brewer, S. Majewski, J. Qian, A. Ranck, M. Saha, K. Smith, M. Smith *et al.*, "SPECT-CT system for small animal imaging," *IEEE Transactions on Nuclear Science*, vol. 50, no. 1, pp. 74–79, 2003.

[40] S. Maramraju, S. Smith, S. Junnarkar, D. Schulz, S. Stoll, B. Ravindranath, M. Purschke, S. Rescia, S. Southekal, J. Pratte *et al.*, "Small animal simultaneous PET/MRI: initial experiences in a 9.4 T microMRI," *Physics in Medicine and Biology*, vol. 56, p. 2459, 2011.

[41] C. Goetz, E. Breton, P. Choquet, V. Israel-Jost, and A. Constantinesco, "SPECT low-field MRI system for small-animal imaging," *J Nucl Med*, vol. 49, no. 1, pp. 88–93, Jan 2008.

[42] P. B. Zanzonico and S. A. Nehmeh, "Introduction to clinical and laboratory (small-animal) image registration and fusion," in *28th Annual International Conference of the IEEE Engineering in Medicine and Biology Society*, vol. 1, 2006, pp. 1580–1583.

[43] D. Stout and H. Zaidi, "Preclinical multimodality imaging in vivo," *PET Clinics*, vol. 3, no. 3, pp. 251–273, 2008.

[44] D. V. McLaughlin W, "Kodak in vivo imaging system: precise co registration of molecular imaging with anatomical x-ray imaging in animals," Available at: http://www.carestreamhealth.com/WorkArea/showcontent.aspx?id5360874, (Accessed May 3rd, 2011).

[45] A. Douraghy, F. R. Rannou, R. W. Silverman, and A. F. Chatziioannou, "FPGA Electronics for OPET: A Dual-Modality Optical and Positron Emission Tomograph," *IEEE Transactions on Nuclear Science*, vol. 55, no. 5, pp. 2541–2545, 2008.

[46] C. Li, G. Mitchell, J. Dutta, S. Ahn, R. Leahy, and S. Cherry, "A three-dimensional multispectral fluorescence optical tomography imaging system for small animals based on a conical mirror design," *Optics express*, vol. 17, no. 9, p. 7571, 2009.

References

[47] L. Cao, M. Breithaupt, and J. Peter, "Geometrical co-calibration of a tomographic optical system with CT for intrinsically co-registered imaging," *Physics in Medicine and Biology*, vol. 55, p. 1591, 2010.

[48] E. Hillman and A. Moore, "All-optical anatomical co-registration for molecular imaging of small animals using dynamic contrast," *Nature photonics*, vol. 1, no. 9, pp. 526–530, 2007.

[49] P. Chow, D. Stout, E. Komisopoulou, and A. Chatziioannou, "A method of image registration for small animal, multi-modality imaging," *Physics in Medicine and Biology*, vol. 51, p. 379, 2006.

[50] D. Rowland, J. Garbow, R. Laforest, and A. Snyder, "Registration of [18F] FDG microPET and small-animal MRI," *Nuclear medicine and Biology*, vol. 32, no. 6, pp. 567–572, 2005.

[51] B. Fei, H. Wang, R. Muzic Jr, C. Flask, D. Wilson, J. Duerk, D. Feyes, and N. Oleinick, "Deformable and rigid registration of MRI and microPET images for photodynamic therapy of cancer in mice," *Medical Physics*, vol. 33, p. 753, 2006.

[52] F. Beekman and B. Hutton, "Multi-modality imaging on track," *European journal of nuclear medicine and molecular imaging*, vol. 34, no. 9, pp. 1410–1414, 2007.

[53] M. Jan, K. Chuang, G. Chen, Y. Ni, S. Chen, C. Chang, J. Wu, T. Lee, and Y. Fu, "A three-dimensional registration method for automated fusion of micro PET-CT-SPECT whole-body images," *IEEE Transactions on Medical Imaging*, vol. 24, no. 7, pp. 886–893, 2005.

[54] C. Kuo, O. Coquoz, T. Troy, H. Xu, and B. Rice, "Three-dimensional reconstruction of in vivo bioluminescent sources based on multispectral imaging," *Journal of Biomedical Optics*, vol. 12, p. 024007, 2007.

[55] M. Allard, D. Côté, L. Davidson, J. Dazai, and R. Henkelman, "Combined magnetic resonance and bioluminescence imaging of live mice," *Journal of Biomedical Optics*, vol. 12, p. 034018, 2007.

[56] J. Humm, D. Ballon, Y. Hu, S. Ruan, C. Chui, P. Tulipano, A. Erdi, J. Koutcher, K. Zakian, M. Urano *et al.*, "A stereotactic method for the three-dimensional registration of multi-modality biologic images in animals: NMR, PET, histology, and autoradiography," *Medical Physics*, vol. 30, p. 2303, 2003.

[57] Z. Xia, X. Huang, X. Zhou, Y. Sun, V. Ntziachristos, and S. Wong, "Registration of 3-D CT and 2-D flat images of mouse via affine transformation," *IEEE Transactions on Information Technology in Biomedicine*, vol. 12, no. 5, pp. 569–578, 2008.

[58] A. J. Chaudhari, F. Darvas, J. R. Bading, R. A. Moats, P. S. Conti, D. J. Smith, S. R. Cherry, and R. M. Leahy, "Hyperspectral and multispectral bioluminescence optical tomography for small animal imaging," *Phys. Med. Biol*, vol. 50, pp. 5421–5441, 2005.

References

[59] W. P. Segars, B. M. W. Tsui, E. C. Frey, G. A. Johnson, and S. S. Berr, "Development of a 4D digital mouse phantom for molecular imaging research," *Molecular Imaging and Biology*, vol. 6, no. 3, pp. 149–159, 2004.

[60] X. Bai, L. Yu, Q. Liu, J. Zhang, A. Li, D. Han, Q. Luo, and H. Gong, "A high-resolution anatomical rat atlas," *Aging Cell*, vol. 209, no. 5, pp. 707–708, 2006.

[61] L. Wu, G. Zhang, Q. Luo, and Q. Liu, "An image-based rat model for monte carlo organ dose calculations," *Medical Physics*, vol. 35, pp. 3759–3764, 2008.

[62] J. Talairach and P. Tournoux, *Co-planar stereotaxic atlas of the human brain: 3-dimensional proportional system: an approach to cerebral imaging.* Thieme, ISBN-10: 0865772932, 1988.

[63] Visible human project, www.nlm.nih.gov/research/visible/visible_human.html, (Accessed April 26th, 2011).

[64] W. P. Segars, D. S. Lalush, and B. M. W. Tsui, "Modeling respiratory mechanics in the MCAT and spline-based MCAT phantoms," *IEEE Transactions on Nuclear Science*, vol. 48, no. 1, pp. 89–97, 2001.

[65] H. Zaidi and B. M. W. Tsui, "Review of computational anthropomorphic anatomical and physiological models," *Proceedings of the IEEE*, vol. 97, no. 12, pp. 1938–1953, 2009.

[66] A. Toga, E. Santori, R. Hazani, and K. Ambach, "A 3D digital map of rat brain," *Brain research bulletin*, vol. 38, no. 1, pp. 77–85, 1995.

[67] R. Broadwell and R. Bleier, "A cytoarchitectonic atlas of the mouse hypothalamus," *The Journal of Comparative Neurology*, vol. 167, no. 3, pp. 315–339, 1976.

[68] M. R. Celio, P. R. Hof, F. E. Bloom, and W. G. Young, "A computerized stereotaxic atlas of the mouse brain," *Soc. Neurosci. Abst*, vol. 24, pp. 1065–1065, 1998.

[69] A. MacKenzie-Graham, E.-F. Lee, I. D. Dinov, M. Bota, D. W. Shattuck, S. Ruffins, H. Yuan, F. Konstantinidis, A. Pitiot, Y. Ding, G. Hu, R. E. Jacobs, and A. W. Toga, "A multimodal, multidimensional atlas of the C57BL/6J mouse brain," *J Anat*, vol. 204, no. 2, pp. 93–102, Feb 2004.

[70] G. Rosen, A. Williams, J. Capra, M. Connolly, B. Cruz, L. Lu, D. Airey, K. Kulkarni, and R. Williams, "The mouse brain library@ www.mbl.org," in *Int Mouse Genome Conference*, vol. 14, 2000, p. 166.

[71] P. Thompson, M. Mega, K. Narr, E. Sowell, R. Blanton, and A. Toga, "Brain image analysis and atlas construction," in *Handbook of Medical Image Proc. and Analysis*, M. Sonka and J. M. Fitzpatrick, Eds. SPIE, Bellingham, Washington, USA, 2000, ch. 17, pp. 1061 – 1130, ISBN-10: 0819436224.

References

[72] R. M. Brune, J. B. Bard, C. Dubreuil, E. Guest, W. Hill, M. Kaufman, M. Stark, D. Davidson, and R. A. Baldock, "A three-dimensional model of the mouse at embryonic day 9," *Dev Biol*, vol. 216, no. 2, pp. 457–468, Dec 1999.

[73] M. Dhenain, S. W. Ruffins, and R. E. Jacobs, "Three-dimensional digital mouse atlas using high-resolution MRI," *Dev Biol*, vol. 232, no. 2, pp. 458–470, Apr 2001.

[74] P. Santi and J. Nietfeld, "Development of a mouse cochlea database," in *ARO Session K4 Inner Ear Anatomy*, vol. 2, 2002.

[75] http://www.amiravis.com, (Accessed: April 26th, 2011).

[76] M. J. Cook, *Anatomy of the laboratory mouse.* Academic Press Inc.,U.S., ISBN-13: 9780121869502, 1965.

[77] I. Bab, C. Hajbi-Yonissi, Y. Gabet, and R. Müller, *Micro-Tomographic Atlas of the Mouse Skeleton.* Springer, N.Y., USA, ISBN-13: 9780387392547, 2007.

[78] G. Cheers, *Anatomica.* Weltbild Verlag, ISBN-10: 3828920683, 2004.

[79] P. J. Besl and N. D. McKay, "A method for registration of 3D shapes," *IEEE Transactions on Pattern Analysis and Machine Intelligence*, vol. 14, no. 2, pp. 239–256, 1992.

[80] F. L. Bookstein, "Principal warps - Thin-Plate Splines and the decomposition of deformations," *IEEE Transactions on Pattern Analysis and Machine Intelligence*, vol. 11, no. 6, pp. 567–585, 1989.

[81] L. Dice, "Measures of the amount of ecologic association between species," *Ecology*, pp. 297–302, 1945.

[82] A. P. Zijdenbos, B. M. Dawant, and R. A. Margolin, "Morphometric analysis of white-matter lesions in MR-images - method and validation," *IEEE Transactions on Medical Imaging*, vol. 13, no. 4, pp. 716–724, 1994.

[83] M. H. Wildeman, M. Baiker, J. H. C. Reiber, C. W. G. M. Löwik, M. J. T. Reinders, and B. P. F. Lelieveldt, "2D/3D registration of micro-CT data to multi-view photographs based on a 3D distance map," in *Proc. IEEE Intl. Symp. on Biomedical Imaging*, 2009, pp. 987–990.

[84] A. Khmelinskii, M. Baiker, X. J. Chen, J. H. C. Reiber, R. M. Henkelman, and B. P. F. Lelieveldt, "Atlas-based organ & bone approximation for ex-vivo Micro-MRI mouse data: a pilot study," in *Proc. IEEE Intl. Symp. on Biomedical Imaging*, 2010, pp. 1197–1200.

[85] Y.-Q. Zhou, L. Davidson, R. M. Henkelman, B. J. Nieman, F. S. Foster, L. X. Yu, and X. J. Chen, "Ultrasound-guided left-ventricular catheterization: a novel method of whole mouse perfusion for microimaging," *Lab Invest*, vol. 84, no. 3, pp. 385–389, Mar 2004.

References

[86] M. Baiker, J. Dijkstra, I. Que, C. W. G. M. Löwik, J. H. C. Reiber, and B. P. F. Lelieveldt, "Organ approximation in μCT data with low soft tissue contrast using an articulated whole-body atlas," in *Proc. IEEE Intl. Symp. on Biomedical Imaging*, 2008, pp. 1267–1270.

[87] A. Joshi, A. Chaudhari, C. Li, D. Shattuck, J. Dutta, R. Leahy, and A. Toga, "Posture matching and elastic registration of a mouse atlas to surface topography range data," in *Proc. IEEE Intl. Symp. on Biomedical Imaging*. IEEE, 2009, pp. 366–369.

[88] J. R. Landis and G. G. Koch, "The measurement of observer agreement for categorical data." *Biometrics*, vol. 33, no. 1, pp. 159–174, Mar 1977.

[89] J. J. Bartko, "Measurement and reliability: statistical thinking considerations." *Schizophr Bull*, vol. 17, no. 3, pp. 483–489, 1991.

[90] G. Alexandrakis, F. R. Rannou, and A. F. Chatziioannou, "Tomographic bioluminescence imaging by use of a combined optical-PET (OPET) system: a computer simulation feasibility study," *Phys. Med. Biol*, vol. 50, no. 17, pp. 4225–4241, Sep 2005.

[91] X. Zhang, C. Badea, and G. Johnson, "Three-dimensional reconstruction in free-space whole-body fluorescence tomography of mice using optically reconstructed surface and atlas anatomy," *Journal of Biomedical Optics*, vol. 14, p. 064010, 2009.

[92] M. A. Martín-Fernández, R. Cárdenes, E. Muñoz Moreno, R. de Luis-García, M. Martín-Fernández, and C. Alberola-López, "Automated articulated registration of hand radiographs," *Image and vision computing*, vol. 27, no. 8, pp. 1207–1222, 2009.

[93] M. Baiker, J. Milles, A. M. Vossepoel, I. Que, E. L. Kaijzel, C. W. G. M. Löwik, J. H. C. Reiber, J. Dijkstra, and B. P. F. Lelieveldt, "Fully automated whole-body registration in mice using an articulated skeleton atlas," in *Proc. IEEE Intl. Symp. on Biomedical Imaging*, 2007, pp. 728–731.

[94] W. E. Lorensen and H. E. Cline, "Marching cubes: A high resolution 3D surface construction algorithm," in *SIGGRAPH '87: Proceedings of the 14th annual conference on Computer graphics and interactive techniques*, 1987, pp. 163–169.

[95] T. W. Ridler and S. Calvard, "Picture thresholding using an iterative selection method," *IEEE Transactions on Systems, Man, and Cybernetics*, vol. 8, no. 8, pp. 630–632, 1978.

[96] G. W. Zack, W. E. Rogers, and S. A. Latt, "Automatic measurement of sister chromatid exchange frequency," *J. Histochem. Cytochem.*, vol. 25, no. 7, pp. 741–753, 1977.

References

[97] M. Garland and E. Shaffer, "A multiphase approach to efficient surface simplification," in *VIS '02: Proceedings of the conference on Visualization '02.* Washington, DC, USA: IEEE Computer Society, 2002, pp. 117–124.

[98] K. Pearson, "On lines and planes of closest fit to systems of points in space," *Philosophical Magazine*, vol. 2, no. 6, pp. 559–572, 1901.

[99] H. Chui and A. Rangarajan, "A new point matching algorithm for non-rigid registration," *Computer Vision and Image Understanding*, vol. 89, no. 3, pp. 114–141, 2003.

[100] S. Soutiere, C. Tankersley, and W. Mitzner, "Differences in alveolar size in inbred mouse strains," *Respiratory physiology & neurobiology*, vol. 140, no. 3, pp. 283–291, 2004.

[101] T. Coleman and Y. Li, "An interior, trust region approach for nonlinear minimization subject to bounds," *SIAM J Optim*, vol. 6, no. 5, pp. 418–445, 1996.

[102] R. W. Sumner and J. Popović, "Deformation transfer for triangle meshes," in *SIGGRAPH '04: ACM SIGGRAPH 2004 Papers.* New York, NY, USA: ACM Press, 2004, pp. 399–405.

[103] R. Zayer, C. Rössl, Z. Karni, and H.-P. Seidel, "Harmonic guidance for surface deformation," in *The European Association for Computer Graphics 26th Annual Conference : EUROGRAPHICS 2005*, ser. Computer Graphics Forum, M. Alexa and J. Marks, Eds., vol. 24, no. 3, Eurographics. Dublin, Ireland: Blackwell, 2005, pp. 601–609.

[104] S. Belongie, J. Malik, and J. Puzicha, "Shape matching and object recognition using shape contexts," *IEEE Transactions on Pattern Analysis and Machine Intelligence*, vol. 24, no. 4, pp. 509–522, 2002.

[105] A. Elad and R. Kimmel, "On bending invariant signatures for surfaces," *IEEE Transactions on Pattern Analysis and Machine Intelligence*, vol. 25, no. 10, pp. 1285–1295, Oct. 2003.

[106] V. Jain and H. Zhang, "A spectral approach to shape-based retrieval of articulated 3D models," *Comput. Aided Des.*, vol. 39, no. 5, pp. 398–407, 2007.

[107] T. Gatzke and C. Grimm, "Curvature maps for local shape comparison," in *In Shape Modeling International*, 2005, pp. 244–256.

[108] Y. M. Wang, B. S. Peterson, and L. H. Staib, "3D brain surface matching based on geodesics and local geometry," *Computer Vision and Image Understanding*, vol. 89, no. 2-3, pp. 252–271, 2003.

[109] G. Wahba, *Spline models for observational data.* Philadelphia: SIAM, ISBN-13: 9780898712445, 1990.

References

[110] M. Holden, "A review of geometric transformations for nonrigid body registration," *IEEE Transactions on Medical Imaging*, vol. 27, no. 1, pp. 111–128, 2008.

[111] K. Rohr, H. S. Stiehl, R. Sprengel, T. M. Buzug, J. Weese, and M. H. Kuhn, "Landmark-based elastic registration using approximating thin-plate-splines," *IEEE Transactions on Pattern Analysis and Machine Intelligence*, vol. 20, no. 6, pp. 526–534, 2001.

[112] T. Henning, A. W. Weber, J. S. Bauer, R. Meier, J. M. Carlsen, E. J. Sutton, S. Prevrhal, S. I. Ziegler, H. Feussner, H. E. Daldrup-Link, and E. J. Rummeny, "Imaging characteristics of DHOG, a hepatobiliary contrast agent for preclinical microCT in mice," *Acad. Radiol.*, vol. 15, no. 3, pp. 342–349, 2008.

[113] R. Kimmel and J. A. Sethian, "Computing geodesic paths on manifolds," *Proceedings of the National Academy of Sciences of the United States of America*, vol. 95(15), pp. 8431–8435, 1998.

[114] T. Rohlfing, C. Maurer Jr, D. Bluemke, and M. Jacobs, "Volume-preserving non-rigid registration of MR breast images using free-form deformation with an incompressibility constraint," *IEEE Transactions on Medical Imaging*, vol. 22, no. 6, pp. 730–741, 2003.

[115] A. Kanitsar, D. Fleischmann, R. Wegenkittl, P. Felkel, and M. Gröller, "CPR: curved planar reformation," in *VIS '02: Proceedings of the conference on Visualization '02*. IEEE Computer Society, 2002, pp. 37–44.

[116] T. Ochi, K. Shimizu, Y. Yasuhara, T. Shigesawa, T. Mochizuki, and J. Ikezoe, "Curved Planar Reformatted CT Angiography: Usefulness for the Evaluation of Aneurysms at the Carotid Siphon," *AJNR. American journal of neuroradiology*, vol. 20, no. 6, pp. 1025–30, Jun. 1999.

[117] N. Lee and M. Rasch, "Tangential Curved Planar Reformation for Topological and Orientation Invariant Visualization of Vascular Trees," in *28th Annual International Conference of the IEEE Engineering in Medicine and Biology Society*, 2006, pp. 1073–1076.

[118] T. Ropinski, S. Hermann, R. Reich, M. Schäfers, and K. Hinrichs, "Multimodal Vessel Visualization of Mouse Aorta PET/CT Scans," *IEEE Transactions on Visualization and Computer Graphics*, vol. 15, no. 6, pp. 1515—-1522, 2009.

[119] W. Hong, X. Gu, F. Qiu, M. Jin, and A. Kaufman, "Conformal virtual colon flattening," in *Proceedings of the 2006 ACM symposium on Solid and physical modeling*. ACM, 2006, pp. 85–93.

[120] H. Lee, S. Lim, and B. Shin, "Unfolding of virtual endoscopy using ray-template," *Biological and Medical Data Analysis*, pp. 69–77, 2005.

References

[121] D. Williams, S. Grimm, E. Coto, A. Roudsari, and H. Hatzakis, "Volumetric Curved Planar Reformation for Virtual Endoscopy," *IEEE Transactions on Visualization and Computer Graphics*, vol. 14, no. 1, pp. 109–119, januari 2008.

[122] H. Sonnet, S. Carpendale, and T. Strothotte, "Integrating expanding annotations with a 3D explosion probe," in *Proceedings of the working conference on Advanced visual interfaces*. ACM, 2004, pp. 63–70, ISBN-10: 1581138679.

[123] S. Bruckner and M. Gröller, "Exploded Views for Volume Data," *IEEE Transactions on Visualization and Computer Graphics*, vol. 12, no. 5, p. 1077, 2006.

[124] M. McGuffin, L. Tancau, and R. Balakrishnan, "Using Deformations for Browsing Volumetric Data," *In Proceedings of IEEE Visualization*, pp. 401–408, 2003.

[125] N. Gagvani and D. Silver, "Animating Volumetric Models," *Graphical Models*, vol. 63, no. 6, pp. 443 – 458, 2001.

[126] H.-G. Pagendarm and F. H. Post, "Comparative Visualization - Approaches and Examples," in *Visualization in Scientific Computing*, M. Göbel, H. Müller, and B. Urban, Eds. Springer, 1995, pp. 95–108.

[127] D. Schneider, A. Wiebel, H. Carr, M. Hlawitschka, and G. Scheuermann, "Interactive Comparison of Scalar Fields Based on Largest Contours with Applications to Flow Visualization," *IEEE Transactions on Visualization and Computer Graphics*, vol. 14, no. 6, pp. 1475–1482, november 2008.

[128] V. Verma and A. Pang, "Comparative Flow Visualization," *IEEE Transactions on Visualization and Computer Graphics*, pp. 609–624, 2004.

[129] J. Woodring and H.-W. Shen, "Multi-variate, Time Varying, and Comparative Visualization with Contextual Cues," *IEEE Transactions on Visualization and Computer Graphics*, vol. 12, pp. 909–916, 2006.

[130] S. Klein, M. Staring, K. Murphy, M. Viergever, and J. Pluim, "Elastix: A toolbox for intensity-based medical image registration," *IEEE Transactions on Medical Imaging*, vol. 29, no. 1, pp. 196–205, 2010.

[131] H. Levkowitz, *Color Theory and Modeling for Computer Graphics, Visualization and Multimedia Applications*. Springer, ISBN-10: 0792399285, 1997.

[132] A. Kallergi, Y. Bei, P. Kok, J. Dijkstra, J. Abrahams, and F. Verbeek, "Cyttron: A Virtualized Microscope Supporting Image Integration and Knowledge Discovery," *Cell Death and Disease Series (Eds.Backendorf,Noteborn,Tavassoli): Proteins Killing Tumour Cells, ResearchSignPost, Kerala India*, pp. 291–315, 2009.

[133] R. K. Yin, *Case Study Research: Design and Methods*, 4th ed. Sage Publications, ISBN-10:1412960991, 2009.

References

[134] T. Munzner, "A Nested Process Model for Visualization Design and Validation," *IEEE Transactions on Visualization and Computer Graphics*, vol. 15, no. 6, 2009.

[135] H. L. Abrams, R. Spiro, and N. Goldstein, "Metastases in carcinoma; analysis of 1000 autopsied cases," *Cancer*, vol. 3, pp. 74–85, Jan 1950.

[136] T. A. Guise and G. R. Mundy, "Cancer and bone," *Endocr Rev*, vol. 19, no. 1, pp. 18–54, Feb 1998.

[137] G. R. Mundy, "Metastasis to bone: causes, consequences and therapeutic opportunities," *Nat Rev Cancer*, vol. 2, no. 8, pp. 584–593, Aug 2002.

[138] M. Nakai, G. R. Mundy, P. J. Williams, B. Boyce, and T. Yoneda, "A synthetic antagonist to laminin inhibits the formation of osteolytic metastases by human melanoma cells in nude mice," *Cancer Res*, vol. 52, no. 19, pp. 5395–5399, Oct 1992.

[139] A. Sasaki, B. F. Boyce, B. Story, K. R. Wright, M. Chapman, R. Boyce, G. R. Mundy, and T. Yoneda, "Bisphosphonate risedronate reduces metastatic human breast cancer burden in bone in nude mice," *Cancer Res*, vol. 55, no. 16, pp. 3551–3557, Aug 1995.

[140] T. J. A. Snoeks, E. L. Kaijzel, I. Que, I. M. Mol, C. W. G. M. Löwik, and J. Dijkstra, "Normalized volume of interest selection and measurement of bone volume in MicroCT scans," *Bone*, 2011, accepted for publication.

[141] O. Peyruchaud, B. Winding, I. Pécheur, C. M. Serre, P. Delmas, and P. Clézardin, "Early detection of bone metastases in a murine model using fluorescent human breast cancer cells: application to the use of the bisphosphonate zoledronic acid in the treatment of osteolytic lesions," *J Bone Miner Res*, vol. 16, no. 11, pp. 2027–2034, Nov 2001.

[142] A. Wetterwald, G. van der Pluijm, I. Que, B. Sijmons, J. Buijs, M. Karperien, C. W. G. M. Löwik, E. Gautschi, G. N. Thalmann, and M. G. Cecchini, "Optical imaging of cancer metastasis to bone marrow: a mouse model of minimal residual disease." *Am J Pathol*, vol. 160, no. 3, pp. 1143–1153, Mar 2002.

[143] A. Webb, *Statistical pattern recognition.* John Wiley & Sons Inc, ISBN-10:0470845147, 2002.

[144] T. Hildebrand and P. Rüegsegger, "A new method for the model-independent assessment of thickness in three-dimensional images," *Journal of Microscopy*, vol. 185, no. 1, pp. 67–75, 1997.

[145] R. J. van der Geest, P. H. Kitslaar, P. J. H. de Koning, R. van 't Klooster, W. J. Jukema, G. Koning, H. A. Marquering, and J. H. C. Reiber, *Cardiovascular imaging.* Elsevier Saunders, St. Louis, USA, 2011, ch. Advanced three-dimensional postprocessing in computed tomographic and magnetic resonance angiography, pp. 1128–1143, ISBN-13: 978-1416053354.

References

[146] J. M. Bland and D. G. Altman, "Statistical methods for assessing agreement between two methods of clinical measurement." *Lancet*, vol. 1, no. 8476, pp. 307–310, Feb 1986.

[147] A. Field and J. Miles, *Discovering statistics using SAS : (and sex and drugs and rock 'n' roll)*. SAGE Publications, ISBN-13: 9781849200912, 2010.

[148] J. H. Waarsing, J. S. Day, and H. Weinans, "An Improved Segmentation Method for In Vivo CT Imaging," *Journal of Bone and Mineral Research*, vol. 19, no. 10, pp. 1640–1650, 2004.

[149] H. M. Patt and M. A. Maloney, "Bone marrow regeneration after local injury: a review," *Exp Hematol*, vol. 3, no. 2, pp. 135–148, Apr 1975.

[150] I. Bab, D. Gazit, A. Muhlrad, and A. Shteyer, "Regenerating bone marrow produces a potent growth-promoting activity to osteogenic cells." *Endocrinology*, vol. 123, no. 1, pp. 345–352, Jul 1988.

[151] E. Lim, K. Modi, A. Christensen, J. Meganck, S. Oldfield, and N. Zhang, "Monitoring tumor metastases and osteolytic lesions with bioluminescence and micro ct imaging," *Journal of Visualized Experiments*, no. 50, 2011.

[152] W. K. Foster and N. L. Ford, "Investigating the effect of longitudinal micro-CT imaging on tumour growth in mice," *Phys. Med. Biol*, vol. 56, no. 2, pp. 315–326, Jan 2011.

[153] L. C. Johnson, R. W. Johnson, S. A. Munoz, G. R. Mundy, T. E. Peterson, and J. A. Sterling, "Longitudinal live animal micro-CT allows for quantitative analysis of tumor-induced bone destruction," *Bone*, vol. 48, no. 1, pp. 141–151, Jan 2011.

[154] S. Klein, J. Pluim, M. Staring, and M. Viergever, "Adaptive stochastic gradient descent optimisation for image registration," *International journal of computer vision*, vol. 81, no. 3, pp. 227–239, 2009.

[155] D. Rueckert, L. Sonoda, C. Hayes, D. Hill, M. Leach, and D. Hawkes, "Nonrigid registration using free-form deformations: application to breast MR images," *IEEE Transactions on Medical Imaging*, vol. 18, no. 8, pp. 712–721, 1999.

[156] P. Sturm, L. Priese, and H. Wang, "A CSC Based Classification Method for CT Bone Images," in *Proceedings of the Third International Symposium on 3D Data Processing, Visualization and Transmission (3DPVT'06)*. IEEE Computer Society, 2006, pp. 1080–1084.

[157] E. B. van de Kraats, G. P. Penney, D. Tomazevic, T. van Walsum, and W. Niessen, "Standardized Evaluation Methodology for 2-D-3-D Registration," *IEEE Transactions on Medical Imaging*, vol. 24, no. 9, pp. 1177–1189, September 2005.

References

[158] S. Lavallee and R. Szeliski, "Recovering the Position and Orientation of Free-Form Objects from Image Contours Using 3D Distance Maps," *IEEE Transactions on Pattern Analysis and Machine Intelligence*, vol. 17, no. 4, pp. 378–390, 1995.

[159] J. H. Hipwell, G. P. Penney, R. A. McLaughlin, K. Rhode, P. Summers, T. C. Cox, J. V. Byrne, J. A. Noble, and D. J. Hawkes, "Intensity-based 2-D - 3-D registration of cerebral angiograms," *IEEE Transactions on Medical Imaging*, vol. 22, no. 11, pp. 1417–1426, Nov. 2003.

[160] P. Markelj, D. Tomazevic, F. Pernus, and B. Likar, "Robust Gradient-Based 3-D/2-D Registration of CT and MR to X-Ray Images," *IEEE Transactions on Medical Imaging*, vol. 27, no. 12, pp. 1704–1714, Dec. 2008.

[161] Y. Iwashita, R. Kurazume, T. Hasegawa, and K. Hara, "Fast Alignment of 3D Geometrical Models and 2D Color Images Using 2D Distance Maps," in *Fifth International Conference on 3D Digital Imaging and Modeling (3DIM)*. Washington, DC, USA: IEEE Computer Society, 2005, pp. 164–171.

[162] X. Huang, N. Paragios, and D. Metaxas, "Shape registration in implicit spaces using information theory and free form deformations," *IEEE Transactions on Pattern Analysis and Machine Intelligence*, pp. 1303–1318, 2006.

[163] P. Danielsson, "Euclidean distance mapping," *Computer Graphics and image processing*, vol. 14, no. 3, pp. 227–248, 1980.

[164] C. J. van Rijsbergen, *Information Retrieval*. Butterworth, ISBN-13: 9780408709293, 1979.

[165] A. Khmelinskii, M. Baiker, P. Kok, J. de Swart, J. H. C. Reiber, M. de Jong, and B. P. F. Lelieveldt, "Atlas-based articulated skeleton segmentation of μSPECT mouse data," in *Proc. IEEE Intl. Symp. on Biomedical Imaging*, 2011.

[166] Y. Lu, A. Douraghy, H. B. Machado, D. Stout, J. Tian, H. Herschman, and A. F. Chatziioannou, "Spectrally resolved bioluminescence tomography with the third-order simplified spherical harmonics approximation," *Phys. Med. Biol.*, vol. 54, pp. 6477–6493, 2009.

[167] A. Klose, B. Beattie, H. Dehghani, L. Vider, C. Le, V. Ponomarev, and R. Blasberg, "In vivo bioluminescence tomography with a blocking-off finite-difference SP method and MRI/CT coregistration," *Medical Physics*, vol. 37, pp. 329–338, 2010.

[168] D. Jacka, A. Reid, B. Merry, and J. Gain, "A comparison of linear skinning techniques for character animation," in *Proc. 5th int. conf. Comp. graphics, virtual reality, vis. interaction in Africa*. ACM, 2007, pp. 177–186.

[169] L. Kavan, S. Collins, J. Žára, and C. O'Sullivan, "Geometric skinning with approximate dual quaternion blending," *ACM Transactions on Graphics (TOG)*, vol. 27, no. 4, p. 105, 2008.

References

Samenvatting en Aanbevelingen

Samenvatting en Conclusies

I N DIT PROEFSCHRIFT worden verschillende strategieën gepresenteerd met als doel de analyse en de visualisering van in vivo data van kleine proefdieren gemakkelijker te maken. Gebaseerd op de specifieke uitdagingen, die het werken met dit soort data met zich meebrengt, zijn we in dit proefschrift op verschillende aspecten ingegaan. De gepresenteerde methoden zijn gericht op het verwerken van data van lichamen die sterk in postuur verschillen en we houden er rekening mee dat een proefdier uit veel uiteenlopende weefseltypes bestaat. Bovendien richten we ons op het compenseren van ontbrekend weefselcontrast in de data door middel van het benaderen van organen met behulp van een anatomisch model van een proefdier. Verder stellen we een oplossing voor om het combineren van data van meerdere modaliteiten en meerdere dimensies te automatiseren.

Hoofdstuk 1 geeft een algemene introductie tot 'molecular imaging' en benoemt de uitdagingen voor de beeldverwerking. Bovendien wordt een overzicht van gepubliceerd werk gegeven, dat zou kunnen bijdragen aan het oplossen van de uitdagingen. We maken duidelijk dat cruciale aspecten zoals het omgaan met grote verschillen in postuur, de veel uiteenlopende weefseltypes en het ontbreken van weefselcontrast in data van hele lichamen, nog steeds problemen vormen en het bijdragen aan oplossingen voor deze aspecten, wordt als doelstelling van dit proefschrift gedefinieerd. Het hoofdstuk wordt met een overzicht van dit proefschrift afgerond.

Hoofdstuk 2 beschrijft de constructie van gearticuleerde modellen van het bottenstelsel, op basis van openbaar beschikbare modellen van hele lichamen van proefdieren (MOBY mouse [59], Digimouse [36], SD Rat [60, 61]).) Het proces omvat de manuele segmentatie, de lokalisatie van gewrichten en de definitie van anatomisch realistische, kinematische gewricht modellen. Het hoofdstuk bevat ook een aantal voorbeelden van mogelijke toepassingen van de gearticuleerde modellen.

Het gearticuleerde muis model MOBY wordt in Hoofdstuk 3 gebruikt voor het segmenteren van hele muislichamen uit in vivo MicroCT data. De methode is gebaseerd op een registratie van het gearticuleerd MOBY bottenstelsel op het bottenstelsel van de target data. Door de combinatie van een hiërarchisch model en het opleggen van beperkingen van de hoeveelheid vrijheidsgraden die voor de registratie van enkele botten toegestaan zijn, is het mogelijk de methode robuust te maken ten opzichte van posturele verschillen en pathologische veranderingen van botweefsel, veroorzaakt door bijvoorbeeld osteolyse. Daarna worden de longen en de huid van de MOBY op de target data gereg-

Samenvatting en Aanbevelingen

istreerd en de locatie en de grootte van verschillende organen geschat door middel van TPS interpolatie. We zijn in staat om een registratiefout (Euclidische afstand tussen oppervlakten) onder de twee voxeldimensies voor het bottenstelsel en de longen en onder één voxeldimensie voor de huid te bereiken. De Dice coëfficiënten, die een indicatie van de orgaanoverlap geven, variëren tussen 0.47 ± 0.08 voor de nieren en 0.73 ± 0.04 voor het brein. Gegeven de grote posturele verschillen, die in de data aanwezig zijn, zijn de verkregen resultaten veelbelovend en vergelijkbaar met eerder gepubliceerde resultaten. Indien subvoxel nauwkeurigheid voor het bottenstelsel en de huid noodzakelijk zijn voor een bepaalde toepassing, zijn de behaalde resultaten niet voldoende nauwkeurig. Maar het registratieresultaat kan worden gebruikt om een nauwkeurigere intensiteitgebaseerde methode te initialiseren. Dit wordt in Hoofdstuk 6 gepresenteerd. De meest geschikte modaliteit voor het toepassen van de gearticuleerde registratie methode, die in dit hoofdstuk wordt besproken, is MicroCT, omdat het bottenstelsel relatief gemakkelijk uit de data kan worden gesegmenteerd. De methode kan echter ook op data van andere modaliteiten zoals MicroSPECT [165] worden toegepast, indien een benadering van het bottenstelsel kan worden bepaald.

In Hoofdstuk 3 lieten we zien, hoe het bottenstelsel van een muis in individuele botten kan worden gesegmenteerd. De echte toegevoegde waarde, om dit geautomatiseerd te doen, wordt in Hoofdstuk 4 duidelijk gemaakt. In dit hoofdstuk wordt een methode met de naam 'Articulated Planar Reformation' voorgesteld, die subvolumes vanuit de originele MicroCT data naar een gestandaardiseerd referentiestelsel verplaatst. Met dit raamwerk kan een bepaalde structuur, zoals een specifiek bot, vanuit verschillende MicroCT datasets van verschillende proefdieren of hetzelfde proefdier op verschillende tijdpunten, gemakkelijk worden vergeleken door middel van een side-by-side visualisatie. Het gebruik van een gestandaardiseerd referentiestelsel waarborgt dat een specifieke structuur in alle datasets aan elkaar uitgelijnd is. Dusdanig worden morfologische verschillen, die bijvoorbeeld uit een bepaalde ziekte of een bepaalde behandeling voortkomen, onmiddellijk duidelijk. Zodoende is het met deze methode mogelijk, om gemakkelijk en automatisch door datasets van hele lichamen te navigeren, en follow-up datasets op een intuïtieve manier te onderzoeken. Om de datasets bovendien ook kwantitatief te kunnen vergelijken, worden meerdere meet- en visualisatiestrategieën gepresenteerd, onder andere een visualisatie van bot verandering, een overlay visualisatie en een checkerboard visualisatie. Een representatie van de registratie fout in een visualisatie van een bepaalde structuur, door middel van kleuren, maakt het mogelijk om de betrouwbaarheid van de resultaten in te schatten. Verder heeft het focussen op een bepaalde structuur in een dataset van een heel lichaam het voordeel, dat niet de hele data in het werkgeheugen moet worden geladen. Dit is een heel belangrijk aspect, vooral als meerdere tijdpunten moeten worden vergeleken. De datasets kunnen dus met hogere resolutie worden geopend, omdat de Volume of Interest erg beperkt kan worden. De methodes werden geëvalueerd door twee experts uit het vak en deze vonden ze erg nuttig in het onderzoeken van follow-up data van hele muislichamen.

In Hoofdstuk 5 wordt het APR raamwerk uitgebreid door een concreet voorbeeld, waar nauwkeurige kwantificatie nodig is voor het volgen van door kanker veroorzaakte osteolyse over de tijd. Eerst wordt een bepaalde structuur automatisch gesegmenteerd uit datasets

Samenvatting en Aanbevelingen

die op drie verschillende tijdpunten zijn opgenomen, door middel van de methodes die in de voorafgaande hoofdstukken zijn geïntroduceerd. Omdat de gearticuleerde registratie van het bottenstelsel segmentaties van enkele botten met beperkte nauwkeurigheid oplevert (de vrijheidsgraden van de individuele registraties zijn beperkt), stellen we in het vervolg een methode voor om verschillende botten met hoge nauwkeurigheid te segmenteren. In dit hoofdstuk gaat het om de tibia, die we van de femur scheiden. Echter kan onze benadering ook voor een segmentatie van andere botten of het hele bottenstelsel worden gebruikt. Gebaseerd op de segmentatie van de tibia, meten we het bot volume op verschillende tijdpunten en vergelijken de meetwaarden van de geautomatiseerde methode met meetwaarden, die door twee experts zijn bepaald. Uit een grondige statistische analyse blijkt dat de automatische methode niet significant verschilt van de twee experts ($p = .10$). De meetwaarden van de twee experts hebben een hoge correlatie ($r = 0.9996$), net zoals de meetwaarden van de experts ten opzichte van de geautomatiseerde methode ($r = 0.9939$ en $r = 0.9937$). Bovendien laten Bland-Altman plots een uitstekende overeenkomst tussen de metingen van de experts en de geautomatiseerde methode zien (Interobserver variabiliteit: $0.59 \pm 0.64\%$, Obs1 vs. Auto: $0.26 \pm 2.53\%$ en Obs2 vs. Auto: $-0.33 \pm 2.61\%$). Dusdanig kunnen we concluderen dat de methode een expert kan vervangen als het om het volgen van osteolyse over de tijd gaat. Verder wordt in het hoofdstuk een automatische methode gepresenteerd om de corticale bot dikte te bepalen. De gemeten waarden kunnen in een visualisatie van de oppervlakte van de tibia worden gebruikt door deze aan verschillende kleuren te koppelen. Daarmee wordt het volgen van bot dikte variaties over de tijd een heel stuk makkelijker gemaakt.

Zoals eerder vermeld kan een heel nauwkeurige segmentatie van het bottenstelsel niet met de gearticuleerde bottenstelsel registratie methode uit Hoofdstuk 3 bereikt worden. Echter zijn intensiteit-gebaseerde benaderingen voor registratie, waarmee in principe een grote nauwkeurigheid kan worden bereikt, niet voldoende robuust om met data van proefdieren met grote posturele verschillen om te kunnen gaan. In Hoofdstuk 6 stellen we voor om de robuustheid van de gearticuleerde registratie met de nauwkeurigheid van een intensiteit-gebaseerde registratie te combineren. Om dit te bereiken, beschouwen we de registratie tussen twee datasets als een optimalisatieprobleem. Het registratie criterium is aan de ene kant gebaseerd op de overeenkomst van de intensiteit en aan de andere kant op de Euclidische afstand tussen corresponderende landmark sets. Deze zijn bepaald in de twee datasets door de registratie van het MOBY muismodel op de twee datasets zoals beschreven in Hoofdstuk 6. De optimalisatie kan heel efficiënt en snel worden doorgevoerd met behulp van de `elastix` [154] software. We waren daarmee in staat om een even goede nauwkeurigheid te behalen als in eerder gepubliceerd werk, maar in significant kortere tijd. De combinatie van de twee termen in de optimalisatie leidt in vergelijking tot het gebruik van alleen één van de twee termen apart tot een beter resultaat en we zijn in staat om subvoxel nauwkeurigheid voor het bottenstelsel en voxel nauwkeurigheid voor de huid, gemeten op basis van de Euclidische afstand tussen twee oppervlakten, te behalen.

In Hoofdstuk 7 besteden we aandacht aan een veel voorkomend probleem in de praktijk van de preklinische moleculaire beeldvorming: de fusie van 2D bioluminescence imaging data en 3D MicroCT data. Onze strategie is om eerst een benadering van de huid van een

proefdier in 3D te reconstrueren, op basis van twee of meerdere silhouetten van de huid op 2D foto's, en dan een 3D distance map te berekenen. Daarop volgend gebruiken we deze distance map om de uit de MicroCT data gesegmenteerde huid van het proefdier te registreren. Meerdere penalty termen worden geïntroduceerd om met de vorm verschillen tussen de twee representaties van de huid om te kunnen gaan. Met deze methode is het mogelijk om subvoxel nauwkeurigheid voor synthetische data te bereiken (Euclidische afstand tussen de huidoppervlakten), waardoor het potentieel van de methode duidelijk wordt. De resultaten van experimenten met echte data zijn met een gemiddelde afstand tussen de oppervlakten van rond de twee voxels minder nauwkeurig. We denken dat dit voornamelijk met de verschillen tussen de twee representaties van de huid te maken heeft. De oren van een proefdier zijn bijvoorbeeld duidelijk op de 2D foto's te zien, maar omdat ze erg dun zijn, is het erg lastig om ze uit de MicroCT dataset te segmenteren. Ondanks de beperkingen zijn de behaalde resultaten vergelijkbaar met de resultaten die door registraties op basis van handmatig geselecteerde landmarks bereikt kunnen worden.

Gebaseerd op de focus van dit onderzoek, die in Sec. 1.4 geformuleerd is, en de observaties in dit hoofdstuk denken we dat we onze doelen in grote mate bereikt hebben. De automatische analyse van datasets van proefdieren met grote posturele verschillen, die bijvoorbeeld in follow-up studies optreden, wordt mogelijk gemaakt door de gearticuleerde registratie (Hoofdstuk 3), de daarop volgende verplaatsing naar een gestandaardiseerd referentie stelsel voor visualisatie en kwantificatie (Hoofdstuk 4) en de nauwkeurige registratie van het hele lichaam (Hoofdstuk 6). Met verschillende weefseltypes wordt gedeeltelijk rekening gehouden, omdat we in Hoofdstuk 3 specifiek eerst het bottenstelsel en dan de longen registreren en door de regularisatie van de registratie in Hoofdstuk 6. Tussen andere organen worden echter door de interpolatie van het zachte weefsel geen verschil gemaakt. Niet realistische deformaties kunnen het gevolg hiervan zijn. Het probleem van het ontbrekende weefselcontrast in datasets van hele lichamen wordt benaderd door het gebruiken van een anatomisch model van het proefdier. We hebben deze oplossing gepresenteerd voor MicroCT data, maar benaderingen voor de analyse voor datasets van andere modaliteiten zouden eveneens baat kunnen hebben van het gebruik van een model. Vanwege een gebrek aan tijd voor dit onderzoek, kon het probleem van het combineren van data van meerdere modaliteiten maar gedeeltelijk worden behandeld. De initiële resultaten zijn echter veelbelovend.

Aanbevelingen

Er zijn meerdere mogelijkheden voor toekomstig werk op basis van de resultaten in dit proefschrift. Wat de gearticuleerde registratie van het bottenstelsel betreft, zou het interessant zijn om de registratie van meerdere botten tegelijkertijd door te voeren, waarbij met de beperkingen van het gewricht types waarmee deze met elkaar verbonden zijn rekening gehouden moet worden. In principe houd de sequentiële bot voor bot registratie methode de mogelijkheid in dat registratiefouten doorgeschoven worden. Wel houden we hiermee rekening, maar het zou interessant zijn om te zien hoe een simultane registratie van botten werkt, vergeleken met onze methode. Echter is voor deze optie een optimalisatie strategie nodig, die met veel meer registratieparameters tegelijkertijd om kan gaan

Samenvatting en Aanbevelingen

als die die wij gebruiken. Een verbetering van de methode zou het meenemen van corresponderende landmarks op de ledematen zijn, voor de registratie van de huid. Op dit moment worden alleen corresponderende landmarks op de huid van de romp meegenomen, omdat de locaties en de afmetingen van de organen niet of nauwelijks van de positie van de ledematen afhangt. Verder zouden de locaties en de afmetingen van de organen op een geavanceerdere manier kunnen worden geschat als dit met TPS interpolatie mogelijk is. Om verschillende stijfheden aan verschillende organen toe te kennen, zou een Finite Element Model van het MOBY model kunnen worden gemaakt. De correspondenties op het bottenstelsel, de longen en de huid zouden dan ervoor kunnen worden gebruikt een inschatting van externe krachten op het lichaam te maken en dan de organen op een realistische manier te deformeren. Een dusdanige methode zou echter vrij rekenintensief zijn.

Een erg interessant experiment zou zijn om aan een heterogeen weefselmodel na de segmentatie van een proefdier met een geïmplanteerde lichtbron, realistische optische weefseleigenschappen toe te kennen. Dit zou heel nuttig kunnen zijn voor het reconstrueren van de lichtbron door middel van Bioluminescence Tomography omdat deze methodes recent voor in vivo toepassingen beschikbaar zijn gekomen [166, 167]. Er bestaat een grote behoefte aan heterogene weefselmodellen, om nauwkeurige resultaten te kunnen bereiken [90] en het lijkt erop dat de begrenzingen van de organen niet heel nauwkeurig bekend hoeven zijn om alsnog goede resultaten te verkrijgen [9].

Het gestandaardiseerde referentiestelsel van het 'Articulated Planar Reformation' raamwerk is op dit moment toegepast op MicroCT data en dus gespecialiseerd op bot. Maar in feite zou het mogelijk zijn om op basis van een benadering van een orgaan een Volume of Interest om dat orgaan te genereren op een manier die lijkt op automatische scan planning strategieën zoals bijvoorbeeld voorgesteld in [10]. Door dit voor meerdere tijdpunten te doen zou het mogelijk zijn om ook organen naar het gestandaardiseerde referentiestelsel te verplaatsen. Dit zou echter voor MicroCT niet veel opleveren, door het ontbrekende contrast van zacht weefsel.

De nauwkeurige botsegmentatiemethode uit Hoofdstuk 5 werd toegepast op de tibia, de femur en de pelvis. De methode zou echter ook op de andere botten van het bottenstelsel kunnen worden toegepast, mits het bot in het gearticuleerde MOBY model is opgenomen. Dit zou een nauwkeurige botsegmentatie van het hele lichaam opleveren. Verder wordt het botvolume tegenwoordig gemeten op basis van thresholded data. Het zou echter een betere keuze kunnen zijn om de botmassa door middel van de grijswaardeverdeling in de data te meten in plaats van het botvolume in het geval van osteolyse.

De registratie van het hele lichaam werd uitsluitend op niet-contrast-verbeterde MicroCT data geëvalueerd. De overeenkomst van de intensiteit wordt gemeten met Normalized Cross Correlation, maar bijvoorbeeld Mutual Information zou ook kunnen worden gebruikt. Daarom zou het interessant zijn om de methode met contrast-verbeterd MicroCT data, die verschillende orgaan contrast kan bevatten, te testen. Hoe meer contrast beschikbaar is, hoe beter zou de methode moeten werken.

Een interessante uitbreiding van de 2D/3D registratie methode zou zijn om ze onafhankelijk van de MicroCT dataset te maken. Dit zou kunnen worden gedaan door een gearticuleerd muismodel met het bottenstelsel en de huid te gebruiken. Het bottens-

telsel zou kunnen worden gearticuleerd, waarbij met de beperkingen door de gewrichten rekening wordt gehouden, en daarop volgend zou de vorm van het lichaam van het proefdier, dus de huid, kunnen worden geschat. Dit zou bijvoorbeeld kunnen worden gedaan door een gewogen combinatie van de bot transformaties [92], door bijzonder aandacht te schenken aan de omkeerbaarheid van de transformaties [35] of door 'skinning' technieken uit de computer animatie literatuur (bijvoorbeeld [168,169]) te gebruiken. Het resultaat zou een benadering van de interne structuur van het proefdier zijn, die puur op basis van twee of meerdere foto's van het proefdier zijn bepaald.

Ten slotte zouden de genoemde beperkingen van de 2D/3D registratie methode uit Hoofdstuk 7 moeten worden aangepakt door de segmentatie van de silhouet in de 2D foto's te automatiseren. Aan een dergelijke benadering zou a priori informatie van de vorm van het proefdier moeten worden toegevoegd, omdat de huidoppervlakte van de MicroCT data niet alles bevat dat op de foto's te zien is (zoals de oren). De combinatie van geautomatiseerde silhouetextractie en een heterogeen weefselmodel van het proefdier zou een belangrijke stap zijn op de weg naar een volledig geautomatiseerd Bioluminescence Tomography systeem voor in vivo applicaties.

Samenvatting en Aanbevelingen

Publications

Publications in international journals

- **Martin Baiker and Thomas J. A. Snoeks**, Eric L. Kaijzel, Ivo Que, Jouke Dijkstra, Boudewijn P. F. Lelieveldt, Clemens W. G. M. Löwik, "Automated segmentation and bone volume and thickness measurements in small animal whole-body MicroCT data", *Accepted for publication in Molecular Imaging and Biology.*

- Peter Kok, **Martin Baiker**, Emile A. Hendriks, Frits H. Post, Jouke Dijkstra, Clemens W. G. M. Löwik, Boudewijn P. F. Lelieveldt, Charl P. Botha, "Articulated Planar Reformation for Change Visualization in Small Animal Imaging", *IEEE Transactions on Visualization and Computer Graphics, 2010, 16(6):1396-1404.*

- **Artem Khmelinskii and Martin Baiker**, Eric Kaijzel, Josette Chen, Johan H.C. Reiber, Boudewijn P.F. Lelieveldt, "Articulated Whole-Body Atlases for Small Animal Image Analysis: Construction and Applications", *Molecular Imaging and Biology, 2011, 13(5):898-910.*

- **Martin Baiker**, Julien Milles, Jouke Dijkstra, Tobias D. Henning, Axel W. Weber, Ivo Que, Eric L. Kaijzel, Clemens W. G. M. Löwik, Johan H. C. Reiber, Boudewijn P. F. Lelieveldt, "Atlas-Based Whole-Body Segmentation of Mice from Low-Contrast Micro-CT Data", *Medical Image Analysis, 2010, 14(6):723-737.*

Contributions to peer reviewed conferences

- **Martin Baiker**, Marius Staring Clemens W. G. M. Löwik, Johan H. C. Reiber, Boudewijn P. F. Lelieveldt, "Automated Registration of Whole-Body Follow-Up MicroCT Data of Mice (poster)", *In: Fichtinger, G., Martel, A., Peters, T. (eds.): MICCAI 2011, Part II, LNCS, vol. 6892, pp. 516-523. Springer, Heidelberg.*

- Artem Khmelinskii, **Martin Baiker**, Peter Kok, Jan de Swart, Johan H. C. Reiber, Marion de Jong, Boudewijn P. F. Lelieveldt, "Atlas-based articulated skeleton segmentation of μSPECT mouse data (oral)", *Proc. IEEE Intl. Symp. on Biomedical Imaging, 2011.*

- Artem Khmelinskii, **Martin Baiker**, X. Josette Chen, Johan H. C. Reiber, Mark R. Henkelman, Boudewijn P. F. Lelieveldt, "Atlas-based organ & bone approximation

for ex-vivo Micro-MRI mouse data: a pilot study (poster)", *Proc. IEEE Intl. Symp. on Biomedical Imaging, 2010, pp. 1197-1200.*

- Martin H. Wildeman, **Martin Baiker**, Johan H. C. Reiber, Clemens W. G. M. Lẅik, Marcel J. T. Reinders, Boudewijn P. F. Lelieveldt, "2D/3D Registration Of Micro-CT Data to Multi-View Photographs Based On a 3D Distance Map (poster)", *Proc. IEEE Intl. Symp. on Biomedical Imaging, 2009, pp. 987-990.*

- **Martin Baiker**, Jouke Dijkstra, Ivo Que, Clemens W. G. M. Löwik, Johan H. C. Reiber, Boudewijn P. F. Lelieveldt, "Organ approximation in μCT data with low soft tissue contrast using an articulated whole-body atlas (oral)", *Proc. IEEE Intl. Symp. on Biomedical Imaging, 2008, pp. 1267-1270.*

- **Martin Baiker**, Julien Milles, Albert M. Vossepoel, Ivo Que, Eric L. Kaijzel, Clemens W. G. M. Löwik, Johan H. C. Reiber, Jouke Dijkstra, Boudewijn P. F. Lelieveldt, "Fully automated whole-body registration in mice using an articulated skeleton atlas (poster)", *Proc. IEEE Intl. Symp. on Biomedical Imaging, 2007, pp. 728-731.*

Other conference contributions

- **Martin Baiker**, Brendan Vastenhouw, Woutjan Branderhorst, Johan H. C. Reiber, Freek J. Beekman, Boudewijn P. F. Lelieveldt, "Atlas-Driven Scan Planning for High-Resolution Mirco-SPECT Data Acquisition based on Multi-View Photographs: a Pilot Study (oral)", *Proc. SPIE Medical Imaging, 2009, 7261, 1L, pp. 1-8.*

Book chapters and other publications

- Eric L. Kaijzel, Thomas J. A. Snoeks, Ivo Que, **Martin Baiker**, Peter Kok, Boudewijn P. F. Lelieveldt, Clemens W. G. M. Löwik, ""In vivo" Molecular Imaging", *in Chemiluminescence and Bioluminescence: Past, Present and Future, Ed. A. Roda, Royal Society of Chemistry 2011, ISBN-13: 978-1847558121.*

- **Martin Baiker**, Jouke Dijkstra, Julien Milles, Clemens W. G. M. Löwik, Boudewijn P. F. Lelieveldt, "Atlas-based whole-body registration in mice", *in Handbook of Biomedical Imaging, Eds. N. Paragios, J. Duncan, N. Ayache, Springer N.Y. 2012, ISBN-13: 978-0387097480, in press.*

- Brendan Vastenhouw, Woutjan Branderhorst, Frans van der Have, **Martin Baiker**, Boudewijn P. F. Lelieveldt, Freek J. Beekman, "Field-of-view definition for focusing pinhole SPECT using optical cameras", *in Simulation, construction and application of focused pinhole small animal SPECT, PhD Thesis, Utrecht University, 2008, ISBN-13: 978-9039349410.*

Abstracts

- **Martin Baiker**, Thomas J. A. Snoeks, Eric L. Kaijzel, Ivo Que, Jouke Dijkstra, Boudewijn P. F. Lelieveldt, Clemens W. G. M. Löwik, "Automated Segmentation and Bone Volume and Thickness Measurement in Small Animal Whole-Body MicroCT Data (oral)", *World Molecular Imaging Congress 2011, San Diego, USA.*

- Thomas J. A. Snoeks, **Martin Baiker**, Eric L. Kaijzel, Boudewijn P. F. Lelieveldt, Clemens W. G. M. Löwik, "Automated segmentation and bone volume and thickness measurements in small animal whole-body micro-CT scans (poster)", *European Molecular Imaging Meeting 2011, Leiden, The Netherlands.*

- **Martin Baiker**, Jouke Dijkstra, Ivo Que, Clemens W. G. M. Löwik, Johan H. C. Reiber, Boudewijn P. F. Lelieveldt, "Organ approximation in μCT data with low soft tissue contrast using an articulated whole-body atlas (oral)", *Imagination 2008, Leiden University Medical Center, Leiden, The Netherlands.*

- **Martin Baiker**, Jouke Dijkstra, Ivo Que, Clemens W. G. M. Löwik, Johan H. C. Reiber, Boudewijn P. F. Lelieveldt, "Organ approximation in μCT data with low soft tissue contrast using an articulated whole-body atlas (oral)", *NVPHBV Meeting 2008, Eindhoven, The Netherlands.*

- **Martin Baiker**, Jouke Dijkstra, Ivo Que, Clemens W. G. M. Löwik, Johan H. C. Reiber, Boudewijn P. F. Lelieveldt, "Organ approximation in μCT data with low soft tissue contrast using an articulated whole-body atlas (poster)", *World Molecular Imaging Congress 2008, Nice, France.*

- **Martin Baiker**, Julien Milles, Albert Vossepoel, Ivo Que, Eric L. Kaijzel, Clemens W. G. M. Löwik, Johan H. C. Reiber, Boudewijn P. F. Lelieveldt, Jouke Dijkstra, "INTEGRIM: a Tool for Matching, Interpretation and Visualization for Fused Micro-CT and BLI imaging of Multiple Animals and Time Points (poster)", *Joint Molecular Imaging Conference 2007, Providence, USA.*

Acknowledgements

From May 2007 to April 2011 I was working as a PhD candidate at the LKEB, the Laboratorium voor Klinische en Experimentele Beeldverwerking (Division of Image Processing), in the Section of Knowledge Guided Image Processing, under the supervision of Prof. Dr. Ir. B.P.F. Lelieveldt, Prof. Dr. C.W.G.M. Löwik and Prof. Dr. Ir. J.H.C. Reiber, at the Leiden University Medical Center (LUMC) in Leiden, the Netherlands. This thesis presents the results of the research conducted during this period.

First of all I would like to thank my colleague Vikas who made clear to me, what really counts in a thesis. Once I told him that I had already finished all the chapters and that only the 'Acknowledgements' and the cover were missing. He said, with a grin on his face, that I had done a nice job but that in fact the most important part of the thesis, which would be read by everybody, was still missing. Indeed, going for a PhD means working for 99.9% of the time to produce output that will be read by 0.1% of the people that get the thesis and vice versa: an economic disaster! (Note that I used 99.9% only for illustrative purposes. It didn't actually take me 1.46 days to write this section.) =:-)

Nevertheless, I enjoyed the years that I spent at the LKEB and am grateful for all the help I got from my colleagues, the facilities and last but not least the in my opinion best office of the LKEB. All this together made it possible to successfully finish my conquest of the holy grail. More specifically I would like to thank Avan Suinesiaputra for fruitful work-related discussions, Marius Staring, image registration guru and very patient `elastix` helpdesk as well as Martin Wildeman, who was working very hard for his MSc project and therefore provided the basis for Chapter 7 of this thesis. Above that I would like to thank all co-authors of the presented work for their valuable contributions. Bertie, Els and Michèle, administrative, hard- and software issues never remained unsolved for long and I am grateful that you were always ready and helpful. My thanks also go to the people of the Department of Endocrinology and Metabolic Diseases at the LUMC, Thomas ('Ken jij nog een aardige reviewer?'), Eric, Ivo ('Ben je alweer met vakantie geweest?') and C., with which we had a pleasant collaboration during the entire period of my PhD and that provided us with most of the data presented in this thesis.

Besides work-related topics, the daily interactions and conversations with my colleagues at work and during the lunch break meant a lot to me and were an important part of what made my time at the LKEB so enjoyable. In my office and in the room next door, first Avan, Elco (the day will come when I win a squash match against you), Julien ('Please don't hit me with your squash racket, I didn't mean to play that mean!', actually I did), Maribel, Meng and Peter ('Morrrrfius') and later Ahmed ('This is a horrible movie!'), Artem ('Lekkerlicious! You can use the expression if you want.'), Jorik, Martijn ('Bird is the word'), Nora ('I brought fruit. I just didn't eat it yet.'), Oleh, Ece and Vikas ('Guten Tag!') were providing a good atmosphere

Acknowledgements

and we had a lot of fun together at work and also during several evening activities like bowling, pancakes at Peter's or drinks after work. Hopefully there will be more activities in the future and I am already looking forward to join. Furthermore there are the guys from the CTA and MRI group, with whom I had lunch together almost every day. I really enjoyed this daily ritual with conversation topics ranging from politics, best practice for gardening, Kindergarten experiences with Assembler and Basic to discussions about the probability of god's existence.

I also want to express my gratitude to two colleagues, B. and H., that provided a listening ear and a lot of support and understanding during not so pleasant times, when things didn't go too well. They contributed an important part to getting me back on track and to finally be able to finish this thesis.

Although I spend most of my hours every day with my colleagues, my family and my friends play the most important role in my life. They fulfil my basic needs that are necessary to be able to work successfully.

Ten eerste wil ik graag Marlies en Bert, Carolien, Ferry en Feliz van harte bedanken, dat ik in Nederland met open armen werd ontvangen en dat ik me meteen thuis kon voelen. In Delft heb ik een studentenkamer gevonden en de 'DGW group' (Bart, Bianca, Chris, Christian, Dhiradj, Freek, Jantine, Mark, Marnix, Mathijs, Michiel, Monica, Pepijn, Sandra en Simone) is een belangrijk onderdeel van mijn leven in Nederland geworden. Bedankt voor het in stand houden van het contact, ook al ben ik normaliter niet de snelste in het beantwoorden van emails. Dank ook aan Carel, Frits, Leidie en Ruth, die een belangrijke rol hebben gespeeld gedurende de laatste twee jaar. Uiteraard wil ik ook de vroegere (Monito) en de huidige (Mixta en Mucho) leden van onze levende knuffelbeesten dierentuin bedanken voor hun onvoorwaardelijke steun (mits er voldoende voedsel klaar staat en een slaapgelegenheid op het bed beschikbaar is).

Außerdem möchte mich bei meinen Freunden Axel, Harry, Jochen, Marcus, Markus, Otze, Tobi und Wolf bedanken. Leider sehen wir uns nicht mehr oft, aber wenn wir uns treffen kommt es mir so vor, als wäre ich nie weg gewesen und ich schätze das sehr.

Ich möchte mich auch bei meiner Mutti Christa, Gebhard, meiner Schwester und Paranimf Maria, meinem Schwager Thomas, meiner heißgeliebten Nichte Laura, meinen heißgeliebten Neffen Aaron, Marco und Sandro sowie bei meinem Omalein Emilie (Danke für die Socken!) recht herzlich bedanken. Ihr alle seid jederzeit bei mir in meinem Herzen.

Ten slotte wil ik Marieke bedanken, de reden waarom ik naar Nederland ben gekomen. Tijdens de jaren die we nu samen zijn, was je niet alleen mijn partner maar ook mijn beste vriend. Je doet altijd je best om naar me te luisteren en me te begrijpen en ik ben je dankbaar voor je eindeloze steun en je liefde.

Acknowledgements

Curriculum Vitae

Martin Baiker was born in Stuttgart, Germany, in 1978. He graduated *with distinction* from secondary school at the Gymnasium Albstadt-Ebingen (Germany) in 1998 and subsequently fulfilled ten months of social service at a home for seriously handicapped adults. In 1999 he started his studies at the University of Cooperative Education (Telecommunications) in Stuttgart, Germany, received a Bachelor of Science in 2002 and continued his studies in Medical Engineering at the University of Applied Sciences in Ulm, where he received his Dipl.-Ing.(FH) *with distinction* in 2005. His final thesis was conducted at the Department of Anatomy and Embryology at the Leiden University Medical Center (LUMC), Leiden, The Netherlands, on staining methods for chicken embryo vasculature. For this project, he received a scholarship from the German Academic Exchange Service (DAAD). In the same year he enrolled in Biomedical Engineering (Medical Imaging) at the Technical University Delft, The Netherlands, where he finished his studies by receiving a Master of Science degree *cum laude* in 2007. His final project was conducted at the Laboratory for Clinical and Experimental Image Processing (LKEB) at the Leiden University Medical Center, Leiden, The Netherlands, on atlas-based registration of mouse skeletons. Also for this project, he received a scholarship from the German Academic Exchange Service. From 2007 until 2011, he worked towards his PhD at the same department. The results of his research are presented in this thesis.

During his studies, he conducted several internships, including a two month stay at a research lab of the Robert Bosch Corp. in Palo Alto, USA, and a six months stay at the Escola Politècnica Superior de Gandía, Gandía, Spain. Furthermore he worked as a teacher for secondary school (math and physics), in a project involved in the construction of sewer systems and as a student assistant at the Department of Anatomy and Embryology at the LUMC.

His current research interests include preclinical image analysis and visualization, knowledge-guided image registration and segmentation, multimodality image fusion and bioluminescence tomography.